AGEING OF ZIRCONIA CERAMICS FOR DENTAL APPLICATIONS

Anastasia Samodurova

Doctoral Dissertation
Jožef Stefan International Postgraduate School
Ljubljana, Slovenia, October 2015

Evaluation Board:

Asst. Prof. Dr. Goran Dražić, Jožef Stefan Institute, Jamova cesta 39, 1000 Ljubljana, Slovenia

Prof. Dr. Anton Meden, Faculty of Chemistry and Chemical Technology, University of Ljubljana, Večna pot 113, 1000 Ljubljana, Slovenia

Prof. Dr. Marc Anglada, Universitat Politecnica de Catalunya, Calle Jordi Girona, 31 08034 Barcelona, Spain

MEDNARODNA PODIPLOMSKA ŠOLA JOŽEFA STEFANA
JOŽEF STEFAN INTERNATIONAL POSTGRADUATE SCHOOL



Anastasia Samodurova

AGEING OF ZIRCONIA CERAMICS FOR DENTAL APPLICATIONS

Doctoral Dissertation

STARANJE CIRKONIJEVE OKSIDNE KERAMIKE ZA DENTALNE NAMENE

Doktorska disertacija

Supervisor: Prof. Dr. Tomaž Kosmač

Co-supervisor: Dr. Andraž Kocjan

Ljubljana, Slovenia, October 2015

Index

Abstract ..... **VI**

Povzetek ..... **VIII**

Abbreviations ..... **X**

1 Introduction **1**
1.1 Zirconia 1
1.2 Phase Equilibria in ZrO_2-Y_2O_3 System 3
1.3 3Y-TZP as a Biomaterial in Orthopaedics and Restorative Dentistry 5
1.4 Stabilization of the Tetragonal Phase 7
1.5 Low-Temperature Degradation 9
1.5.1 Kinetics of LTD 9
1.5.2 Nucleation of LTD 11
1.5.3 Propagation of LTD 13
1.5.4 Role of water 14
1.5.5 Ways to improve the LTD stability 16

2 Aims and Hypothesis **20**

3 Materials and Methods **22**
3.1 Materials 22
3.2 Preparation of Specimens 22
3.2.1 Preparation of biscuit-sintered ceramics 22
3.2.2 Characterization of biscuit-sintered materials 23
3.2.3 Infiltration and sintering 23
3.3 Characterization of Sintered Materials 24
3.3.1 Density and microstructure 24
3.3.2 Phase composition 24
3.3.3 Mechanical properties 25
3.3.4 Impedance measurements 26
3.3.5 Optical properties 26
3.3.6 In-vitro ageing 27

4 Results **29**
4.1 Preparation of Specimens 29
4.1.1 Characterization of pre-sintered 3Y-TZP 29
4.1.2 Elaboration of infiltration technique 29
4.2 Characterisation of Sintered Alumina or/and Silica-Doped 3Y-TZP 32

4.2.1 Microstructural analysis 33
4.2.2 Phase composition 37
4.2.3 Mechanical properties 39
4.2.4 Fracture mode 40
4.2.5 Investigating grain boundaries in 0.25A-TZ and 0.25A-TZ/SiO_2 using impedance spectroscopy 42
4.2.6 Optical properties 45
4.3 *In vitro* Ageing Behaviour 46
4.3.1 XRD of aged 3Y-TZP 46
4.3.2 The effect of alumina or/and silica co-doping on the LTD of tetragonal zirconia 47
4.3.3 FIB-SEM analysis of transformed zone 51
4.3.4 Sintering temperature-related ageing properties 53
4.3.5 Mechanical properties of the aged materials 55

5 Discussion 57
5.1 The Infiltration Technique 57
5.2 Characterization of Sintered Ceramics 57
5.2.1 Microstructure and phase composition 57
5.2.2 Mechanical properties 61
5.3 LTD 61
5.3.1 Effect of alumina 61
5.3.2 Effect of silica 64
5.3.3 Effect of co-doping 65
5.4 Influence of the Yttria Distribution (Heterogeneities/Segregation) in 3Y-TZP Grains on the LTD 67
5.5 Origin of the Low-Theta Broadening of $(1\ 01)_t/(1\ 1\ 1)_c$ Peak on the XRD of Aged 3Y-TZP 71

6 Conclusions 73

7 Acknowledgements 75

8 References 76

9 Index of Figures 87

10 Index of Tables 92

11 Appendix 93
11.1 Personal Bibliography 93

Abstract

This doctoral thesis deals with the kinetics and mechanisms of hydrothermal ageing of 3 mol % yttria-doped tetragonal zirconia polycrystalline (3Y-TZP) ceramic, which is an attractive material for dental restorations due to its unique combination of excellent mechanical properties, biocompatibility and aesthetic appearance. The tetragonal grains in sintered ceramic are thermodynamically metastable and can be transformed to a monoclinic form by an externally applied stress, thereby developing transformation toughening. On the other hand, the metastability of the tetragonal phase makes 3Y-TZP ceramics susceptible to spontaneous tetragonal-to-monoclinic (*t–m*) transformation in humid environments at slightly elevated temperatures (~ 30-300 °C), i.e. to the so-called low-temperature degradation (LTD) or ageing. This process is accompanied by intensive microcracking in the transformed zone that may ultimately lead to the degradation of mechanical properties and thereby preventing a use of 3Y-TZP in dental applications. The LTD in 3Y–TZP is mainly affected by the grain size and can be further influenced by doping with alumina or some other oxides, such as ceria, silica, etc.

In my work I focussed on the role of silica or/and alumina-(co)-doping in the nucleation and propagation of the hydrothermally induced *t-m* transformation. In order to differentiate between the distinct contributions of the two dopants to the overall resistance to ageing, the specimens were prepared by infiltration of silica sol into pre-sintered, porous 3Y-TZP discs, which where alumina-free or contained 0.05 and 0.25 wt. % of alumina. The infiltration technique was chosen for co-doping, since it could be easily included in the already established computer-aided design and computer-aided manufacturing machining (CAD/CAM) procedure commonly used in the production of 3Y-TZP dental restorations. After the final sintering, the specimens were characterized in terms of their microstructure, phase composition, mechanical properties and accelerated ageing behaviour. Kinetics of the LTD was studied by quantifying the transformed monoclinic fraction from X-ray diffraction analysis as well as by analysing cross sections of the aged samples by optical microscopy. The sub-surfaces of the aged samples were studied using focused ion beam–scanning electron microscopy analysis. In order to gain a better inside into the possible mechanism associated with the deceleration of LTD by co-doping, selected as-sintered samples were additionally examined by Raman and impedance spectroscopy. Coupled-diffusion experiments were carried out in order to assess the reactivity in in the 3Y-TZP-SiO_2 and 3Y-TZP-SiO_2-Al_2O_3 systems.

The results showed that the grain size was not a prevailing factor influencing the ageing resistance of 3Y-TZP ceramics that were sintered in the temperature range of 1400-1500 °C. The microstructures of all these materials were practically identical, being unimodal and exhibiting similar grain size and size distribution. However, the LTD stability was substantially improved by single-doping and even more by co-doping. The presence of alumina increases the grain boundary cohesion, which was reflected in an increased fraction of transgranular fracture and reduced microcracking upon the moisture-induced *t–m* transformation. The presence of individual alumina grains commonly observed in SEM micrographs of sintered silica-free 3Y-TZP, containing 0.25 wt. % of alumina, indicates a very low solubility of the dopant being restricted to the grain

boundary area reflecting in ~100-400 orders of magnitude higher grain boundary resistivity, compared to the bulk resistivity. In silica-doped and alumina/silica co-doped ceramics sintered at temperatures ≤ 1500 °C an amorphous silica-rich phase was preferentially located at the multiple grain junctions, causing the rounding of zirconia grains and reducing the internal stresses. Silica does not affect the fracture mode, but it substantially reduces the microcracking upon ageing.

The increase of sintering temperatures to 1550-1600 °C resulted in substantial differences in the microstructure, phase partitioning and LTD behaviour of undoped, single-doped and co-doped materials. The addition of alumina enhances the grain growth, but still decelerates the hydrothermal ageing of 3Y-TZP. In contrast, silica-doped 3Y-TZP sintered at higher temperatures (≥ 1500 °C) aged much faster compared to alumina-doped materials. This temperature-related change in the ageing behaviour coincides with the formation of yttria-rich silicate phase in Y_2O_3-SiO_2 system at temperatures ≥1500 °C, leading to the depletion of yttria from the tetragonal grains. In the presence of alumina the diffusion of yttria into the silica phase was prevented, implying that alumina has an impact on the composition and properties of the glassy phase in silica-doped 3Y-TZP.

In high-temperature (≥ 1550 °C) sintered alumina/silica co-doped 3Y-TZP the penetration of silica phase from triple grain junctions along the grain boundaries was observed accompanied by sudden emergence of larger yttria-rich, untransformable, *t`*-ZrO_2 grains within the matrix of small *t* grains with a lower yttria concentration. The overall partitioning process was the slowest in co-doped material, leaving the higher amount of yttria in tetragonal grains, making them more resistant towards transformation and thereby decelerating the LTD. No alumina grains could be found in co-doped material, even when it was sintered at higher temperatures, indicating that a larger amount of alumina can be dissolved in co-doped 3Y-TZP. This will additionally stabilize the *t*-grains.

The alumina/silica co-doping of 3Y-TZP ceramic thus resulted in higher amount of yttria and alumina in tetragonal grains. Higher thermodynamic stability of these grains together with the presence of silica phase at triple grain junctions or/and grain boundaries, led to exceptionally improved LTD resistance of 3Y-TZP, without compromising its strength and fracture toughness.

Povzetek

Doktorsko delo obravnava kinetiko in mehanizme staranja tetragonalne, s 3 mol % itrijevega oksida delno stabilizirane cirkonijeve oksidne keramike (3Y-TZP), ki se zaradi izjemne kombinacije mehanskih lastnosti, biokompatibilnosti in estetskega videza vedno bolj uveljavlja kot alternativen ogrodni material v zobni protetiki. Po sintranju je tetragonalna modifikacija cirkonijevega oksida termodinamsko nestabilna, zaradi česar ima 3Y-TZP keramika sposobnost transformacijskega utrjevanja, je pa istočasno občutljiva na staranje, to je na spontano transformacijo tetragonalne v monoklinsko fazo v vlažnem okolju pri nekoliko povišani temperaturi. Pri tem procesu pride do nastanka mikrorazpok, ki olajšajo prodiranje vode s površine in s tem napredovanje transformacije v notranjost. Intenzivna tvorba mikrorazpok v transformirani površinski plasti povzroči poslabšanje mehanskih lastnosti in zmanjšuje uporabnost materiala v praksi.

V svojem delu sem preučevala vlogo in vpliv malih dodatkov aluminijevega ali/in silcijevega oksida na hidrotermalno inducirano transformacijo 3Y-TZP keramike sinterane pri temperatuturah med 1400 °C in 1600 °C. Da bi lahko določila prispevka obeh dodatkov k celokupni odpornosti proti staranju, sem predsintrane tablete iz komercialnih granulatov 3Y-TZP, ki vsebujejo 0,00, 0,05 and 0,25 mas. % aluminijevega oksida, infiltrirala s solom SiO_2 . Ta način dodajanja SiO_2 sem izbrala, ker bi ga bilo v praksi zlahka možno uporabiti kot dodatno operacijo običajnega CAD/CAM postopka izdelave zobne protetike z rezkanjem predsintarnih blokov in naknadnim zgoščevanjem pri višjih temperaturah. Karakterizacija sintranih vzorcev je obsegala mikrostrukturno in fazno analizo, merjenje mehanskih lastnosti in ugotavljanje odpornosti proti hidrotermalnemu staranju z *in vitro* testiranjem v avtoklavu. Kinetiko staranja sem zasledovala z ugotavljanjem relativnega deleža transformirane monoklinske faze s pomočjo rentgenske praškovne analize in z določanjem globine transformirane cone z optično mikroskopsko analizo poliranih prečnih površin vzorcev po staranju. Dogajanje v tanki plasti neposredno pod površino sem študirala s pomočjo vrstičnega elektronskega mikroskopa, opremljenega z usmerjenim ionskim sklopom (FIB-SEM). Da bi prišla do dodatnih informacij o istočasnem vplivu obeh dopantov na fazno sestavo in porazdelitev faz, sem izbrane vzorce preiskala še z ramansko in impedančno spektroskopijo, izdelala pa sem tudi nekaj difuzijskih členov, s pomočjo katerih sem ugotavljala reaktivnost v sistemih 3Y-TZP-SiO_2 in 3Y-TZP-SiO_2-Al_2O_3.

Rezultati omenjenih analiz so pokazali, da v preiskovanih materialih, sintranih pri temperaturah med 1400-1500 °C, velikost zrn ni imela prevladujočega vpliva na odpornost tetragonalne 3Y-TZP keramike proti staranju v hidrotermalnih pogojih. Ne glede na vrsto in vsebnost dopantov je bila velikost in porazdelitev velikosti zrn v vseh vzorcah praktično identična. Kljub podobni velikosti zrn pa se je z dodatkom enega ali drugega dopanta odpornost materiala proti staranju izrazito izboljšala, še bolj pa ob istočasnem dodatku obeh dopantov. Prisotnost aluminijevega oksida izboljša trdnost mej med zrni, kar se kaže v povečanem deležu transgranularnega loma in občutno manjši gostoti mikrorazpok po hidrotermalno inducirani *t–m* transformaciji. Topnost aluminijevega oksida je majhna, saj so v mikrostrukturi vzorcev z 0,25 mas. % Al_2O_3 prisotna diskretna korundna zrnca. Dopant je pretežno raztopljen v bližini mej med zrni,

kar se odraža v ~100-400 velikostnih redov večji impedance mej primerjavi z volumsko keramiko. SiO_2 je bil v vzorcih, sintranih pri temperaturah ≤ 1500 °C pretežno prisoten kot amorfana faza na stičiščih med zaobljenimi zrni. Prisotnost SiO_2 ne vpliva na vrsto preloma, zmanjšuje pa intenzivnost tvorbe mikrorazpok med staranjem.

Po sintranju pri višjih temperaturah (≥ 1500 °C) postanejo razlike v mikrostrukturi, razmerju ravnotežnih faz (ločevanje faz) in staranju nedopiranih z enim ali drugim dodatkom dopiranih vzorcev večje. Keramika z 0,25 wt% Al_2O_3 se kljub pospešeni rasti zrn stara najpočasneje; keramika z 0,05 mas. % se še vedno stara počasneje, kot nedopiran 3Y-TZP. Dodatek SiO_2 pa kot zaviralec staranja postane neučinkovit, saj se s SiO_2 dopirana keramika stara z enako hitrostjo, kot nedopirana. To temperaturno odvisno spremembo v kinetiki staranja pripisujem začetku tvorbe itrijevega silikata in posledično, zmanjšani koncentraciji itrijevega oksida v tetragonalnih zrnih. V prisotnosti aluminijevega oksida do difuzije itrijevega oksida v silikatno fazo ne pride, na osnovi česar sklepam, da aluminijev oksid pomembno vpliva na sestavo in lastnosti steklaste faze v s SiO_2 dopirani 3Y-TZP keramiki. Pri višjih temperaturah (≥ 1550 °C) opažamo v materialih, (so)dopiranih s SiO_2, prodiranje silikatne faze po mejah med zrni, ki sovpada s pojavom velikih, na Y_2O_3 bogatih *t'*-ZrO_2 zrn v matici manjših *t* zrn z manjšo koncentracijo Y_2O_3. Ravnotežno razslojevanje faz je najpočasnejše v so-dopirani keramiki, zaradi česar ostaja v tetragonalnih zrnih največ Y_2O_3, kar upočasni process staranja. V prisotnosti SiO_2 se topnost Al_2O_3 v 3Y-TZP znatno poveča, saj v so-dopirani keramiki niti s SEMom, niti z ramansko spektroskopijo nisem potrdila prisotnosti korunda.

Istočasen dodatek aluminijevega in silicijevega oksida povzroča večjo koncentracijo itrijevega oksida in večjo topnost aluminijevega oksida v tetragonalnih zrnih. Večja termodinamska stabilnost teh zrn ter manjše lokalne napetosti zaradi zaobljenih zrn vodijo k izjemno povečani odpornosti 3Y-TZP keramike proti staranju, ne da bi se pri tem poslabšala trdnost in lomna žilavost.

Abbreviations

3Y-TZP	=	3-mol%-yttria-doped tetragonal zirconia polycrystalline
FSC	=	fully stabilized zirconia
PSZ	=	partially stabilized zirconia
Mg-PSZ	=	magnesia partially stabilized zirconia
Y-TZP	=	yttria-doped tetragonal zirconia polycrystalline
LTD	=	low-temperature degradation
XRD	=	X-ray diffraction
APB	=	anti-phase domain boundary
TEM	=	transmission electron microscopy
CAD/CAM	=	computer-aided design and computer-aided manufacturing
FPD	=	fixed partial dentures
SEM	=	scanning electron microscopy
MAJ	=	Mehl-Avrami-Johnson
CTE	=	coefficient of thermal expansion
FIB	=	focused ion beam
EBSD	=	electron backscatter diffraction
AFM	=	atomic-force microscopy
EDS	=	energy-dispersive X-ray spectroscopy
EELS	=	electron energy loss spectroscopy
SIMS	=	secondary ion mass spectrometry
TZ-3YB	=	yttria-stabilised tetragonal zirconia powder
TZ-3YSB-E	=	yttria stabilized tetragonal zirconia powder doped with 0.25 wt% of alumina
TZ-PX-242A	=	yttria stabilized tetragonal zirconia powder doped with 0.05 wt% of alumina
TZ	=	ceramic produced from TZ-3YB powder
0.05A-TZ	=	ceramic produced from TZ-PX-242A powder
0.25A-TZ	=	ceramic produced from TZ-3YSB-E powder
TGA/DTA	=	thermogravimetric and differential thermal analysis

1 Introduction

With the aim of replacing the infrastructure of metallic dental prostheses, structural ceramics have been significantly improved and they become increasingly popular in dentistry. Except the stability against the stresses generated by masticatory loads, they must also be aesthetic and biocompatible.

There are only a few ceramics, which are suitable for biomedical applications, namely, alumina (Al_2O_3), zirconia (ZrO_2) and their composites. Both materials combine excellent chemical stability and tissue compatability, but they have specific properties, which should be taken into account when looking for the most suitable material for an engineering application. The engineering grades of alumina are typically harder than zirconia, while zirconia possesses higher fracture toughness and flexural strength. Nowadays, alumina and alimina-zirconia composites are mainly used as load-bearing biomaterials in orthopedics for the production of hip, shoulder and knee replacements, while zirconia is widly used in dentistry for fabrication of crowns, bridges, abutments, root posts and orthodontic brackets.

The present work is devoted to the dental 3 mol % yttria-doped tetragonal zirconia polycrystalline (3Y-TZP) ceramics. The following chapters cover basic information about the material, its properties, advantages and disadvantages.

1.1 Zirconia

At ambient pressure, pure ZrO_2 exhibits three polymorphic structures depending on the temperature [1]: monoclinic symmetry ($P2_1/c$) at room temperature, tetragonal structure ($P4_2/nmc$) above 1170°C and cubic (fluorite) structure ($Fm\bar{3}m$) beyond 2370 °C (Figure 1). The tetragonal to monoclinic (*t-m*) phase transformation in zirconia is martensitic in nature. This transformation is reversible and on cooling it is accompanied by shear strain of ~0.16 % and substantial increase of volume (3-5%) [1]–[3]. This causes high internal stresses and catastrophic failure of fabricated components upon cooling from the sintering temperature. As a result, over decades the interest to pure zirconia as an engineering ceramic material was very limited.

In 1929 Ruff et al. [4] discovered that alloying with calcium oxide (CaO) can keep zirconia in the cubic phase at room temperature. Later it was found, that other oxides of di-, tri- and tetravalent metals such as magnesium, yttrium, lanthanum, ytterbium and cerium can stabilize zirconia in its cubic form as well [5]. These fully stabilized zirconias (FSZ) are of interest for heating elements, oxygen sensors and fuel cell applications. Single crystals of the cubic zirconia are commonly used as diamond simulants in jewellery. FSZ is generally obtained with large concentrations of stabilizers, for example, more than 12 mol% of CaO or more than 8 mol% of Y_2O_3.

In 1972, Garvie and Nicholson [6] introduced the family of partially stabilized zirconias (PSZ) exemplified by CaO-ZrO_2 system. PSZ consists of large cubic zirconia grains as the major phase and tetragonal zirconia precipitates as the minor phase. Besides calcium oxide, there are some other oxides, such as magnesium oxide and yttrium oxide, which are capable to partially stabilize zirconia. PSZ obtained by sintering of powder compacts in the single-phase cubic region of phase diagram (Figure 2) followed by fast

cooling to the cubic/tetragonal (*c*+*t*) two-phase region and annealing at this region to allow nucleation and growth of the tetragonal precipitates within the cubic grains.

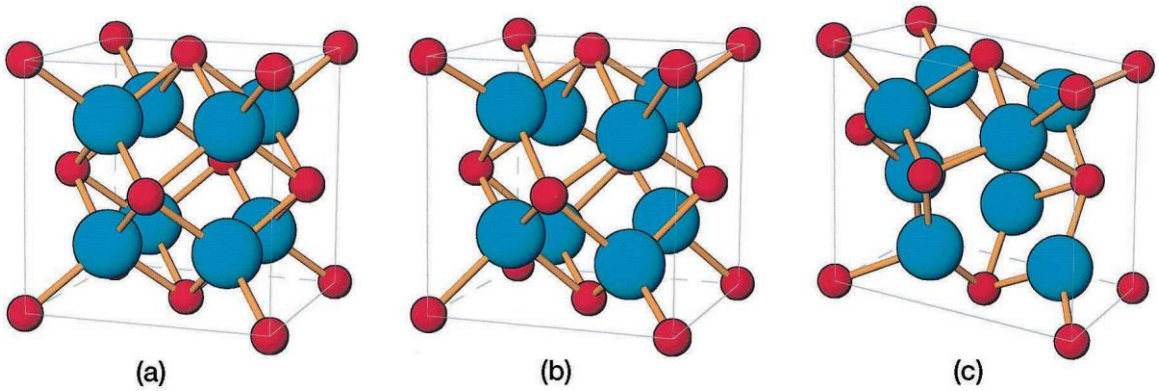


Figure 1: Schematic representation of the three polymorphs of ZrO_2 and the corresponding space groups: (a) cubic ($Fm\bar{3}m$), (b) tetragonal ($P4_2/nmc$), and (c) monoclinic ($P2_1/c$). (Source: H. J. Hannink et al. [7]).

In 1975 Garvie, Hannink and Pascoe [8] reported that magnesia partially stabilized zirconia (Mg-PSZ) exhibits the stress-induced *t-m* transformation, which enhances the strength and fracture toughness of the material. Authors purposely entitled their paper «Ceramic Steel?» to emphasize the fascinating simmilarity of zirconia-based alloys to martensitic steels. Namely, the thermal expansion coefficient and elastic modulus of zirconia are similar to those of steel. As the formation of martensite in steels, the *t-m* phase transformation in zirconia occurs without diffusion of matter (it is diffusion-less) and it has athermal kinetics. This means that the transformation takes place with the speed of sound as soon as the nucleus of the new phase appears. The discovery of the stress-induced transformation toughening of zirconia not only increased the industrial applicability of the material, but it also stimulated an intense effort to understand the relation between transformation and enhancement of mechanical properties. It was a critical point in the development of improved engineering ceramics in general and in the study of toughening of ceramic systems in particular.

The further breakthrough in the development of zirconia ceramics as an engineering material was made by Rieth et al. [9] and Gupta et al. [10], who discovered the so-called yttria-stabilised tetragonal zirconia polycrystalline (Y-TZP) – a fine-grained (0.3 to 0.5 μm in diameter) monophase material, which nominally contains 2-3 mol.% of Y_2O_3. These metastable tetragonal ceramics exhibited exceptional fracture toughness (5-10 $MPa \cdot m^{1/2}$) and the highest strength (>1000 MPa) among all monolithic ceramics. These outstanding mechanical properties of zirconia-based ceramics opened a way for new structural devices.

The excitement created by the development of Y-TZP, however, was dampened in 1981 by Kobayashi et al. [11], who discovered a negative side of metastability of tetragonal zirconia. Authors showed that after prolonged exposure to water vapor in the temperature range 150-450 °C the material suffers from a slow *t-m* transformation, which occurs at the sample surface and is followed by microcracking and loss in strength. Nowadays, this phenomenon, which is known as low-temperature degradation (LTD), or ageing represents the major drawback of tetragonal zirconia ceramics. However, in the mid 1980th the thread of the LTD to occur at ambient or/and body temperatures was underestimated and thanks to work by Christel et al. [12] Y-TZP was added to the list of high-performance bioceramic materials.

1.2 Phase Equilibria in ZrO_2-Y_2O_3 System

The first detailed study of the zirconia-yttria system was done in 1951 by Duwez et al. [13]. Since that time the binary diagram has been significantly refined many times. The evolution of the phase diagram is illustrated in Figure 2, which shows the original diagram introduced by Duwez [13], the diagram proposed by Scott in 1975 [14] and some more recent diagrams [15], [16].

The discrepancies between the different studies appeared due to the difficulties associated with determination of the true equilibrium in zirconia-yttria system. Since at temperatures above 2000 °C it is difficult to carry out direct studies of crystal structure, the XRD measurements were done at room temperature on the rapidly cooled samples. Even if cooling is sufficiently fast to prevent the compositional changes, the structural changes may still occur, which would complicate the interpretation of the results. Another problem is slow cation diffusion [17], therefore it is particularly difficult to establish the equilibrium, especially at lower temperatures (<1400 °C). Figure 3 shows the estimated time of diffusion, which is necessary to homogenize the Y content in a 0.5- or 3-µm-diameter grain at different temperatures [17]. Even at a temperature 1500 °C estimated time of homogenization is of the order of several weeks for the 3-µm-grain sized material and a few days/hours for the 0.5-µm-grains. The characteristic features of the martensitic transformation, such as the initial and final temperatures, further complicate the interpretation of the diagram and the interpretation of microstructures. This uncertainty is marked in Scott's phase diagram by the hatched region.

Finally, the existence of metastable states complicates things even more. Considerable clarification was obtained from computer modeling of the phase diagram, particularly it gave the position of the metastable T_0 lines. The T_0-line corresponds to the situation when the Gibbs energy of one phase is equal to the other one. Figure 2d shows the equilibrium phase diagram along with T_0-lines for diffusionless *c–t'* and *t–m* transformations. Scott [14] was the first who suggested that the diffusionless cubic to tetragonal phase transformation could occur in ZrO_2-Y_2O_3 alloys on quenching from high temperatures with 5 to 12 wt% of Y_2O_3. After this observation the transformation was extensively studied [18]–[24]. Miller et al. [18] found a tetragonal phase with high concentration of Y_2O_3 in plasma-sprayed 4.5 mol% Y_2O_3-ZrO_2. They called it *t'*-form to distinguish it from conventional *t*-ZrO_2 with lower content of Y_2O_3. Since this phase was resistant to martensitic *t-m* transformation, authors described it as nontransformable tetragonal phase. During the *c-t'* transformation the anti-phase domain boundaries (APB's), which can be observed by transmission electron microscopy (TEM) analysis, are forming [19]–[22], [25]. Such APB's have never been observed in *t*-ZrO_2, which was formed by a diffusional reaction. Scott suggested that upon annealing for a long time in the two-phase *t+c* part of the phase diagram, the *t'*-phase would decompose diffusionally to cubic and tetragonal phases. In agreement with Scott's predictions after annealing at 1200-1600 °C for 100 h the *t'* phase was decomposed to high-yttria *c*-ZrO_2 and low-yttria *t*-ZrO_2 [18]. Lanteri et al. [26] showed that the *c-t'* phase transformation is ubiquitous in certain Y_2O_3-containing alloys of ZrO_2 ceramics and can occur even upon slow cooling. The slowly cooled single-crystal two phase alloy 8Y-TZP annealed at 1600 °C for 50 h also showed the APB-like features in the matrix which are similar to those of *t'* phase.

Both, *t* and *t'* forms, belong to the same space group $P4_2/nmc$ [27]. In the *t*- and *t'*-forms, the *c*-axis is larger than the *a*-axis (axial ratio c/a > 1) and the oxygen is displaced alternatively along the *c*-axis.

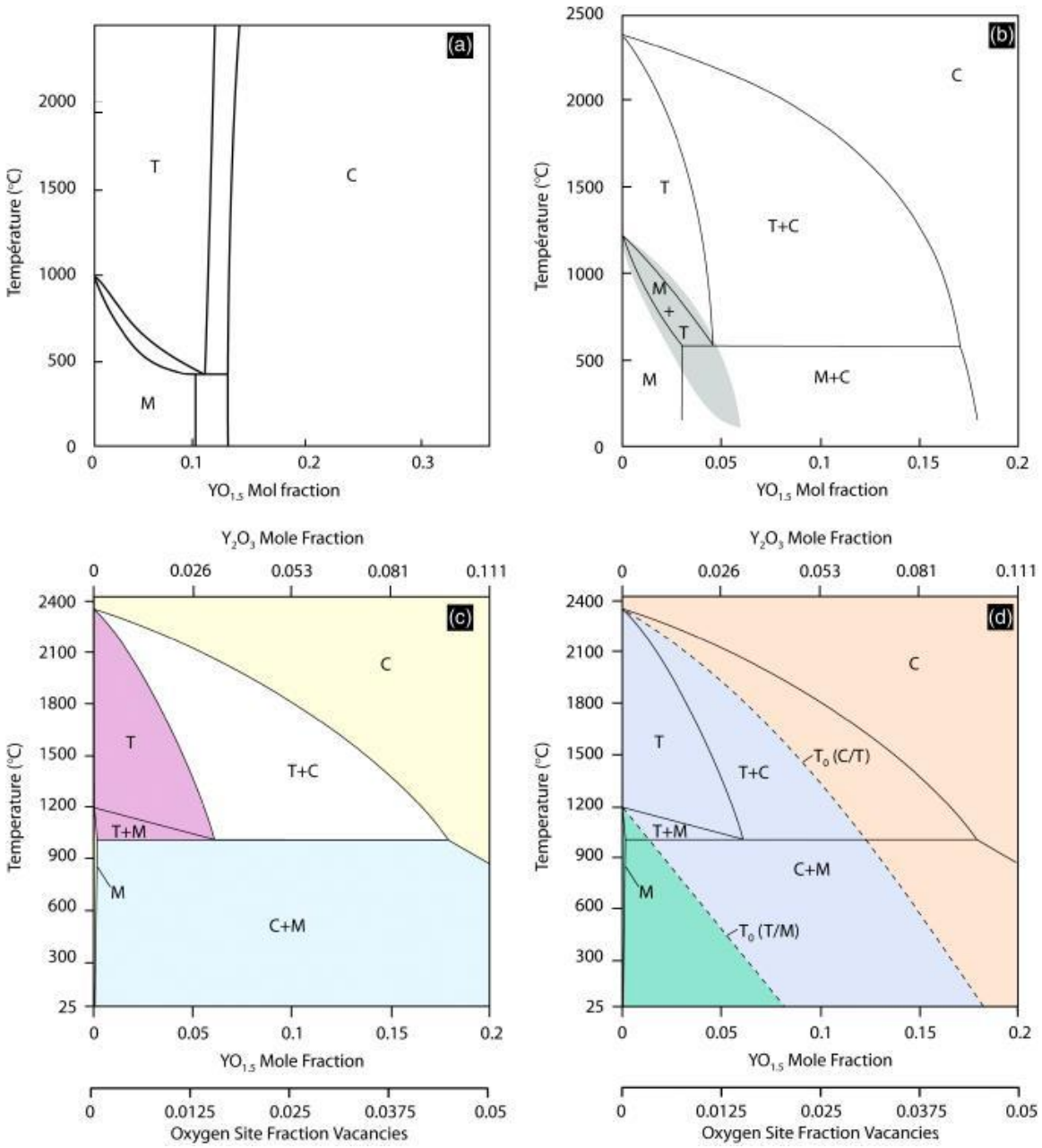


Figure 2: Evolution of the zirconia–yttria phase diagram: (a) original diagram by Duwez [13] in 1951; (b) diagram presented by Scott in 1975 [14]; (c) and (d) the most recent diagrams [15]; (d) is the metastable phase diagram (Source: Chevalier et al. [28]). Unsigned regions in Duwez's phase diagram were assumed to be two-phase without actual experimental proof. The hatched region in Scott's phase diagram shows the uncertainty of characteristic features of the martensitic transformation, such as the initial and final temperatures.

Using the high-temperature XRD, Yashima et al. [29] showed that the *t'* phase prepared by rapid quenching of melts with 12 mol.% of $YO_{1.5}$ can change not only into the *c*, but also into the *t''* phase at 1400 °C. Similarly to the *c* phase the axial ratio of the *t''*-form is unity but the oxygen is displaced along the *c*-axis making the symmetry tetragonal [27], [30], [31]. The space group of *t''* phase was assigned to be $P4_2/nmc$ after the examination of various space groups which are subgroups of $Fm\bar{3}m$ and supergroups of $P4_2/nmc$ [27].

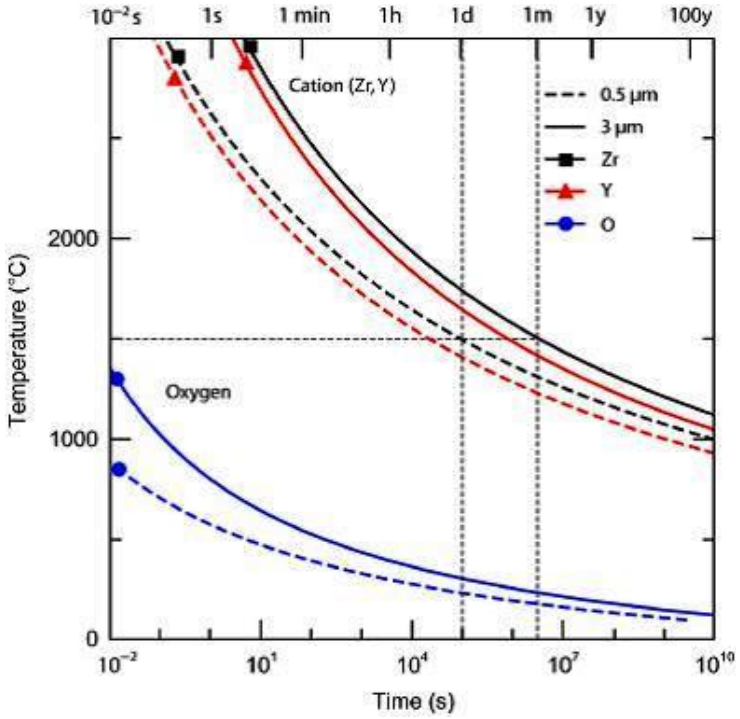


Figure 3: Estimated time of diffusion needed to homogenize the Y content of 0.5- and 3-µm-diameter grains at different temperatures in 3Y-TZP. TZP – tetragonal zirconia polycrystals; Y – yttria.

The transformability of the high-temperature equilibrium products of the *t'* phase decomposition leads to a situation, when up to five (*m*, *t*, *t'*, *t''*, *c*) distinct phases can be present at a given point in the phase evolution process at ambient conditions.

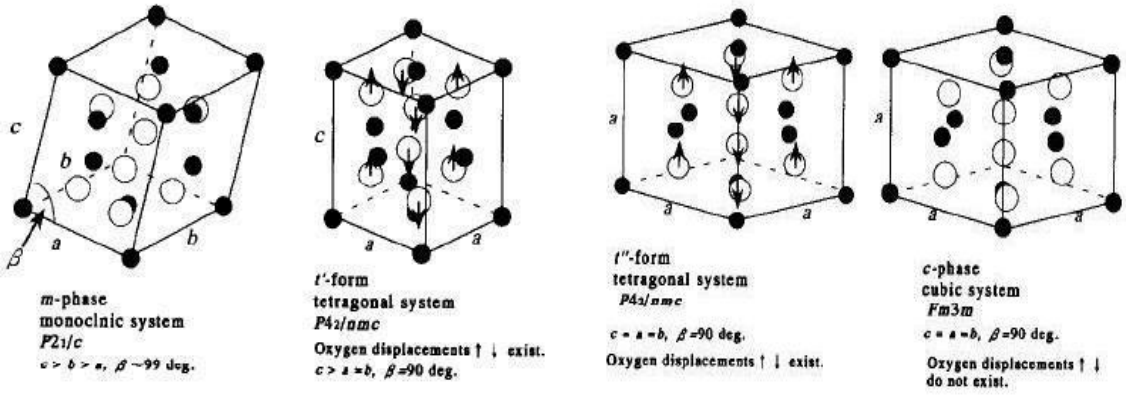


Figure 4: Shemathic representation of the crystal structures of monoclinic, *t'*, *t''* and cubic phases (Source: Yashima et al. [29]).

1.3 3Y-TZP as a Biomaterial in Orthopaedics and Restorative Dentistry

The research and development of zirconia as a biomaterial started in late 1960s. The first paper concerning the biomedical application of zirconia was published in 1969 by Helmer and Driskell [32]. Ca-PSZ and Mg-PSZ were proposed for this application, but after discovery of tough and strong Y-TZP [9], [10], it became the main material for the clinical use.

In 1990s, Y-TZP was introduced into clinics as an alternative to alumina because of its

superior mechanical properties, excellent chemical stability and biocompatibility [33]. In the next decade around 600 000 zirconia femoral heads were implanted. Clinical results until 2000th were satisfactory; at that time only a couple of failures were reported for zirconia femoral heads. In 1997 the U.S. Food and Drug Administration reported that the standard steam sterilization procedure (134°C, 2 bars) led to surface roughening of zirconia implants [34]. More importantly, in 2001–2002, several hundreds of Y-TZP femoral heads failed in a short period. The appearance of fractures was associated with the LTD [35]. This episode had a strong negative impact on the use of zirconia in orthopedics. In particular, the main supplier of zirconia implants at that time, French company Ceramiques Techniques Desmarquest (Saint Gobain), stopped manufacturing of biomedical devices. Other companies, such as Ceramtec and Mathys Orthopedie GmbH in Germany, switched to alumina-zirconia composites, which were introduced to the biomaterials market in 2002 as load-bearing components for hip replacements [36].

In the late 1990s, the success of zirconia for orthopedic implants encouraged its use for dental restorations. Initially Y-TZP was used for the fabrication of endodontic brackets, root posts and implant abutments. Later, the development of CAD/CAM technology, which includes the fabrication of pre-sintered Y-TZP restoration, opened the path to the production of highly precise, individually designed fixed partial dentures (FPD), particularly, single crowns and bridges [37]. The replacement of the traditional metal-based FPDs with all-ceramic dentures was driven mainly by improved aesthetics and excellent tissue compatibility. Additionally, the absorbent nature of biscuit-sintered 3Y-TZP compacts provided the opportunity to shade the material prior to sintering by infiltration with colouring liquids.

Dental restorations produced from currently available 3Y-TZP blanks by soft machining are commonly sintered at temperatures between 1350 °C and 1550 °C depending on the manufacturer [38]. The microstructure of 3Y-TZP ceramics for dental applications consists of small grains (0.2–0.5 μm in diameter, depending on the sintering temperature). A representative SEM micrograph is shown in Figure 5. The mechanical properties are significantly better than for any other available dental ceramic. It shows flexural strength in the 800–1000 MPa range and fracture toughness in the 6–8 $MPa \cdot m^{0.5}$ range depending on the processing methods [39].

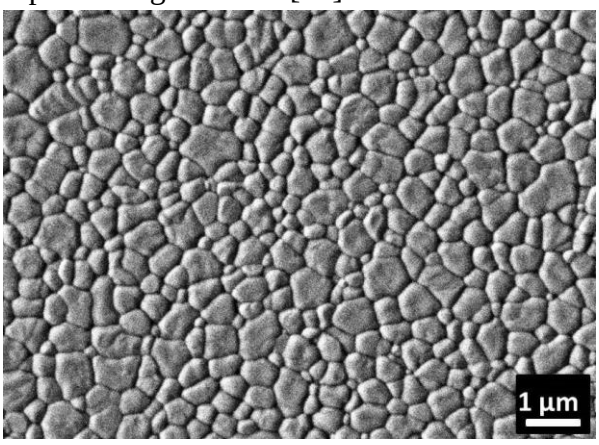


Figure 5: SEM micrograph of 3Y-TZP (TZ-PX-242A, Tosoh, Japan) sintered at 1550 °C for 2 h.

Along with excellent mechanical properties, attractive aesthetics and biocompatibility, Y-TZP ceramics also have some problems, which limit their practical application as dental materials.

The major problem of zirconia-based all-ceramic dental restorations is porcelain chipping [40], [41]. Porcelain veneer is needed because of its aesthetic appearance,

hardness and elastic modulus, which match to hard tissues (dentin and tooth enamel). Unfortunately, its strength and fracture toughness are low, so the veneer is the weakest place of the prosthesis. Chipping of the porcelain veneer on the ceramics occurs much more frequently than chipping of the porcelain on the metal-based FPDs. This occurs due to the higher chemical inertness, worse wetting ability and considerably lower thermal conductivity of ceramics. Due to the porcelain chipping monolithic full-contour 3Y-TZP ceramics are being introduced [42]–[44].

No evidence of LTD was reported for dental 3Y-TZP restorations, as the veneering porcelain protects the material, separating it from the aggressive oral environment. However, some parts of the FPD may not be entirely covered by porcelain, and it has been shown recently that commonly used luting cements absorb water via dentine tubules, thereby exposing the core surface to moisture, which may lead to the nucleation of the LTD. Moreover, since the porcelain-free full-contour 3Y-TZP ceramics are being introduced, the issue of LTD must be kept in mind.

1.4 Stabilization of the Tetragonal Phase

Factors, which influence the stability of tetragonal zirconia either in powders or in densely sintered ceramics, can be described using the thermodynamic approach.

It was shown that after calcination of precipitated zirconium hydroxide the resultant nanocrystalline zirconia powder appears in the high-temperature tetragonal form at room temperature even without using the stabilizers [45].

In 1965 Garvie was the first, who used the thermodynamic approach to explain the unusual appearance of the high-temperature tetragonal phase in wet-chemically synthesized powder at room temperature [45]. The following equation, which takes the surface energy into account was proposed:

$$F_{mon} + \alpha_{mon} A_{mon} = F_{tetr} + \alpha_{tetr} A_{tetr}, \qquad (1)$$

where F_{mon} and F_{tetr} are the molar free energies of the monoclinic and tetragonal zirconia respectively, A_{mon} and A_{tetr} are the corresponding molar surface areas, and α_{mon}, α_{tetr} are the surface energies. Thus, the stability of the tetragonal phase in powder is the result of its lower surface energy (0.77 J/m^2) comparing to the monoclinic phase (1.13 J/m^2). Using the aforementioned equation, Garvie calculated that the critical particle size, above which the metastable tetragonal phase could not exist at room temperature, is 30 nm (from XRD analysis). The role of the surface energy was later confirmed by Suresh et al. [46], who observed slower *t-m* transformation upon cooling for smaller particles.

The situation for sintered zirconia is different in that the tetragonal precipitates (in PSZ), grains in TZP or inclusions in zirconia toughened ceramics, such as zirconia toughened alumina (ZTA) are constrained in the matrix. For these cases a model was derived by Lange [47], who considered the transformation thermodynamics of isolated spherical particles in the elastic matrix. Although this model is rather idealized and does not take into account the irregular shape of grains and free surfaces, it provides good inside into factors, which influence the *t-m* transformation. The change of free energy between the initial untransformed tetragonal state and the final transformed monoclinic state is given by the equation:

$$\Delta G_{t-m} = \Delta G_c + \Delta U_{SE} + \Delta U_c, \qquad (2)$$

where ΔG_C (<0) is the chemical free energy change, which depends on temperature and the stabilizer content. ΔU_{SE} is the differential strain energy, which depends on the elastic modulus of the surrounding matrix, the size and the shape of the particle and the presence

of internal or external stresses. ΔU_C is change of energy associated with the formation of new interfaces when the transformation occurs.

When $\Delta G_{t\text{-}m}$ becomes negative, the tetragonal grain is unstable and may transform into the monoclinic phase. The value of the free energy change can be increased by adding the stabilizing oxide or by dispersion of the second phase in the zirconia matrix. The addition of other particles, such as alumina, into zirconia matrix decreases $\Delta U_{SE,}$ favouring the *t-m* transformation [48]. This is explained by the appearance of residual stresses during cooling of alumina-containing 3Y-TZP as the result of different coefficients of thermal expansion (CTE) and elastic modulus between the alumina and zirconia particles. $\Delta G_{t\text{-}m}$ may also be influenced by externally applied or by existing internal stresses: tensile hydrostatic stress will reduce ΔU_{SE}, destabilizing the tetragonal phase, whereas hydrostatic pressure favours the retention of the tetragonal phase. One of the consequences of these contributions is that the driving force for the *t-m* transformation will not be the same in the bulk and on the surface, because neither ΔU_{SE} nor ΔU_C are the same.

Another possibility for increasing $\Delta G_{t\text{-}m}$ is to reduce the grain size, e.g. by adding sintering additives that reduce the sintering temperature. The critical grain size often reported for bulk *t-m* transformation is on the order of micrometer, whereas it drops to around a few hundreds nanometres at the surface.

Either stabilizing oxides, which increase ΔG_C or additional compressive stresses (stiff particles), which decrease ΔU_{SE} are needed in order to obtain bulk monolithic tetragonal zirconia. Thus, in scope of the thermodynamic approach, one can expect that the incorporation of Y_2O_3 or other oxides into ZrO_2 lattice will stabilize the *t*-zirconia by decreasing $|\Delta G_C|$.

From the crystallographic point of view, the di- or trivalent cations replace a part of the Zr^{4+} ions and create the vacancies in the oxygen sublattice in order to maintain the charge neutrality. For example, in Y-TZP the incorporation of two Y^{3+} will create one oxygen vacancy $V_O^{\bullet\bullet}$ [49] :

$$Y_2O_3 + 2Zr_{Zr}^{x} + O_x^o \xrightarrow{ZrO_2} 2Y'_{Zr} + V_O^{\bullet\bullet} + 2ZrO_2. \qquad (3)$$

Livage et al. [50] and others [51]–[56] believe that the oxygen vacancies play an important role in the stabilization of high-temperature zirconia phases. Koutouros and Petzow [57] claimed that there is a critical minimum and a critical maximum of vacancies for each ZrO_2 phase. Under the critical minimum the *t-m* transformation will occur.

The effect of vacancies on the stability of high-temperature phases at room temperature was explained by the lattice relaxation around oxygen vacancy in doped ZrO_2 [58]. The presence of vacancies reduces the average cation coordination number to the value between 7 and 8 for YSZ, depending on the dopant concentration and makes the local atomic environments rather different from the corresponding stoichiometric high-temperature tetragonal and cubic phases of pure ZrO_2. The host and/or dopant cations as the nearest neighbours to the positive charged vacancy move outwards because of the electrostatic repulsion between the same charged species. This repulsion will cause the *c*-axis of the lattice to increase. Conversely, the vacancy allows the surrounding oxygen ions to draw inward and simultaneously repeal from the next nearest oxygens. The local bonding is disrupted and vicinity of the oxygen vacancy relaxes. The local lattice relaxation around the vacancy perturbs several lattice sites.

Subbarao [51] suggested that the size of the dopant cations may also influence the stabilization. Li et al. [59], while studying the local structures of Zr and dopant cations in zirconia solid solutions with oxides of trivalent (Fe_2O_3, Ga_2O_3,Y_2O_3 and Gd_2O_3), found that the ionic size of dopant determines the preferred locations of oxygen vacancies. Vacancies introduced by the oversized dopants (Y^{3+} and Gd^{3+}) are located as nearest

neighbours to Zr atoms, leaving 8-fold oxygen coordination to dopant cations. The undersized dopants (Fe^{3+} and Ga^{3+}) compete with Zr^{4+} ions for the oxygen vacancies in zirconia, resulting in 6-fold oxygen coordination and a large disturbance of the surrounding next nearest neighbours. Oxygen vacancies are associated with the Zr^{4+} cations for the oversized dopants, and with two dopant cations for the undersized dopants. This different availability of oxygen vacancies to Zr is responsible for the different stabilization effects of oversized and undersized trivalent dopants: the oversized trivalent dopants stabilize the cubic and tetragonal phases more effectively than the undersized trivalent dopants.

The substitution of Zr^{4+} ions by Ce^{4+} does not create oxygen vacancies and yet stabilizes *t*- and *c*-zirconia phases at room temperature [60], implying that in this case the stability is not affected by the presence of oxygen vacancies. Koutouros and Petzow noticed that in CeO_2-stabilized TZP after sintering at 1400 °C in air, the Ce^{4+} can be partially reduced to Ce^{3+}, which would create oxygen vacancies for charge neutrality. Therefore, the reason why *t*-zirconia could not be stabilised at room temperature with less than 9 mol% of CeO_2 is that the total amount of reduced Ce^{3+} is not enough to introduce the minimum number of oxygen vacancies (critical minimum), which is essential for the metastability. However, Li et al. [60] attributed the stabilization of the *t*-phase by tetravalent dopants such as Ce^{4+} to the oversized dimension of this ion. Ce^{+4} forms a random substitutional solution in the Zr tetragonal lattice, but adopts a more symmetric 8-fold coordination due to the bigger size of Ce^{4+} with respect to Zr^{4+}, resulting in decreased tetragonality of the unit cell, and the stabilization of the tetragonal and cubic phases.

Some authors believe that the metastability of *t*-zirconia occurs as a result of simultaneous impact of several effects. For example, Hannink et al. [7] claim that the metastability of *t*-zirconia may be explained in terms of balance between chemical, strain and interfacial energies. The exact mechanism still remains disputable.

1.5 Low-Temperature Degradation

1.5.1 Kinetics of LTD

To quantify the progress of the *t-m* transformation with time the change in the monoclinic content on the surface measured either by XRD [61] or by Raman spectroscopy [62] is commonly used. Studies of hydrothermal degradation of tetragonal zirconia by both methods suggested the nucleation and growth mechanism for the transformation because of the sigmoidal variation of monoclinic phase with time for different temperatures (Figure 6) [61].

The ageing curves obtained using the XRD analysis were fitted by Mehl-Avrami-Johnson (MAJ) equation:

$$\alpha = 1 - \exp(-(b \cdot t)^n), \qquad (4)$$

where α is the monoclinic fraction, *t* is time of ageing, *b* is the factor, describing the temperature dependence of the ageing, and *n* is a constants. The *b* factor is derived from fitting the experimental data according to the following type of Arrhenius equation:

$$b = b_0 \exp(\frac{Q}{RT}) \cdot b, \qquad (5)$$

where b_0 is a material constant, Q is the activation energy of hydrothermal ageing, R is the universal gas constant, and T is the absolute temperature. b can also be calculated for each ageing temperature from a $\ln(\ln(1/(1-\alpha)))$ versus $\ln t$ plot. Chevalier et al. [61] observed the liner relationship with a constant value of *n* equal to 3.6±0.4 for 3Y-TZP material sintered at 1500°C for 2 h and aged at temperature range from 70° to 100°C.

According to MAJ theory the value of *n* between 3 and 4 corresponds to the nucleation and three-dimensional growth process. The plotting of ln *b* versus 1/T gives the activation energy of 106 kJ/mol.

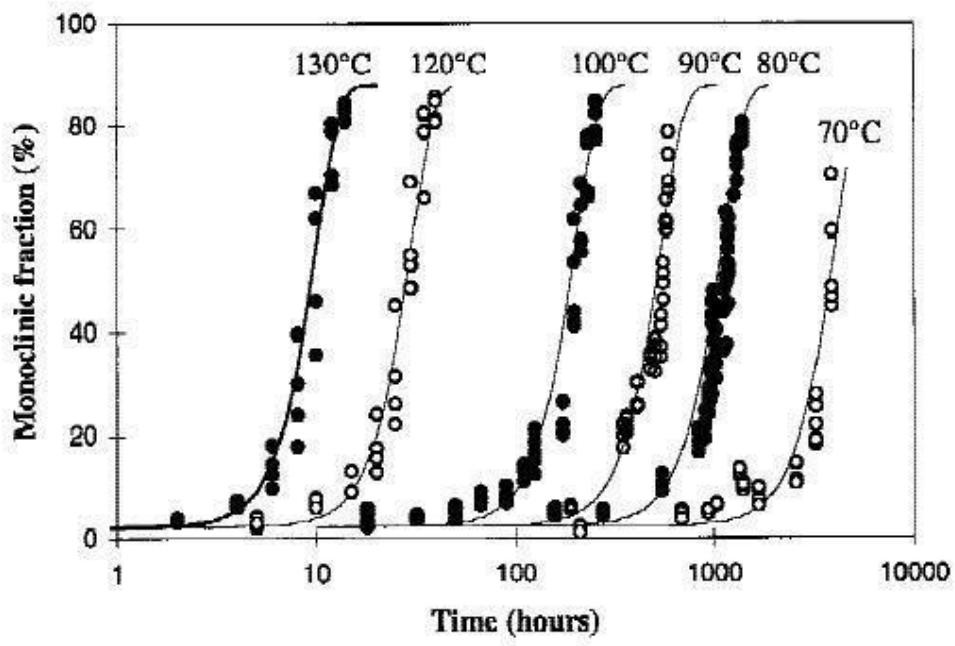


Figure 6: Monoclinic content measured by XRD versus time for 3Y-TZP sintered at 1500 °C for 2 h, polished and aged at temperatures ranging from 70 to 130 °C (Source: Chevalier et al. [61]).

The nucleation and growth mechanism was further confirmed by observations of topological changes upon ageing on the polished surface of tetragonal zirconia using optical interferometry (OI) (Figure 7) [63]. After an incubation period of about 1 h the nucleation of monoclinic sites was clearly visible as small surface upheavals with a diameter close to 1 μm, which correspond to the transformation of one or a few grains. At that time the amount of monoclinic fraction measured by XRD was still close to 0%. After 5 h the monoclinic sites increased in size and in addition to that new monoclinic sites are appeared. The XRD analysis of this surface showed that the amount of monoclinic phase reached ~ 10%.

It should be noticed that the penetration of X-ray in zirconia is low (typically limited to several microns in depth). The hydrothermal *t-m* transformation however proceeds deeper into the bulk. When all the volume accessible by XRD underwent a *t-m* transformation, no further increase in the XRD monoclinic fraction will occur. In other words, the monoclinic fraction as determined by XRD on the surface of the tetragonal zirconia increases with the ageing time and approaches to a saturation plateau. The saturated monoclinic phase content varies, depending on the grade of the material, but never reaches 100% *m*-ZrO_2 even after very long exposure in steam. This is explained by the presence of a fraction of cubic phase in 3Y-TZP ceramics, which is sintered in a bi-phasic (*c*+ *t*) region.

The transformed layer can be observed by SEM analysis of cross section of aged material. Keuper et al. [64] used focused ion beam technique (FIB) to prepare artifact-free cuts of 3Y-TZP sintered at 1530 °C for 2 h and aged at 134 °C for 3-200 h. Samples subsequently were investigated by SEM, electron backscatter diffraction (EBSD) and Raman spectroscopy.

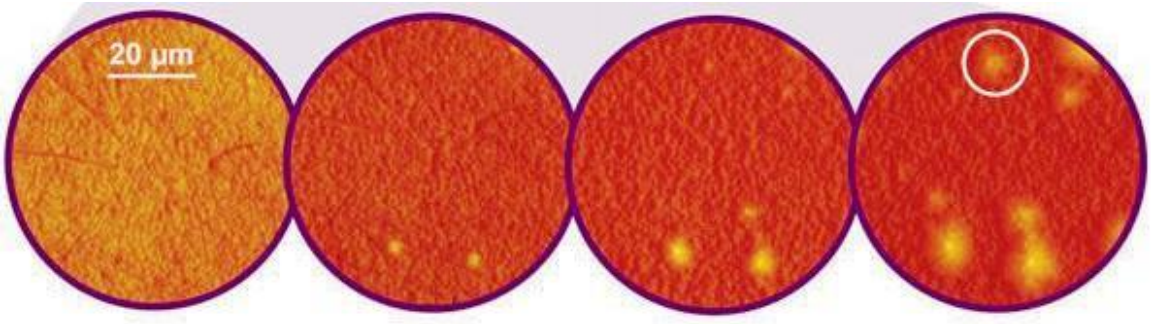


Figure 7: Nucleation-and-growth process observed by optical interferometry (the circled area indicates a monoclinic spot). (Source: Chevalier et al. [63]).

Authors found that the monoclinic layer expands continuously and linearly into the depth of the material with increasing time (Figure 8). Results proved that reported saturation limitations with time are only due to the limited individual penetration depth of the analytical tool used, e.g., XRD or Raman spectroscopy and that certain fraction of grains within the transformed layer will remain untransformed.

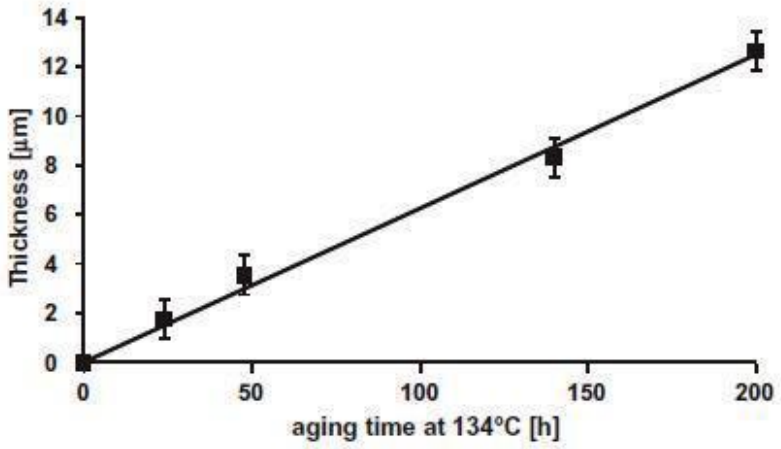


Figure 8: Transformed layer thickness determined in FIB cuts of 3Y-TZP versus ageing time at 134°C. (Source: Keuper et al. [64]).

1.5.2 Nucleation of LTD

The nucleation of LTD will start on the grains which are less stable, i.e. they are larger in size [65]–[67], contain less yttria [65]–[68] or they are exposed to higher internal stresses. The existence of critical grain size, below which the *t-m* transformation is not possible, is still debated [63], but the crucial role of the grain size on the hydrothermal stability of 3Y-TZP is recognized. As illustrated in Figure 9, the grain size increases with increasing sintering temperature. Materials sintered at different temperatures show different ageing behaviour (Figure 10). It should be mentioned, however, that decreasing of grain size has a beneficial effect on the hydrothermal stability, but it compromises the fracture toughness of tetragonal zirconia [69]. Coarser-grained Y-TZP ceramics, namely, exhibit higher fracture toughness, but lower ageing stability compared to that of fine-grained material.

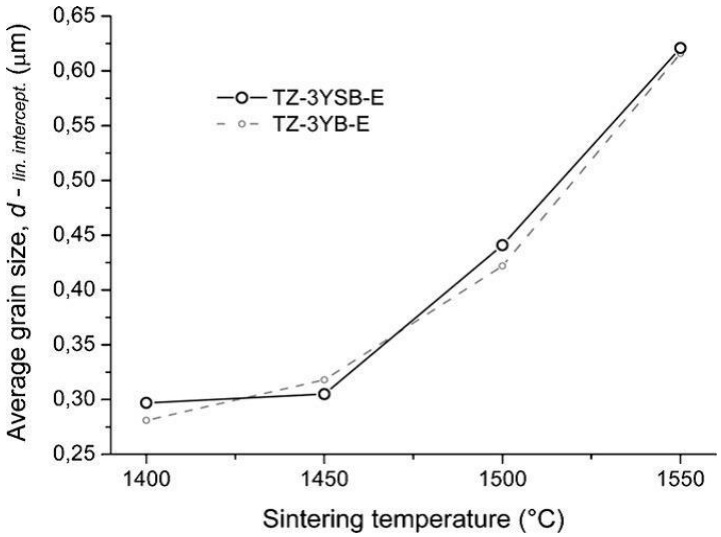


Figure 9: Sintering-temperature-dependent average grain sizes of TZ-3YB-E and TZ-3YSB-E ceramics evaluated by using the linear interception method (Source: Kosmač et al. [70]).

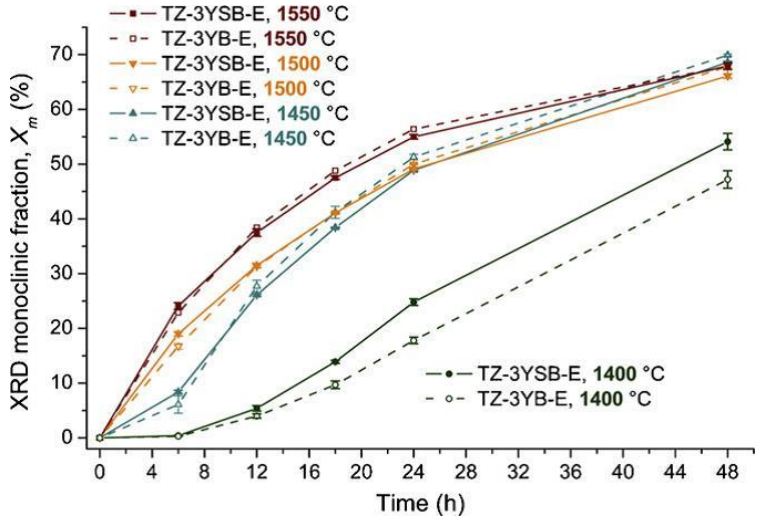


Figure 10: Calculated fraction of monoclinic zirconia (Xm) versus accelerated in vitro ageing time for the TZ-3YSB-E and TZ-3YB-E ceramic surfaces, sintered for 2 h in the temperature range 1400–1550 °C (Source: Kosmač et al. [70]).

Furthemore, because 3Y-TZP ceramics are typically sintered in a bi-phasic, *t*+*c* region of zirconia-yttria phase diagram (Figure 2), higher sintering temperatures are not only result in larger grains, but also in a higher degree of phase partitioning into the equilibrium assemblage of *t*+*c* phases, i.e., in a larger relative amount of un-transformable (yttria-rich) *c*-ZrO_2 co-existing in equilibrium with the more readily transformable (yttria-lean) *t*-ZrO_2. Matsui et al. [71] reported that the amount of cubic zirconia in 3Y-TZP sintered at 1300 °C was 12.7 mass% and reached 18.6 mass% when the sintering temperature was 1500 °C. These values were determined by X-ray diffraction and Rietveld calculations. In addition, the distribution of the Y^{3+} ions inside the zirconia grains after sintering at 1300 °C was nearly homogeneous, while Y^{3+} ions appeared to concentrate at the grain boundaries after sintering at higher temperatures. Matsui et al. [72] also showed that cubic phase regions start to form at grain boundaries and triple grain junctions, where the Y^{3+} ions had segregated. In the SEM micrograph of 3Y-TZP cubic grains in phase partitioned ceramics can be distinguished, because they are larger (typically 2-3 µm) than the tetragonal grains. Ruiz et al. [69] observed the bimodal

microstructure in 3Y-TZP (HSY-3, Zirconia Sales of America, Atlanta) sintered at 1550 °C for 2 h (Figure 11a). However, sintering under the same conditions of 3Y-TZP powder, produced a decade later by Tosoh (Japan) resulted in unimodal microstructure (Figure 11b). Longer annealing time (1550 °C for 5 h) was needed to achieve the bimodal microstructure in this material. Chevalier et al. [73] using the atomic-force microscopy (AFM) analysis of aged surface of 3Y-TZP has shown that the yttria-lean tetragonal grains, neighbouring to large cubic grains, act as a sites for the nucleation of the *t-m* transformation, reducing the overall resistance to LTD of the as-sintered, coarser-grained 3Y-TZP ceramics.

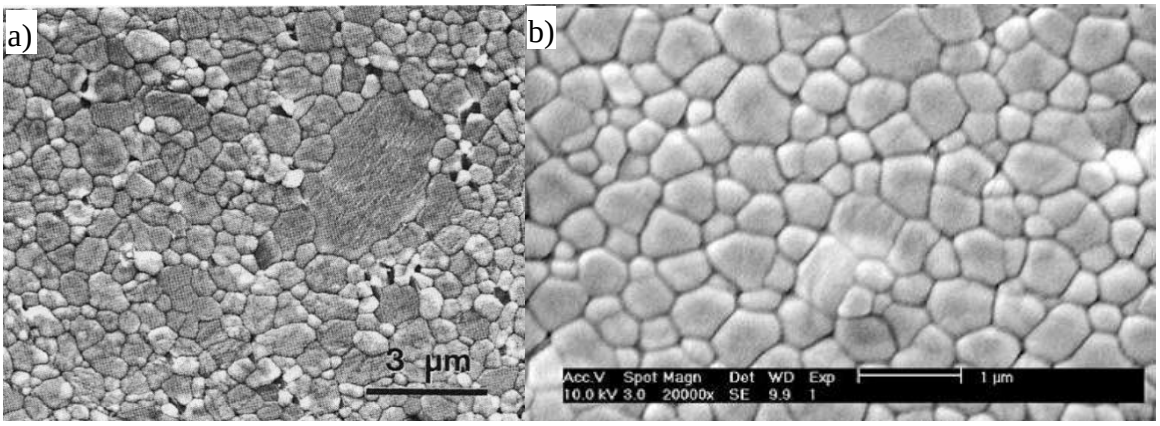


Figure 11: SEM micrographs of sintered at 1550 °C for 2 h 3Y-TZP powders produced by (a) Zirconia Sales of America, Atlanta (source: Ruiz et al. [69]) and (b) Tosoh, Japan. (Source: Chevalier et al. [73])

In 1986 Schmauder and Schubert [74] suggested that the *t–m* transformation will not start in stress-free grains, but at the grain boundaries or grain corners, where high internal stresses are localised. These stresses arise upon cooling due to the thermal expansion anisotropy of tetragonal zirconia. Later Deville et al. [75] using the AFM analysis confirmed that the transformation never initiates in the middle of a grain, but martensite almost always appears at triple grains junction at first (Figure 12).

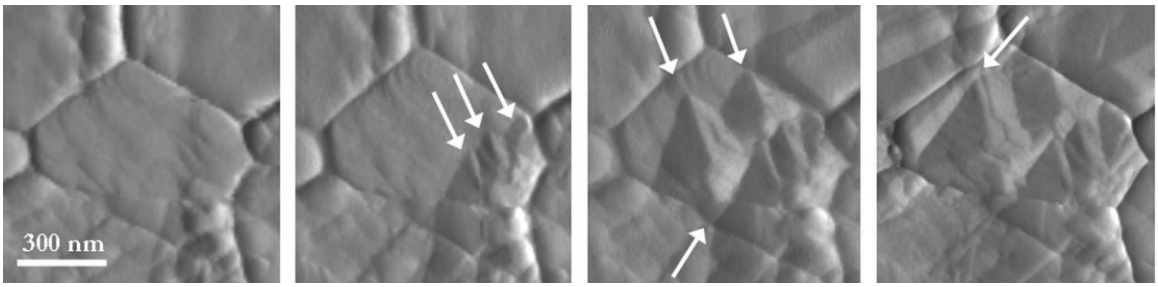


Figure 12: Progressive transformation of a grain in 3Y-TZP. The first variants (arrow) appeared at a grain boundary triple junction (Source: Deville et al. [75]).

1.5.3 Propagation of LTD

Considering the very large shear strain (~16%) and volume increase (~4%) accompanying the *t–m* phase transformation, very large stresses appear in the surrounding zones of a transformed grain. Because of these stresses, untransformed *t*-zirconia will be more prone to *t–m* transformation. This is the so-called autocatalytic effect, in which the transformation of one grain accelerates the transformation of neighbouring grains. Due to volume expansion associated with the transformation the propagation of LTD leads to a surface roughening and extensive microcraking. The latter opens the path for water to

penetrate into the bulk of material, and even accelerates the ageing as schematically illustrated in Figure 13.

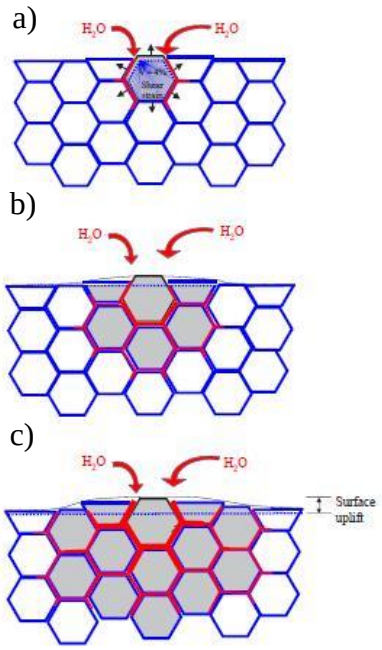


Figure 13: Scheme of the ageing process occurring in a cross section, showing the transformation neighbor to neighbor. (a) Nucleation on a particular grain at the surface, leading to microcracking and stresses to the neighbors. (b) Growth of the transformed zone, leading to extensive microcracking and surface roughening. Transformed grains are gray. Red path represents the penetration of water due to microcracking around the transformed grains. (Source: Chevalier et al. [76]).

1.5.4 Role of water

A series of papers were published with an attempt to explain, how the presence of water can promote the LTD, however, after more than 30 years of research, the exact mechanism is still not well understood.

The effect of various types of solvents (aqueous and nonaqueous) on the ageing of 3Y-TZP has been studied. Sato et al. [77] reported that the addition of acid or base into the water does not influence on the rate of LTD. In contrast, Kosmač et al. [78] found that *t*-zirconia ceramics are more susceptible to low temperature degradation in an acidic environment than in alkaline environment.

Lange et al. [79] observed $Y(OH)_3$ crystallites in the hydrothermally aged Y-TZP ceramics and suggested that hot water has a potential for leaching of yttrium, which may induce transformation on the ceramic surface. However, the dissolution of Y^{3+} in water could not be confirmed by the chemical analysis of the solvent [68]. Moreover, Kim et al. [80] noted that if LTD leads to a loss of yttrium, then the aged and transformed back into the tetragonal structure 3Y-TZP should experience an even more extensive degradation. Since the subsequent ageing induced even less monoclinic phase, the Lange's et al. theory was seriously questioned.

Sato et al. [68], [81] suggested that LTD is controlled by the reaction for the breakage of the Zr-O-Zr bond to form Zr-OH bonds. However, this model cannot rationalize the composition and grain size dependence of the degradation rate.

Yoshimura et al. [82] also proposed the chemical sorption of water to form Zr-OH and/or Y-OH as the first step of water attack. Using the infrared spectroscopy the

introduction of OH^- in the lattice of *t*-zirconia and exclusion of OH^- by re-heating were shown. These results were confirmed by Raman spectroscopy.

Later several experimental results showed that during the LTD water radicals are indeed penetrating the lattice of the *t*-zirconia [83], [84]. Shubert et al. [83], using the isotope marking for both hydrogen and oxygen, showed that the depth of water penetration after autoclaving for 2 h at 200 °C of 3Y-TZP sintered at 1400 °C is about 500 nm. The concentrations of hydrogen and oxygen are similar and both are in the order of the vacancy concentration of the material. This emphasizes the primary role of oxygen vacancies initially present in Y-TZP. Moreover, the activation energy for LTD is comparable to that for the ionic conduction of 3Y-TZP at temperatures below 500 °C which was reported as 88-89 kJ/mol [85]–[87], regardless of the amount of dopants and grain size. This suggests that LTD is related to a lattice relaxation process which is induced by thermally activated oxygen vacancy diffusion.

The penetration of water species in zirconia lattice and the primary role of oxygen vacancies in the LTD process are now generally accepted. However, the nature of diffusing water radicals is still under discussion. Although it has been suggested that the diffusing species may be a charged oxygen molecules O_2^- [88], the majority of papers assume that the diffusing species is the OH^- ion.

The reaction of water with zirconia in terms of OH^- ions as the diffusing species has been formalized in the literature, in the Kroger-Vink notation [89]:

$$H_2O + V_O^{\cdot\cdot} + O_O^x = 2(OH)_O^{\cdot}, \qquad (6)$$

where $(OH)_O^{\cdot}$ are proton defects.

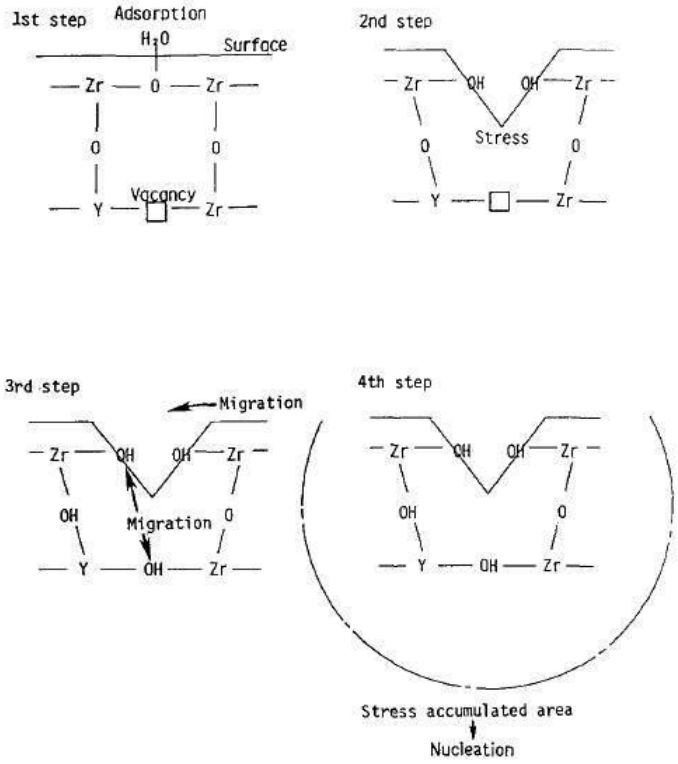


Figure 14: Proposed degradation process of Y-TZP by H_2O: 1) the adsorption of water to form Zr-OH 2) reaction of water with Zr-0-Zr bonds to form two Zr-OH groups 3) the migration of OH^- species in the lattice 4) the accumulation of stresses and as a result the nucleation of LTD. (Source: Yoshimura et al. [82])

Another issue still requiring clarification is the mechanism by which the filling of oxygen vacancies results in destabilization of the tetragonal phase. Fabris et al. [90] suggested that the decrease of oxygen vacancies content, by itself accounts for the destabilization. Based on Eq. (6) the following sequence of mechanisms was proposed [91]–[93]: (1) chemical adsorption of H_2O on ZrO_2 surface, (2) reaction of H_2O with O^{2-} on the ZrO_2 surface to form hydroxyl groups OH^-, (3) penetration of OH^- into the inner part probably by grain boundary diffusion, (4) annihilation of oxygen vacancies by OH^-, (5) when the oxygen vacancy concentration is reduced so that the tetragonal phase is no longer stable, a tetragonal to monoclinic transformation occurs.

An alternative process proposed independently by other authors is a stress driven transformation. Yoshimura et al. [82] were the first to propose that the migration of OH^- species at the surface and in the lattice leads to the accumulation of stresses (Figure 14). In this regard, some authors claim that exposure to moisture increases lattice parameters of the tetragonal phase, while others claim that lattice parameters decrease under the same conditions. Shubert et al. [83] suggested that the penetration of water radical leads to a lattice contraction and in a strain hindered situation—such as the surface near region—the contraction leads to the formation of tensile stresses that destabilize the *t* phase by reducing ΔU_{SE} in Equation 2.

1.5.5 Ways to improve the LTD stability

In a review paper «What future for zirconia as a biomaterial?» [76] Chevalier et al. came up with a self-explaining Table 1: summarizing the potential effects of the different stages of processing on the microstructure and, consequently, LTD stability of biomedical grade 3Y-TZP ceramics.

As it was already mentioned, increasing the Y_2O_3 content and/or decreasing the grain sizes substantially improves resistance to ageing, but it will inhibit the *t-m* transformation and thus decrease the fracture toughness of the material.

Table 1: Potential effect of the different process stages on the microstructure of zirconia ceramics. (Source: Chevalier et al. [76])

Processing stage	Potential effect on the microstructure
Initial powder	Yttria content and distribution, presence of additives (leading to secondary phases)
Forming	Pore distribution of green compacts, and consequently porosity of final components
Sintering temperature and duration	Density, grain size, amount of cubic phase
Cooling rate after sintering	Phase partitioning, residual stresses
Hot isostatic pressing	Density, phase assemblage, increase of oxygen vacancies content, residual stresses
Whitening	Decrease of oxygen vacancies, modification of residual stresses
Grinding and machining	Surface roughness, residual stresses, initial monoclinic content
Cleaning, sterilization	Initial content of monoclinic phase

While preserving the mechanical properties the addition of dopants appears to be the most effective way to decelerate the LTD. Effect of a number of oxides on the hydrothermal stability of Y-TZP has been extensively studied. Among tested oxides, only a few provide a satisfactory balance between ageing resistance, mechanical properties and biocompatibility.

Generally, dopants are present in zirconia either as a second phase or they form a solid solution. They influence the sintering rate, grain morphology, and microstructure and as a result they change the mechanical properties and the hydrothermal stability of zirconia. As it was already mentioned, substitution of Zr^{4+} by divalent or trivalent cations would produce oxygen vacancies to maintain the charge balance and decelerate the LTD [59]. The tetravalent dopants, in particular Ce^{4+}, are also known to improve the ageing resistance [60]. Adding ceria to a Y-TZP increases the grain size [94]–[96], but improves the ageing resistance of the material [96]–[98]. For it ageing resistance Ce-TZP is already used for dental applications.

Among all insoluble dopants alumina should be mentioned first. It is already used in commercial biomedical-grade 3Y-TZP powders in order to decelerate the LTD [99]–[101]. 3Y-TZP powders, such as E-types or Zpex (High translucent grade) from Tosoh, Japan, contain 0.25 and 0.05 wt. % of alumina, respectively. Small amounts of alumina not only suppress the ageing process but also lowers the sintering temperature and improves the mechanical properties of the 3Y-TZP [101]–[103]. Since its solubility in zirconia is known to be limited [104], the individual alumina grains within zirconia matrix are usually observed in the microstructure of ceramics prepared from 0.25 wt% alumina containing powders (Figure 15).

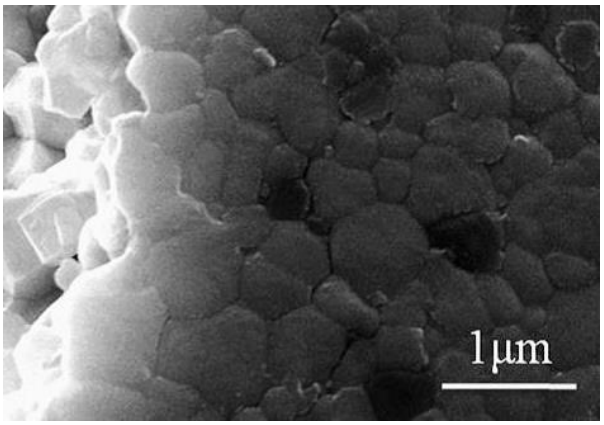


Figure 15: SEM micrograph of 3Y-TZP containing 0.25 wt% alumina (Source: Wu et al. [101]).

Matsui et al. [72] showed that alumina tends to segregate at the grain boundaries of 3Y-TZP. However, the issue of whether or not Al^{3+} traces are present in the grain interiors remains unclear. Ross et al. [100] using the energy-dispersive X-ray spectroscopy (EDS), electron energy loss spectroscopy (EELS) and secondary ion mass spectrometry (SIMS) analysis revealed that Al^{3+} segregate to the grain boundaries, but traces Al^{3+} were also found in the grain interiors. Because of uncertainties in the microstructure of alumina-containing 3Y-TZP, the mechanism by which alumina improves the ageing properties of 3Y-TZP has not been fully clarified. It is thought that Al^{3+} cations with their smaller ionic radius and a lower valence than the host Zr^{4+} cations, produce oxygen vacancies to maintain the charge balance.

Zhang et al. [48] studied the influence of alumina content on the LTD of 3Y-TZP and showed that only the segregated Al^{3+} at the grain boundary of zirconia is effective to decelerate the degradation of *t*-zirconia. The individual alumina grains could induce

residual stresses during cooling due to the mismatch of thermal expansion between the alumina and zirconia. Since the thermal expansion coefficient of zirconia ($11 \times 10^{-6}K^{-1}$) is higher than for alumina ($8 \times 10^{-6}K^{-1}$), the zirconia phase will be under a net hydrostatic tensile stress which favours the *t*–*m* transformation. Thus, 0.25 wt.% alumina was found to have a higher degradation retarding effect to Y-TZP ceramics than 2 and 5 wt.% of alumina additions.

Nogiwa-Valdez et al. [105] used alumina and lanthana as dopants to 3Y-TZP as an effective strategy to significantly decelerate the hydrothermal degradation kinetics, without considerably modifying the density, grain size or fracture toughness. Both dopants were found to segregate at the grain boundaries and thereby preventing the nucleation of new monoclinic nuclei after 3 h of exposure and substantially limiting propagation of the transformation, both across the surface and into the bulk, also resulting in suppressed grain boundary microcracking. It was claimed that the strategy of introducing additions of lower valence cations that segregate to the grain boundary provides a promising method of reducing sensitivity to hydrothermal degradation without any reduction in fracture toughness.

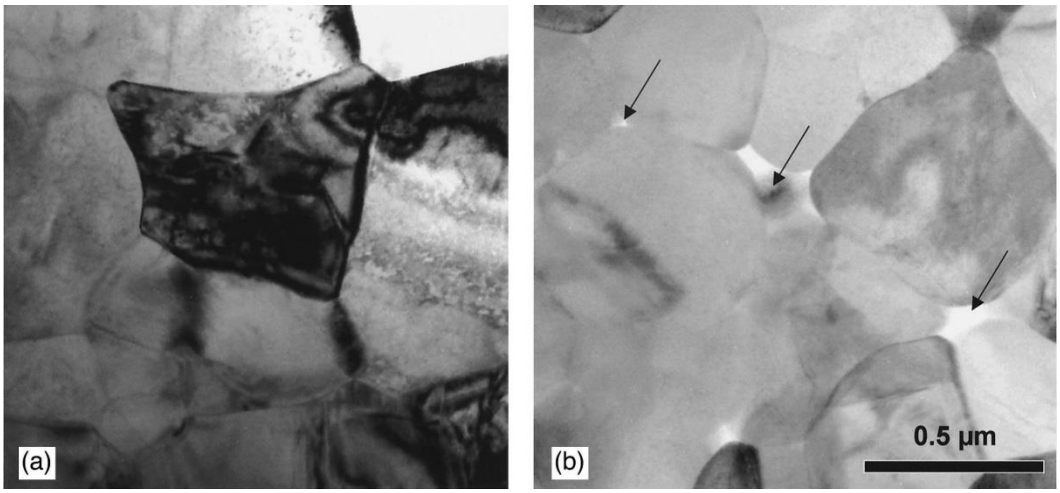


Figure 16: TEM micrographs of (a) silica-free and (b) silica-containing 3Y-TZP material, showing faceted grains for pure material and round grains with smal amorphous pockets (see arrows) for 3Y-TZP/SiO_2 material (Source: Gremillard et al. [106]).

Silica is another attractive dopant for the stabilization of 3Y-TZP is silica. Gremillard et al. [106], [107] has reported that minor addition of silica (up to 0.5 wt.%) to 3Y-TZP results in an improved resistance to ageing without affecting the mechanical properties. Silica-doped 3Y-TZP ceramic was prepared by addition of colloidal silica to the zirconia slurry with following drying and sintering at 1450 °C for 5 h in air. TEM analysis of obtained samples revealed that the amorphous silica phase located at multiple grain junctions makes the grains rounder, and so reduces the cooling residual stresses and the stress concentrations at the grain triple points (Figure 16) [106]. This was confirmed by XRD measurements of internal stresses performed for undoped samples and silica-containing samples. Results showed that the addition of silica reduces the internal stresses (Figure 17): they may be twice as large in the pure material than in the silica-containing 3Y-TZP (mean least-squares fitting of the Williamson–Hall plot leads to a mean deformation of 0.5% for the pure material and 0.35% for the silica-containing material).

Furthermore it was suggested that silica could reduce the stresses arising due to the *t*-*m* transformation and limit the growth of monoclinic nuclei thereby slowing down the LTD process by hindering its propagation.

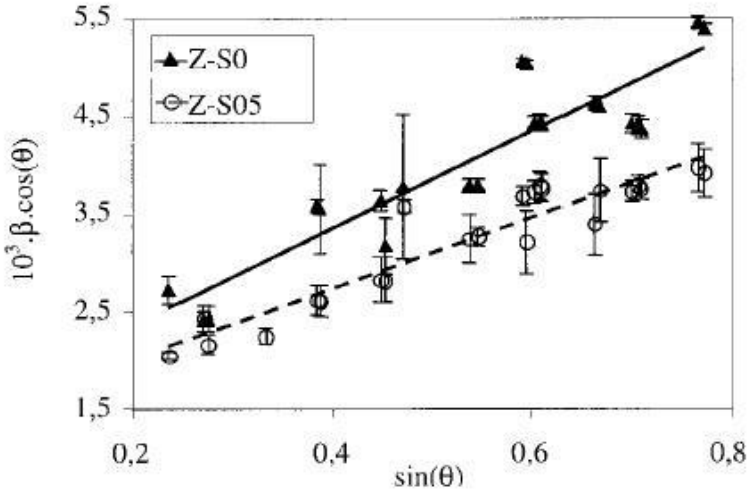


Figure 17: Williamson–Hall plot of (Z-S0) pure and (Z-S05) silica-doped 3Y-TZP, showing that Z-S0 material exhibits more internal stresses than Z-S05 material (Source: Gremillard et al. [106]).

The effect of sintering temperatures on the stability of silica-doped 3Y-TZP and the effect of alumina and silica co-doping on the hydrothermal stability of 3Y-TZP was not studied yet. The first commercially available Y-TZP powders always contained small amounts of silica. Therefore it was hard to differentiate between individual contributions of dopants to the properties of tetragonal zirconia. In 1990, Tsubakino et al. [99] studied the effect of alumina addition on the *t-m* transformation of 3Y-TZP. Since the starting material contained 0.1 wt% of SiO_2 authors assumed that yttria-containing $A1_2O_3$-SiO_2 phase will be formed at the grain boundaries and as a result Y_2O_3 content in tetragonal grains should decrease resulting in destabilization of tetragonal phase. However, the tetragonal phase in 3Y-TZP containing 0.1 wt% of SiO_2 and Al_2O_3 was much more stable compared to alumina-free 3Y-TZP, disproving the initial assumption. Therefore an alternative explanation was suggested: the formation of the phase containing Y_2O_3, $A1_2O_3$, and/or SiO_2 at grain boundaries may induce a much stronger cohesion between grains in 3Y-TZP containing $A1_2O_3$ than that between grains in 3Y-TZP. If the cohesion between grains increases, a constrained effect from the surrounding matrix will act strongly to prevent the formation of monoclinic phase. However, authors did not provide any experimental evidences.

2 Aims and Hypothesis

The main goal of this work was to expand the current knowledge of the low-temperature degradation (LTD), i.e., ageing, of 3 mol % yttria-doped tetragonal zirconia polycrystalline (3Y-TZP) ceramic. LTD is spontaneous tetragonal-to-monoclinic (*t–m*) transformation, taking place under hydrothermal conditions. This process is accompanied by intensive microcracking in the transformed zone that may ultimately lead to the degradation of mechanical properties and thereby preventing a use of 3Y-TZP in dental applications. For its unique combination of excellent mechanical properties and biocompatibility the 3Y-TZP ceramic is nowadays widely used as an aesthetic core material in restorative dentistry. LTD has been extensively investigated for more than three decades, but the phenomenon is still not well understood. The same holds for the role of dopants, including alumina, although it is used in most commercially available 3Y-TZP products. Special emphasis was given to the role of silica or/and alumina-(co)-doping in the nucleation and propagation of the LTD. While it is generally accepted that silica, located at triple grain junctions, reduces the internal stresses occurring at grain edges by making grains rounder, the review of the literature relating to the role of alumina gives the impression of a much more confused state of affairs. To the best of our knowledge the combining effect of alumina and silica co-doping on the ageing behaviour of 3Y-TZP has not been systematically investigated so far, although these two dopants may have complementary mechanism associated with the deceleration of ageing. Assuming that no reactions between the two dopants will occur during sintering of 3Y-TZP, it can be expected that alumina and silica co-doping will give the synergistic effect on the LTD stability of ceramic without compromising the strength and fracture toughness.

In order to differentiate between the distinct contributions of the two dopants to the overall resistance to ageing, the specimens were prepared by infiltration of silica sol into pre-sintered, porous 3Y-TZP discs, which contained 0.00, 0.05 and 0.25 wt. % of alumina. The infiltration technique was chosen for co-doping, since it could be easily included in the CAD/CAM (computer-aided design and computer-aided manufacturing) technology commonly used in the production of dental 3Y-TZP restorations. Since this way of adding silica has never been used before, the first part of my work was aimed at verifying the viability and of the process and its optimization. After the final sintering at temperatures ranging between 1400 °C and 1600 °C for 2 h, the ceramic specimens were characterized in terms of their microstructure, phase composition, mechanical properties and accelerated ageing behaviour. Since the nucleation of the LTD is known to occur at the grain boundaries and triple grain junctions, the characterization of grain boundaries by the impedance spectroscopy and comparison of the fracture modes of pure and doped 3Y-TZP materials was expected to give better insight into the possible mechanism associated with the deceleration of LTD by alumina or/and silica-doping, and because it is expected that both dopants will influence both the nucleation, as well as the propagation of hydrothermal *t–m* transformation. FIB-SEM technique will be employed to study the microstructural features in the transformed layer of pure and (co)doped samples. Knowing that 3Y-TZP ceramics are sintered in a bi-phasic, tetragonal+cubic region, higher sintering temperatures are expected to result not only in grain coarsening, but also

in a larger relative amount of un-transformable (yttria-rich) *c*-ZrO_2 coexisting in equilibrium with the more readily transformable (yttria-lean) *t*-ZrO_2, which, in turn, may additionally reduce the overall resistance to LTD of the as-sintered, coarser-grained material. Besides, in light of the ongoing debate, whether upon cooling the partitioned un-transformable (yttria-rich) phase is cubic or *t'*-ZrO_2, special care will be devoted to characterization of phases in materials subjected to accelerated ageing under extreme conditions, leading to the saturation of the monoclinic phase. Finally, the role of silica and alumina co-doping on the phase partitioning in 3Y-TZP is not known. A ternary ZrO_2-Y_2O_3-SiO_2 phase diagram does not exist and the effect of alumina on the reactivity of this system is not clear. Therefore, selected coupled-diffusion experiments in 3Y-TZP/SiO_2 and 3Y-TZP/SiO_2/Al_2O_3 systems at 1450-1500 °C will be carried out in order to explore the reactivity in these systems.

3 Materials and Methods

3.1 Materials

Three commercially available, ready-to-press 3Y-TZP powders (Tosoh, Japan) were used for the preparation of the specimens. The chemical composition of these powders, as obtained from the supplier, and their abbreviations used in present study are given in Table 2. All the powders contain 3–4 wt. % of an acrylic binder, but they differ slightly in their composition and, to a larger extent, in their specific surface area: a standard-grade (pure) TZ-3YB with a specific surface area of ~16 m^2 g^{-1}; a low alumina- (~ 0.05 wt. %) but slightly higher yttria-containing biomedical grade TZ-PX-242A, with a specific surface area of ~12 m^2 g^{-1}; and a high alumina- (~ 0.25 wt.%) but slightly lower yttria-containing biomedical grade TZ-3YSB-E, with the lowest specific surface area of ~7 m^2g^{-1}. Due to its higher translucency, the TZ-PX-242A grade is nowadays used in the fabrication of porcelain-free FPDs, while from the TZ-3YSB-E powder grade a somewhat more opaque dental ceramic is produced that needs veneering.

Table 2: Chemical composition of the 3Y-TZP powders as obtained from the commercial suppliers, expressed as wt. %, specific surface area (m^2/g).

Powder grade[a]	Abbreviations	Y_2O_3	Al_2O_3	SiO_2	Fe_2O_3	Na_2O	Specific surface area (m^2/g)
TZ-3YB	TZ	5.21	0.005	0.002	0.002	0.019	16
TZ-PX-242A	0.05A-TZ	5.36	0.05	0.002	0.002	–	12[b]
TZ-3YSB-E	0.25A-TZ	5.15	0.25	0.002	0.002	0.006	7

[a]Tosoh, Japan

[b]In-house measured value

3.2 Preparation of Specimens

3.2.1 Preparation of biscuit-sintered ceramics

Since its development in 2001 [108], direct oversize milling of Y-TZP blanks has become increasingly popular in dentistry and is now the most common method in the fabrication of individual Y-TZP cores for all-ceramic dental restorations. These blanks are prepared through uniaxially pressing the 3Y-TZP powders followed by cold-isostatical pressing (CIP) and pre-sintering.

To simulate the industrial production of porous, soft machinable blanks in the present work 3Y-TZP powders were dry pressed at 150 MPa into disks (~20 mm in diameter and ~2 mm in thickness), followed by CIP at 200 MPa and biscuit-firing up to start densification. The shrinkage of powder compacts depended on the chemical composition and on the specific area of granulated Y-TZP powders, therefore shrinkage onsets were evaluated from the dilatometric curves (Table 3). The low-specific-surface-area 0.25A-TZ material had higher shrinkage temperature as compared to those of finer TZ and 0.05A-

TZ materials. Since the slight differences were observed between the shrinkage temperatures of TZ and 0.05A-TZ powders, both materials were pre-sintered at 900 °C for 2 h, while 0.25A-TZ material was pre-sintered at 1000 °C for 2 h.

Table 3: The temperature of shrinkage onset for TZ, 0.05A-TZ and 0.25A-TZ powders evaluated from the dilatometric curves.

Powder	Onset of shrinkage (^{o}C)
TZ	~ 930
0.05A-TZ	~ 940
0.25A-TZ	~ 1030

3.2.2 Characterization of biscuit-sintered materials

The relative densities and the pore size distribution for the pre-sintered compacts were determined using mercury injection porosimetry (MIP). The volume of mercury required to fill all accessible pores is considered the total pore volume. Dividing this value by the mass of the sample gives total specific pore volume. If the sample contains no blind pores and all pore space is filled, the volume of mercury intruded into the pores subtracted from the bulk volume of the sample gives its true volume (the volume only of the solid material, excluding the volume of open pores and closed pores). Skeletal densities follow from dividing the material mass by volume.

The total volume of pores and the total porosity were determined using coupled Pascal 140 + 440 porosimeters by Thermo Electron - Porotec. The Pascal 140 porosimeter was utilized for low-pressure measurements below 100 kPa. The Pascal 440 porosimeter works within the pressure range from 10 kPa to 400 MPa. All mercury porosimetry analyses were performed using operating procedures, which was suggested by the manufacturer.

The pressure values can be converted into pore diameters using the Laplace–Washburn equation:

$$d = -\frac{4\gamma cos\theta}{P}, \qquad (7)$$

where d is the pore diameter, γ is the interfacial tension between the solid matrix, mercury and vacuum and is assumed to correspond to a value of 0.48 N· m^{-1}, θ is the contact angle, P is the applied pressure.

3.2.3 Infiltration and sintering

For the preparation of silica-doped 3Y-TZP by the infiltration method silicon alkoxides $Si(OR)_4$ seem to be the most attractive as a SiO_2 precursor for their alkoxide groups (-OR), which react readily with water in the presence of a mineral acid or a base as a catalyst. The hydrolysis reaction replaces –OR with hydroxyl groups (-OH) followed by the subsequent condensation reaction with the formation of siloxane bonds (-Si-O-Si), which upon oxidation give SiO_2. Another way to obtain SiO_2 is by simple decomposition of $Si(OR)_4$ at elevated temperatures. Therefore silica-containing 3Y-TZP can be prepared by immersion of pre-sintered preforms into pure or prehydrolysed $Si(OR)_4$. In the present work both methods were tested to find the optimized conditions for the infiltration. The dynasylan (Dynasylan® 6490, Evonik, Germany) was used as a SiO_2 precursor. This is a vinyl silane concentrate (oligomeric siloxane) containing vinyl and methoxy groups. The pre-sintered 0.25A-TZ specimens were randomly divided into two groups. One group of samples was soaked in pure dynasylan for 5 min, while the other group was soaked in silica sol, synthesized *in situ* using the sol–gel method through the hydrolysis of a

dynasylan. In the latter case specimens were immersed in a mixture of absolute ethanol and dynasylan solution, and the hydrolysis was carried out by the drop-wise addition of aqueous ammonia (25 wt.%) at room temperature. The specimens were infiltrated in 1 cycle, which involved soaking for 30 and 60 min. Thereafter all specimens were rinsed with the ethanol, dried at room temperature for 2 h and in dry set at 60 °C for 3 h.

In order to determine the appropriate sintering conditions for obtained specimens the temperature behaviour of dynasylan should be known. The oxidation of dynasylan leads to the formation of volatile coproducts, which could destroy the tetragonal zirconia ceramic upon sintering. Therefore the thermogravimetric and differential thermal analysis (TGA/DTA) of infiltrated with dynasylan and dried 3Y-TZP sample was performed on a Netzsch STA 409 C/CD instrument at a heating rate of 5°C/min in static air over a temperature range 30-900 °C. Infiltrated with pure or prehydrolyzed dynasylan 3Y-TZP samples were slowly heated (120 °C/min) to pyrolysis temperature. The resulting weights of the preforms were measured with an analytical balance (± 0.0001 g) before and after the infiltration–drying–pyrolysis cycle. The difference being the amount of silica introduced during the infiltration. To compare the effect of different ways of infiltration on the microstructure and mechanical properties, finally sintered at 1450 °C for 4 h samples were studied in terms of microstructure (SEM), phase composition and verified for flexural strength.

The optimised conditions for the infiltration were used to prepare silica-containing TZ, 0.05A-TZ and 0.25A-TZ samples. The infiltrated samples were finally sintered at 1400-1600 °C for 2 h together with the controls. Both the heating and cooling rates were 5 °C/min.

3.3 Characterization of Sintered Materials

3.3.1 Density and microstructure

The relative density of the sintered disks was determined with Archimedes' method using distilled water as the immersion liquid. The relative densities were calculated by adopting a theoretical density of ρ_T = 6.08 g/cm^3. Five discs of each group were measured and the mean values and the corresponding SD were calculated.

The grain size evaluations were taken from field emission scanning electron micrographs FE-SEM (Jeol JSM-7600F, Japan) of polished (3 μm diamond paste) and thermally etched (1350 °C, 10 min) specimens using the planimetric method (with the ImageJ software). EDS spectra were conducted in specific regions for a 30 kV voltage, for 5 min, to obtain well-resolved Y–K_α and Zr–K_α peaks.

The specimens for TEM (Jeol JEM-2100) were prepared by cutting 3-mm diameter discs from the ceramic bodies. These discs were reduced to ~120 μm by grinding. A region about 20-μm thick at the centre of the disc was produced using a dimple grinder. Finally, the specimens were thinned by argon-ion erosion at 4 kV with an incident angle of about 10 °.

3.3.2 Phase composition

XRD patterns were recorded using PANalytical X'Pert PRO MPD diffractometer, fitted with an X'Celerator detector. Variable anti-scatter and divergence slit of 10 mm were used together with a beam mask of 10 mm. As-sintered specimens' surfaces were exposed to Cu-Kα X-ray radiation (Cu$K\alpha_1$, λ = 1.5406 Å). The data were collected over a range of 25–140° 2θ using a 0.017 ° step and 400 s/step. XRD data peak fitting was performed

using DiffracPlus EVA (Brüker, version 12.0 rev 0) software. The presence of tetragonal, monoclinic and cubic zirconia was confirmed according to the Powder Diffraction File database, maintained by the International Center for Diffraction Data (ICDD PDF-2) (Card Nos. 01-079-1771, 00-036-0420 and 00-003-640, respectively).

Selected samples were additionally characterised by Raman spectroscopy system (Horiba Jobin Yvon). 514.5 and 632.81 nm excitation lines of Ar and He-Ne lasers respectively were used.

3.3.3 Mechanical properties

3.3.3.1 Biaxial flexural strength

The biaxial flexural strength of the sintered disks before and after 24 h of ageing (10 for each material) was measured using a universal testing machine (Galdabini Quasar 50, Italy) in piston-on-three-ball test (ISO 6872) at a loading rate of 1 mm/min. The discs were symmetrically supported by three balls at one plane and loaded by a piston in the center of the opposite plane (Figure 18). The balls measure 3.2 mm in diameter and are placed in a circular configuration with the diameter of 11 mm. The piston has a diameter of 1.4 mm.

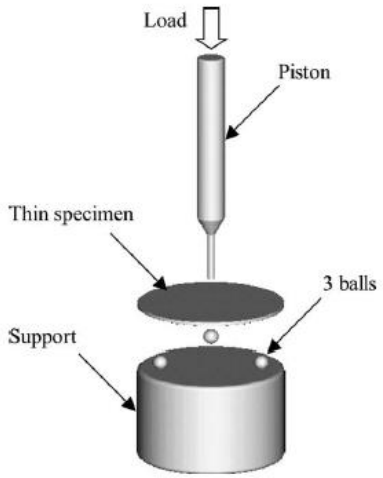


Figure 18: Piston-on-3-ball experimental configuration.

The samples were loaded until failure occurred and the force was registered in Newtons (N). The recorded value was inserted into equation derived by Shetty et al. [109]:

$$\sigma = -0.2387F(X - Y)/d^2, \quad (8)$$

where σ presents biaxial flexural strength, F is the force at failure, d is the thickness of the sample (mm). The X and Y are:

$$X = (1 + \nu)ln\frac{r_2}{r_3}^2 + (\frac{1-\nu}{2})(\frac{r_2}{r_3})^2, \quad (9)$$

$$Y = (1 + \nu)[1 + \ln(\frac{r_1}{r_3})^2] + (1 - \nu)(\frac{r_1}{r_3})^2 \quad (10)$$

Here ν is the Poisson's ratio for Y-TZP, r_1 is the diameter of supporting circle (mm), r_2 is the diameter of the piston (mm), r_3 is the diameter of the sample (mm).

3.3.3.2 Hardness and fracture toughness

Vickers indentation tests were used for the hardness and fracture-toughness evaluations. The hardness tests were performed at a load of 10 N. The toughness was calculated directly from the crack lengths produced by the Vickers indentation at a load of 100 N.

An average value was obtained from 10 indentations. The fracture toughness was calculated using the equation given by Niihara for Palmqvist cracks [110]:

$$K_{IC} = 0.35(l/a)^{1/2}\left(\frac{H}{Ef}\right)^{-\frac{2}{5}}\left(\frac{Ha^{\frac{1}{2}}}{f}\right), \quad (11)$$

where H is the hardness, E is the Young's modulus, f is the constant, l is the radial cracks size, a is the indent half diagonal.

3.3.4 Impedance measurements

The impedance measurements were conducted with Solartron 1260 frequency response analyser on air in the temperature range of 120-440 °C and at frequencies 0.1-106 Hz with amplitude 100 mV. Platinum paste was used to fabricate the electrodes. Both sides of the pellets were completely covered with the paste (~1 mm thickness) and annealed at 800 °C for 1 h.

The measurements were performed using a standard 4-terminal technique. From the measured impedance spectra the resistance of a high-frequency and low-frequency impedance arcs, R(HF-arc) and R(MF-arc), were extracted by fitting the spectra using the ZView 2 software. Based on the literature survey the HF-arc and MF-arc were ascribed to the resistance of the bulk of grains R_{bulk} and the resistance of grain boundaries R_{gb} respectively. In addition to the values of the resistances R_{bulk} and R_{gb}, the fitting procedure gives the values of Q and α parameters of the corresponding CPE elements (CPE_{bulk} and CPE_{gb}) coupled in parallel with the two resistive contributions. From the value of R_{bulk} and known geometry of the pellet, the bulk resistivity can be calculated using the following expression:

$$\rho_{\text{bulk}} = \frac{R_{\text{bulk}} \cdot A}{l}; \quad (12)$$

where A is the pellets' cross section and l is the thickness. The effective capacitances C_{eff} were calculated by using the parameter values of the two CPE elements using the general expression:

$$C_{\text{eff}} = (R^{(1-\alpha)}Q)^{1/\alpha}. \quad (13)$$

Time constant of the process τ, which can be described equivalently by parallel coupling of the resistive and capacitive elements can be expressed as an RC product. For the used CPE elements, corresponding value of C_{eff} is used instead of capacitance C. Finally grain-boundary resistivity ρ_{gb}, is obtained from the equation:

$$\rho_{\text{gb}} = \frac{\tau_{\text{gb}}}{\tau_{\text{bulk}}}\,\rho_{\text{bulk}}. \quad (14)$$

Activation energies for bulk and grain-boundary conductivities are obtained from the corresponding $\ln(\rho)$ versus $1/T$ plots using Arrhenius type of equation.

3.3.5 Optical properties

To study the effect of silica on the transmittance of 3Y-TZP materials 1.5 mm thick 0.05A-TZ and 0.05A-TZ/SiO_2 disks sintered at 1450 °C for 4 h were prepared and mirror polished from both sides. Transmission measurements were made in the wavelength

range of 300 nm to 800 nm using the Perkin-Elmer instrument.

3.3.6 In-vitro ageing

No surface treatment, such as grinding and/or polishing, was applied to the specimens' surface before the *in vitro* ageing experiments. To study the effect of alumina or/and silica-doping on the LTD stability of 3Y-TZP, all samples sintered at 1450 °C were sequentially (incrementally) autoclaved in distilled water under isothermal conditions at 134 °C for 6–48 h. To study the effect of sintering temperatures on the ageing behaviour of alumina or/and silica doped 3Y-TZP, samples sintered at 1400-1600 °C for 2 h were aged for 24 h at 134 °C.

XRD patterns were recorded using Endeavor D4 (Bruker AXS) diffractometer equipped with a SOL'X detector. *In-vitro* aged specimens' surfaces were exposed to Cu-Kα X-ray radiation ($CuK\alpha_1$, λ = 1.5406 Å). X-ray diffraction patterns were collected in the 25–40 °2θ range using 0.020 ° step. XRD data peak fitting was performed using DiffracPlus EVA (Brüker, version 12.0 rev 0) software. The presence of tetragonal and monoclinic zirconia was confirmed according to the Powder Diffraction File database, maintained by the International Center for Diffraction Data (ICDD PDF-2) (Card Nos. 01-079-1771 and 00-036-0420, respectively).

The relative amount of the transformed monoclinic zirconia phase (m-ZrO_2) on all the surfaces was determined from the integral intensities of the monoclinic $(\bar{1}\ 1\ 1)_m$ and $(1\ 1\ 1)_m$, and the tetragonal $(1\ 0\ 1)_t$ peaks according to the method of Garvie and Nicholson [22]:

$$X_m = \frac{I^m_{111} + I^m_{\bar{1}11}}{I^m_{111} + I^m_{\bar{1}11} + I^t_{101}} \qquad (15)$$

Three samples were used for each measrument. The error bars were estimated from standard deviation.

XRD analysis is a non-destructive method, allowing the monitoring of LTD evolution on one specimen. However, only the surface is characterized (typical depth of a few micrometers), and thus this method is unable to provide any information when the transformation propagates deeper into the bulk. It is also not very precise for monoclinic contents lower than 5%, making it unsuitable for monitoring the beginning of the transformation.

It is however possible to detect lower monoclinic fractions in thin surface layer by using XRD at grazing incidence angles (1–5° 2θ). The penetration depth of X-rays ranges from ~5 μm at 30° to ~0.3 μm at 1° with the copper K_α radiation [63]. Through the use of this property, several measures at different incidence angles also give access to the depth profile of the monoclinic concentration.

It should be noted here that according to the binary phase diagram [14] the materials were sintered in the t+c two-phase region. Considering the composition and the sintering temperatures the Scott's phase diagram suggests that up to about 24% of untransformable phase with the reminder transformable tetragonal phase can be present in materials. Within this work the selected materials were aged until the saturation with the monoclinic phase and the amount of untransformable phase was determined from integral intensities of the monoclinic $(\bar{1}\ 1\ 1)_m$ and $(1\ 1\ 1)_m$, and the tetragonal $(1\ 0\ 1)_t$ peaks according to the method of Garvie and Nicholson.

Another method to quantify the progress of the transformation with time is Raman spectroscopy. In zirconia, the monoclinic content is given by a ratio between the intensities of the monoclinic peaks (~181 and 192 cm^{-1}) and the tetragonal peaks (~148 and 264 cm^{-1}):

$$R_m = \frac{I^m_{181}+I^m_{192}}{I^m_{181}+I^m_{192}+0.97(I^t_{148}+I^t_{264})}. \quad (16)$$

Compared to XRD analysis Raman spectroscopy is more sensitive to smaller traces of monoclinic phase. Micro-Raman spectroscopes are now available in confocal configurations: Confocal Raman microscopy offers three-dimensional mapping of both monoclinic content and stress state, with a micrometer resolution along the three axes. Although less widely used than XRD, Raman spectroscopy is one of the most powerful tools for characterizing zirconia LTD.

However, like XRD, Raman techniques have a very limited depth of penetration and these methods are unable to provide any further information when the transformation propagates deeper into the bulk.

The third way to monitor the progress of LTD is analysing cross sections of aged material using the optical interferometer (OI) or FIB/SEM technique.

To study the progress of the LTD into the bulk the cross-sections of the samples (sintered at 1450 °C and 1600 °C and additionally aged up to 72 h and 120 h respectively) were polished and studied by OI.

A study of the sub-surface microstructures of selected aged 3Y-TZP ceramics was carried out using FIB-SEM dual beam system (FEI Helios Nanolab 650), that comprises a SEM for imaging of sample surface and ion beam for etching or machining. A 0.5 µm thick platinum film was first deposited onto a ceramic surface, where the cross section was intended to be made, using ion beam assisted gas injection system at 30 kV and 0.43 nA to protect the area of interest from the formation of extensive curtain effect. The regular cross sections were then made using ion beam machining at 30 kV and 65 nA and were finalized by ion polishing at 30 kV and 21 nA. As-prepared cross sections were observed in situ, under an angle of 52°, using the electron probe at 2 kV and 100 pA.

4 Results

4.1 Preparation of Specimens

4.1.1 Characterization of pre-sintered 3Y-TZP

The relative densities, pore size and porosity of the pre-sintered at 900 °C (TZ, 0.05A-TZ) and 1000 °C (0.25A-TZ) preforms are listed in Table 4. The 0.05A-TZ indicate superior pressing and sintering ability of the low alumina "high translucency" powder grade resulting in the highest relative density after the pre-sintering stage, as compared to the other two powder grades. TZ material showed slightly higher porosity and slightly lower density as compared to 0.25A-TZ. The pore size distributions for all materials are shown in Figure 19.

Table 4: Results of a mercury porosimetry measurements.

	Density (TD, %)	Pore size (nm)	Porosity (%)
TZ	48.7	47.1	49.3
0.05A-TZ	53.4	50.7	45.7
0.25A-TZ	49.3	112	48.6

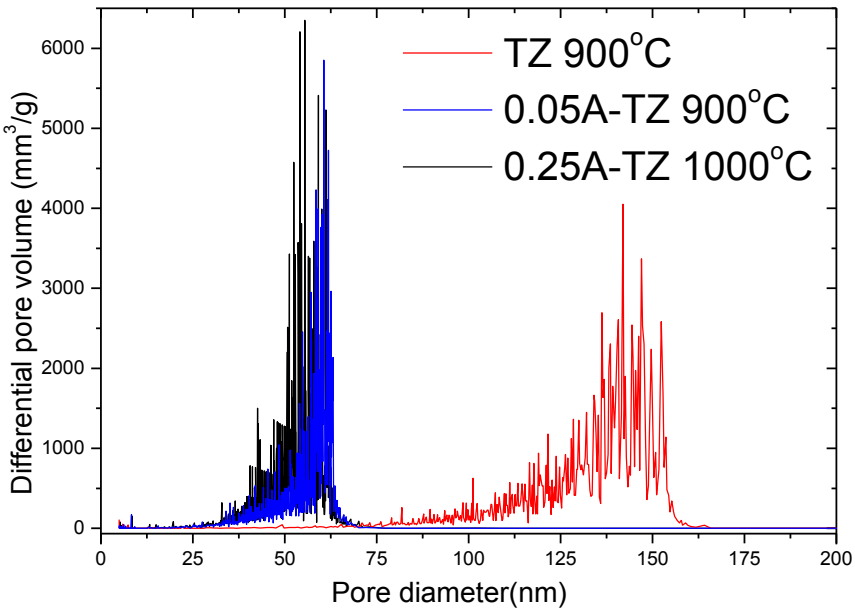


Figure 19: Pore size distribution measured by mercury intrusion porosimetry for TZ and 0.05A-TZ materials pre-sintered at 900 °C and 0.25A-TZ material pre-sintered at 1000 °C.

4.1.2 Elaboration of infiltration technique

Pre-sintered 0.25A-TZ samples were divided into two groups. One group was soaked in

pure dynasylan for 5 min, while the other group was soaked in prehydrolyzed dynasylan solution for 30 and 60 min. Thereafter all specimens were rinsed with the ethanol, dried at room temperature for 2 h and in dry set at 60 °C for 3 h. Figure 20 shows the result of TGA/DTA analysis of soaked in dynasylan and dried 0.25A-TZ sample.

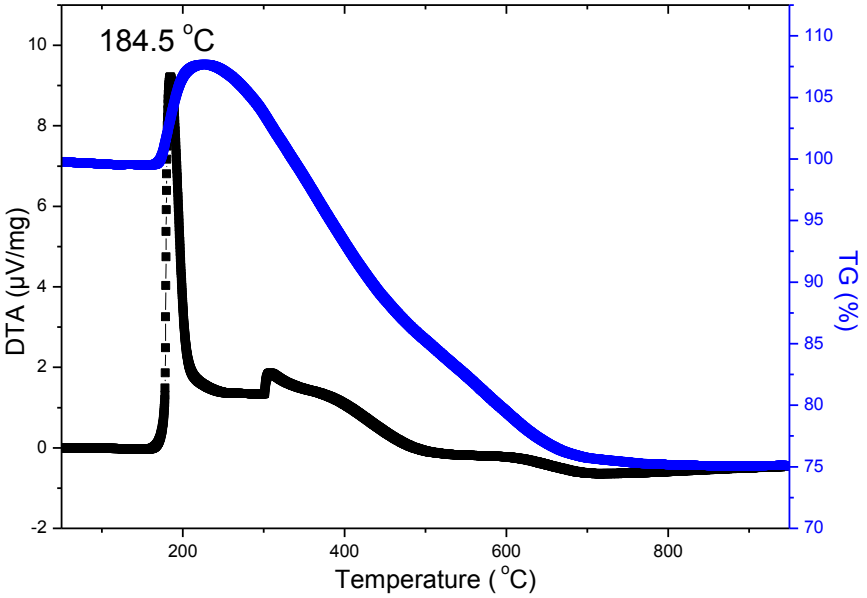


Figure 20: TGA/DTA analysis of soaked in dynasylan and dried 0.25A-TZ sample.

The weight of specimen initially increased and achieved the maximum at ~185 °C. Since analysis is performed in air, oxygen can react with the double bond between two carbon atoms in dynasylan with the formation of epoxide groups. Upon heating at higher temperature of 185 °C the weight of sample decreased and achieved the constant value at ~ 800°C. Based on the obtained results the following conditions were used for the sintering of infiltrated with pure or prehydrolysed dynasylan 3Y-TZP materials:

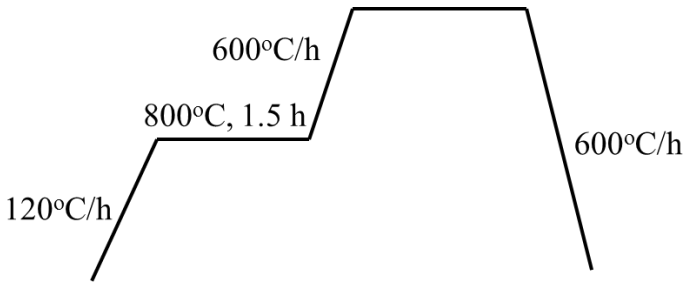


Figure 21: Sintering program used for silica-doped TZ, 0.05A-TZ and 0.25A-TZ materials.

Up to 800 °C the slow heating rate (120 °C/min) was applied to prevent the disintegration of silica-doped samples due to the release of volatile compounds.

The soaking of pre-sintered tetragonal zirconia in pure or hydrolyzed dynasylan for different times followed by sintering at 1450 °C for 4 h resulted in materials with different phase compositions and related mechanical properties. The representative XRDs, Raman and SEM micrographs are shown in Figure 22-Figure 24. The soaking in pure dynasylan for 5 min resulted in the formation of zirconium silicate $ZrSiO_4$ during the sintering, leading to low flexural strength of 3Y-TZP (Table 5). The soaking of pre-sintered blanks in hydrolyzed dynasylan for 1 h followed by drying and final sintering leads to the formation of crystabolite, which reduses the flexural strength of material. The reducing of soaking time to 30 min results in monolithic tetragonal zirconia blanks with

sufficiently high flexural strength.

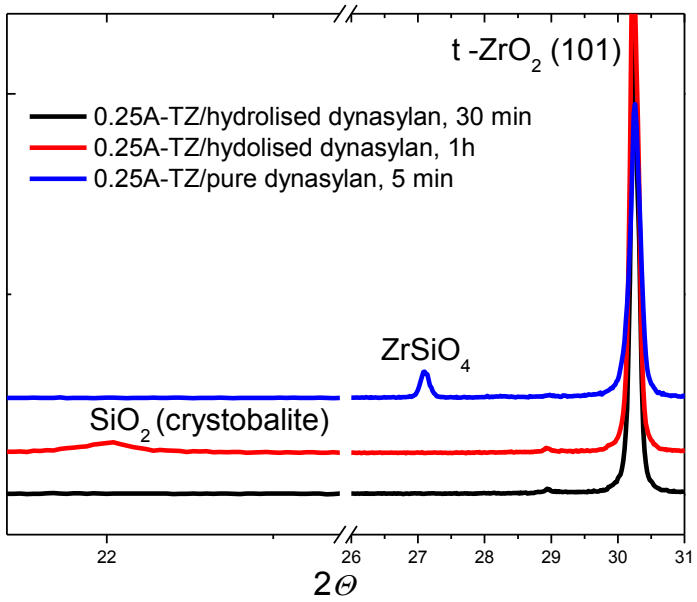


Figure 22: XRD patterns collected from the 0.25A-TZ/SiO_2 samples, obtained by the soaking of pre-sintered TZ in pure dynasylan for 5 min; prehydrolysed dynasylan for 30 min and prehydrolysed dynasylan for 60 min followed by final sintering at 1450 °C for 4 h.

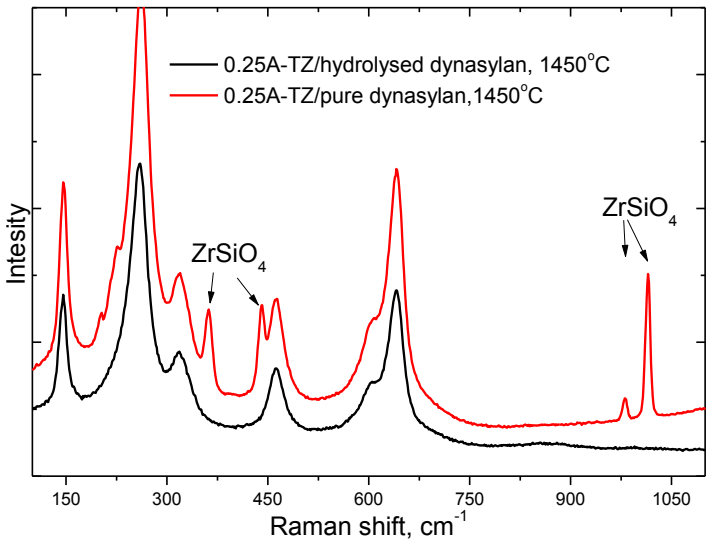


Figure 23: Raman spectra of 0.25A-TZ/SiO_2 samples, obtained by the soaking of pre-sintered 0.25A-TZ in (a) pure dynasylan for 5 min (b) prehydrolysed dynasylan for 30 min and finally sintered at 1450 °C for 4 h.

Table 5: Flexural strength of 0.25A-TZ material infiltrated with pure dynasylan, hydrolised dynasylan for 30 and 60 min and finally sintered at 1450 °C for 4 h.

Infiltration	Flexural strength, MPa
Pure dynasylan, 5 min	543±8
Hydrolised dynasylan, 30 min	1412±93
Hydrolysed dynasylan, 60 min	924±68

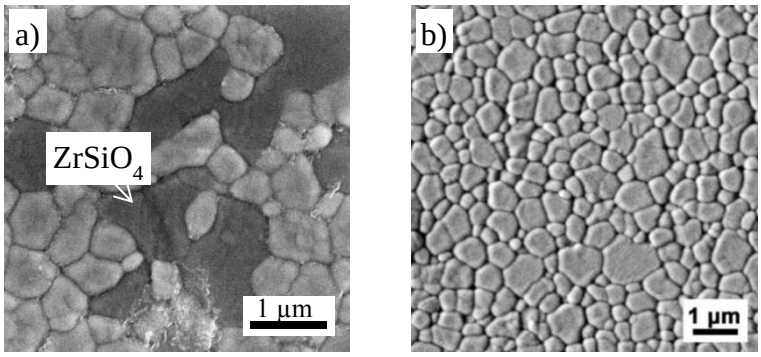


Figure 24: Scanning electron micrographs of 0.25A-TZ specimens infiltrated using (a) pure and (b) prehydrolyzed dynasylan and sintered at 1450 °C for 4 h.

The homogeneity of silica distribution in sintered ceramics was qualitatively verified using SEM analyses performed on ion-polished cross-sections (Figure 25). No significant differences in the amount of silica-rich triple junction pockets were observed between the bulk and the near-surface region for 2-millimeter thick samples.

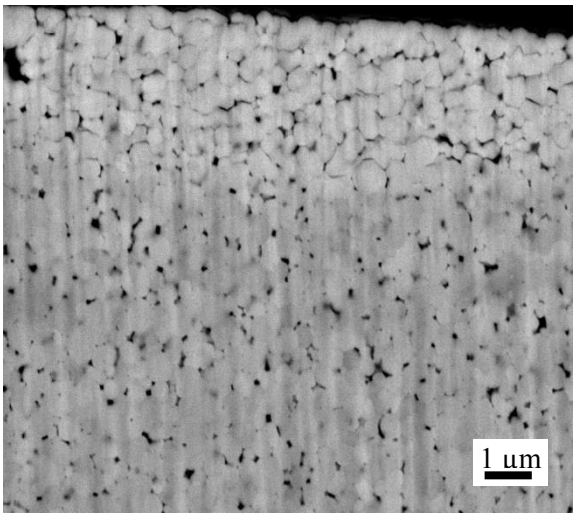


Figure 25: FIB-SEM cross-section of the 24-hours aged 0.25A-TZ/SiO_2 specimen.

The optimised conditions for the infiltration (soaking in prehydrolysed dynasylan for 30 min) were then used for the preparation of the silica-doped TZ, 0.05A-TZ and 0.25A-TZ samples. The gravimetrically determined content of silica in the infiltrated disks was ~0.25 wt.% for the TZ and 0.25A-TZ specimens and ~0.15 wt.% for the 0.05A-TZ. The lowest amount of infiltrated silica (~0.15 wt.%) in the 0.05A-TZ material compared to ~0.25 wt.% for the TZ and 0.25A-TZ specimens was attributed to the highest relative density of this pre-sintered material.

4.2 Characterisation of Sintered Alumina or/and Silica-Doped 3Y-TZP

After final sintering at 1400-1600 °C for 2 h pure and silica-doped TZ, 0.05A-TZ and 0.25A-TZ specimens were verified for density, microstructure, phase composition (XRD, Raman), flexural strength, Vickers hardness and indentation toughness. Selected alumina- and alumina-silica-co-doped 3Y-TZP materials were additionally studied impedance spectroscopy.

4.2.1 Microstructural analysis

All the sintered samples were nearly fully dense (about 99% TD) (Table 6). The silica-containing specimens show slightly lower density relative to the pure and alumina-doped 3Y-TZP, however (considering a relatively limited number of measurements and accuracy of the measuring method) the differences are likely to be insignificant.

Table 6: Relative densities in percentages of sintered at 1400-1600 °C for 2 h pure and silica-doped TZ, 0.05A-TZ and 0.25A-TZ discs (mean ± SD).

Sintering temperature	TZ	0.05A-TZ	0.25A-TZ	TZ/SiO_2	0.05A-TZ/SiO_2	0.25A-TZ/SiO_2
1400	99.3±0.1	99.4±0.1	–	99.1±0.1	99±0.1	–
1450	99.7±0.1	99.8±0.0	99.8±0.0	99.4 ±0.2	99.5±0.1	99.1 ± 0.2
1500	–	99.8±0.1	–	–	–	–
1550	99.8±0.1	99.8±0.1	99.8±0.1	–	99.3±0.3	–
1600	99.8±0.1	99.8±0.1	99.8±0.1	98.8±0.2	99.3±0.2	98.9±0.2

SEM micrographs obtained from the sintered and thermally etched surfaces of silica-free and silica-containing TZ, 0.05A-TZ and 0.25A-TZ disks sintered at 1400-1600 °C for 2 h, are shown in Figure 26-Figure 27.

Irrespective of the difference in the chemical composition, the ceramic microstructures after sintering under the same conditions in the temperature range of 1400-1500 °C were practically identical, being uniform with equiaxed grains of similar size without any marked pores or other defects. No isolated alumina grains were observed for all grades of materials sintered at temperatures ≤ 1450 °C, while at higher sintering temperatures clearly discernible, distinct alumina inclusions are present in the 0.25A-TZ (the dashed circles in Figure 26). After sintering at temperatures ≥ 1550 °C, the striking difference in the microstructures for the materials became observable: while the grains in the pure and silica-doped TZ, 0.05A-TZ and 0.25A-TZ materials preserved their size uniformity, the grain size distribution of the 0.25A-TZ/SiO_2 material became bi-modal (Figure 27), with a minor fraction of evidently larger grains surrounded by (about four times) smaller grains of the major fraction. The larger grains are not homogeneous: small grains with a visible inner grain boundary could be observed within these grains. It is interesting to note, that no alumina grains were observed in the microstructure of co-doped material even when it was sintered at 1600 °C (Figure 27).

The average grain sizes for all the grades of material are listed in Table 7. As it was expected the grain sizes of all materials increase with temperature. The values for sintered pure and silica-doped TZ a 0.05A-TZ materials are nearly the same, indicating that small additions of alumina (0.05 wt%) or silica practically have no influence on the grain growth of tetragonal zirconia; the addition of ~0.25 wt.% alumina or co-doping enhances the growth of zirconia grains, especially at temperatures ≥ 1550 °C. After sintering at these temperatures, the overall average grain size in the alumina-doped ceramic was comparable to the average size of the finer grains in co-doped ceramics. Additional EDS analyses performed on the 0.25A-TZ/SiO_2 material sintered at 1600 °C revealed that the larger grains contained a higher yttria content (5–6 mol.%), while a considerably lower yttria content (2.2–2.7 mol.%) was found in the smaller grains.

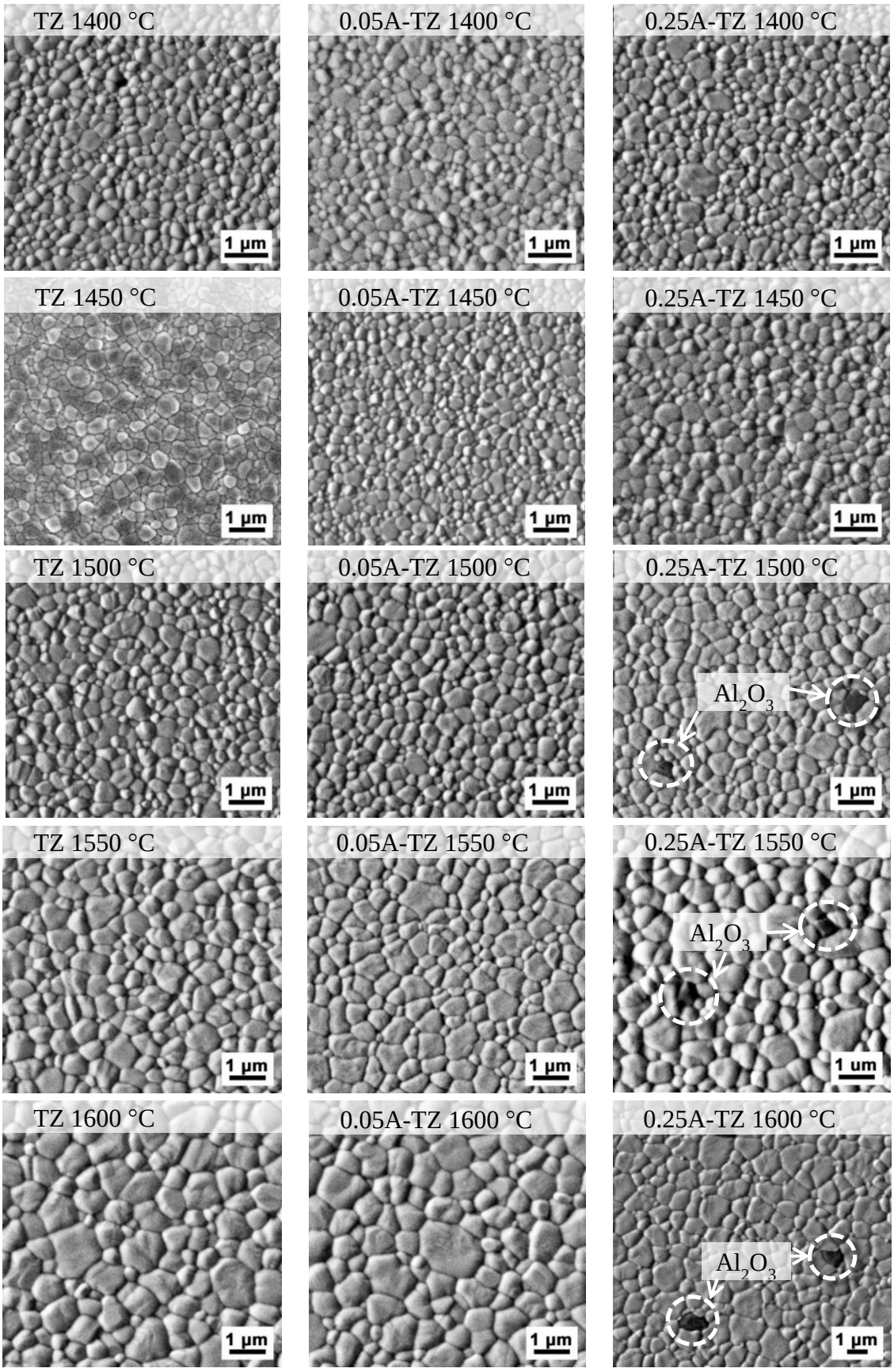


Figure 26: SEM micrographs of polished and thermally etched surfaces of pure TZ, 0.05A-TZ and 0.25A-TZ discs sintered at 1400-1600 °C for 2 h. Dashed circles show alumina grains.

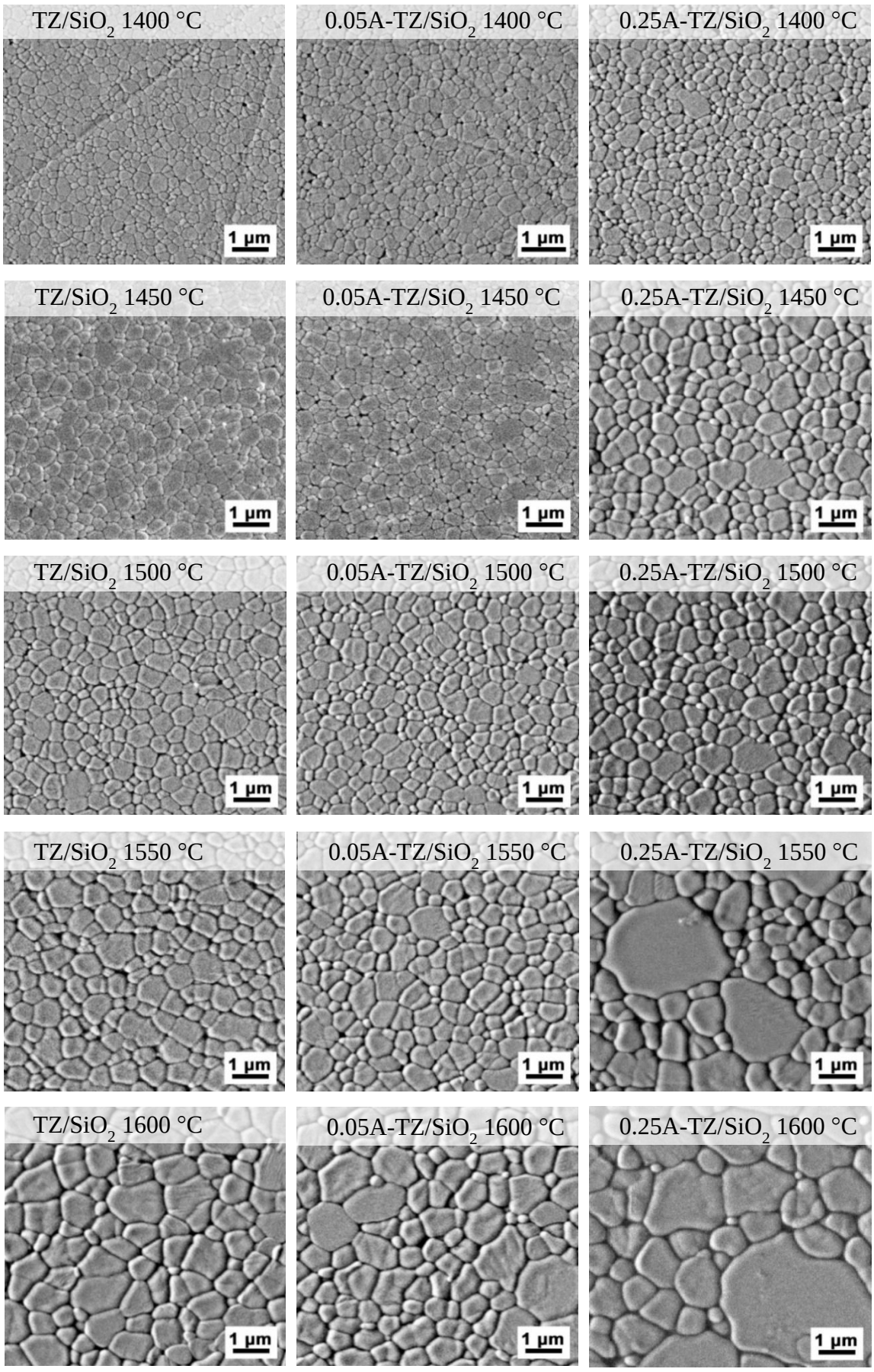


Figure 27: SEM micrographs of polished and thermally etched surfaces of silica-doped TZ, 0.05A-TZ and 0.25A-TZ discs sintered at 1400-1600 °C for 2 h.

Table 7: Average grain sizes in microns of pure and silica-doped TZ, 0.05A-TZ and 0.25A-TZ materials sintered at 1400-1600 °C for 2 h (mean ± SD).

Sintering temperature	TZ	0.05A-TZ	0.25A-TZ	TZ/SiO_2	0.05A-TZ/SiO_2	0.25A-TZ/SiO_2
1400	0.21±0.08	0.28±0.02	0.25±0.09	0.26±0.10	0.27±0.02	0.27±0.10
1450	0.30±0.11	0.29±0.03	0.29±0.03	0.28±0.12	0.30±0.02	0.34±0.13
1500	0.39±0.14	–	0.43±0.13	0.44±0.16	–	0.44±0.16
1550	0.48±0.16	0.44±0.05	0.52±0.15	0.49±0.17	0.41±0.03	0.6 (2.5)*
1600	0.61±0.25	–	0.83±0.23	0.65±0.20	–	0.78±0.20 (3.2)*

*Average grain size representing the fraction of lager grains in the 0.25A-TZ/SiO_2 materials.

While 3Y-TZP samples with no silica exhibited typical faceted grains (Figure 26), in the silica-doped sample the grains' shape was slightly changed, i.e., the edges of the polygonal grains became more rounded, with the pore-like pockets in the triple-grain junctions that can be attributed to silica-rich regions (Figure 27).

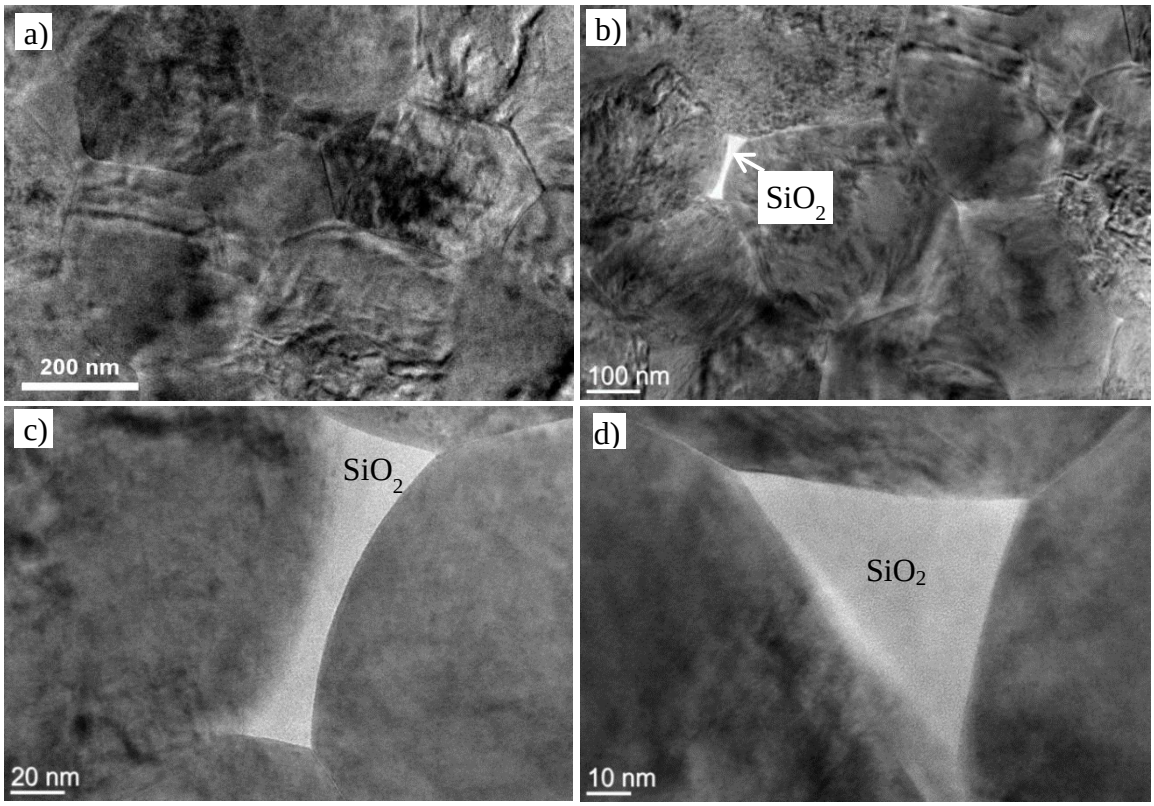


Figure 28: TEM micrographs of (a) 0.05A-TZ and (b-d) 0.05A-TZ/SiO_2 specimens, sintered at 1450 °C.

The findings were further confirmed using a TEM analysis. As shown in Figure 28a, the silica-free sample has grains with edged corners. On the other hand, silica addition resulted in the appearance of an amorphous, silica-rich second phase, positioned mainly at multiple-grain junctions, making the grains rounder in shape (Figure 28 b-d). The crystallinity and composition of this second phase were evaluated by small angle electron diffraction (SAED) and energy-dispersive X-ray spectroscopy (EDS), respectively; it was amorphous and consisted mostly of SiO_2, with some Y_2O_3 and ZrO_2 also present.

The effect of sintering temperature on the position of silica phase was studied by TEM analysis of 0.25A-TZ/SiO_2 samples sintered at 1500-1600 °C. Sintering at temperatures ≥1550 °C resulted in appearance of amorphous silica phase not only at multiple grain

junctions, but also at some grain boundaries (for details see paragraph 5.4).

4.2.2 Phase composition

Figure 29 shows typical XRD profiles of the investigated as-sintered materials (exemplified by 0.25A-TZ/SiO_2). No *m*-ZrO_2 peaks could be found in the patterns obtained from the surfaces of all sintered specimens, implying that they were mainly composed of the *t*-ZrO_2 phase, displaying three characteristic peaks located at 2θ equals 30.2°, 34.7° and 35.2°, corresponding to the *t*(101), *t*(002) and *t*(110) planes, respectively.

XRD analysis clearly shows differences between samples, sintered at different temperatures. Namely, sintering of all the materials at higher temperature of 1450 °C resulted in the appearance on the XRD pattern of additional reflections between the weaker *t*(002) and *t*(110) reflections (Figure 30a). The intensity of this peak increased with temperature for all materials. The only peak was observed between the weaker *t*(002) and *t*(110) reflections for samples sintered at 1450 °C. However, two additional discrete peaks between the same reflections were observed in all materials sintered at temperatures > 1500 °C. A solid confirmation was obtained after inspecting the 72.5–75° 2θ region (plotted in Figure 30b).

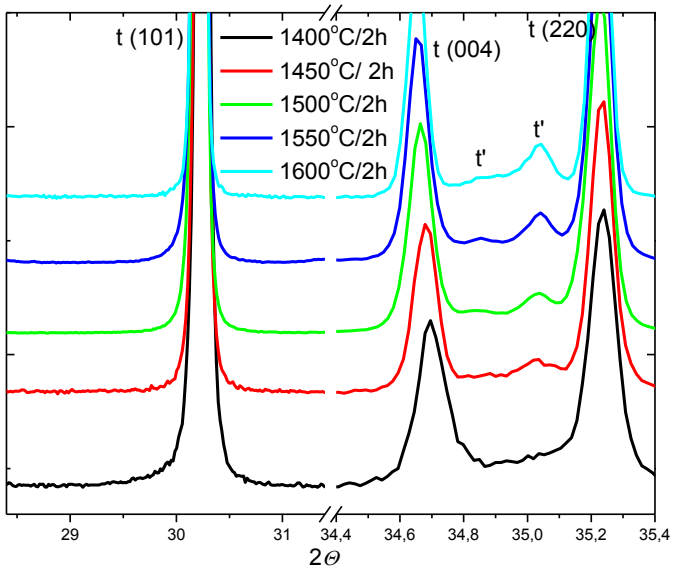


Figure 29: XRD patterns obtained from the 0.25A-TZ/SiO_2 ceramic surfaces, sintered at 1400-1600 °C for 2 h.

The observed two peaks are characteristic of the high temperature, yttria-rich, tetragonal phase, known as *t'*-ZrO_2, which is not transformable to the monoclinic structure. In the specimens sintered at temperatures < 1500 °C practically no differences were observed in the position and shape of the diffraction peak at 30.2° and 35° 2θ. In materials sintered at 1600 °C the lowest intensity of the *t'* peak was observed for the co-doped 0.25A-TZ/SiO_2 material. However, the exact fraction of this phase was not quantified using XRD analysis.

Although individual alumina (α-Al_2O_3) grains were clearly observed on the SEM micrographs of 0.25A-TZ materials, sintered at temperature ≥ 1500 °C, no peaks characteristic for alumina were observed in XRD spectra of the same materials. The amount of α-Al_2O_3 phase in 0.25A-TZ is below the detection limit for XRD. However, it is well known, that the α-Al_2O_3 excited with a 632.8-nm frequency exhibits strong and remarkable fluorescence fine structure at 1370-1410 cm^{-1} range [111], [112].

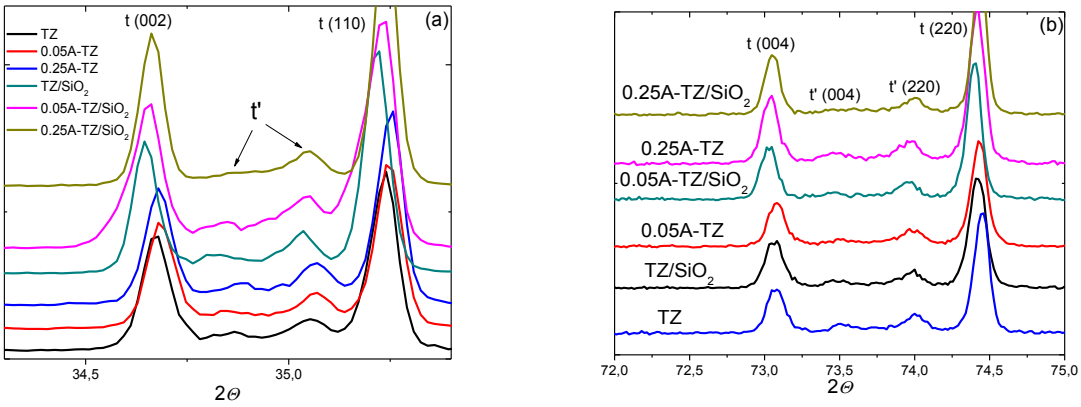


Figure 30: Detailed XRD patterns in (a) 34-35° 2Θ regions and (b) 72-75° 2Θ regions obtained from the pure and silica-doped TZ, 0.05A-TZ and 0.25A-TZ ceramic surfaces, sintered at 1600°C for 2 h.

In a fact, the striking difference was observed between Raman spectra (Figure 31) for 0.25A-TZ and other materials: in addition to signals between 100 and 750 cm^{-1} characteristic for *t*-ZrO_2, there are two strong peaks in 1370-1410 cm^{-1} range of the spectrum of 0.25A-TZ.

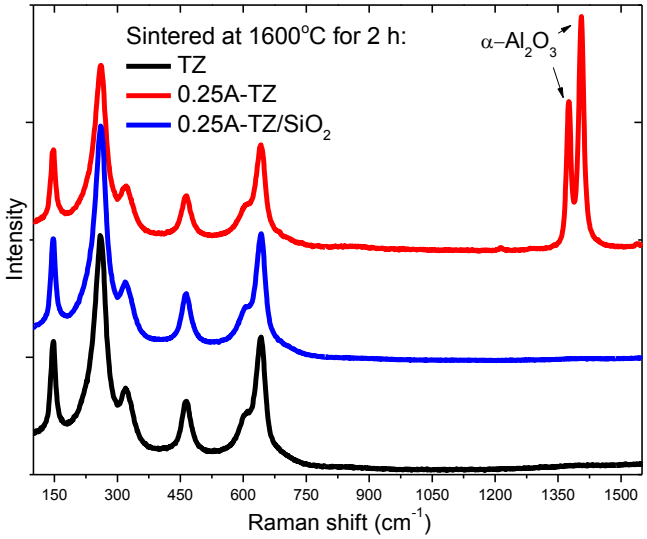


Figure 31: Raman spectra of TZ, 0.25A-TZ and 0.25A-TZ/SiO_2 materials sintered at 1600 °C for 2 h (632.8 nm He-Ne laser).

The luminescence nature of the bands is the most easily detectable by comparison of band positions when different excitation lines are used. When the excitation is changed to a different wavelength the Raman bands shift the same amount correspondingly, while the luminescence lines stay on the same absolute wave number. Therefore, to prove luminescence nature of the bands at 1370-1410 cm^{-1}, 0.25A-TZ sample sintered at 1550°C for 2 h (containing the individual alumina grains in the SEM micrograph (Figure 26) were excited with two different lasers: He-Ne 514.5 nm and Ar-ion 632.8 nm. The obtained spectra are shown in Figure 32. Together with Raman bands in the range of 100 cm^{-1} and 750 cm^{-1}, characteristic for tetragonal phase of 3Y-TZP, in both spectra the luminescence lines in regions from 1370 to 1410 cm^{-1} and from 5000 to 5100 cm^{-1} were observed after excitation with 632.8 and 514.5 nm, respectively. These bands identified as alumina luminescence were very sharp and narrow. Thus, the Raman spectroscopy is an effective tool for the presence of α-Al_2O_3 phase in 3Y-TZP ceramics.

No alumina fluorescence doublet was observed for 0.05A-TZ even when material was sintered at 1600 °C (Figure 33), indicating that this material does not contain α-Al_2O_3 phase.

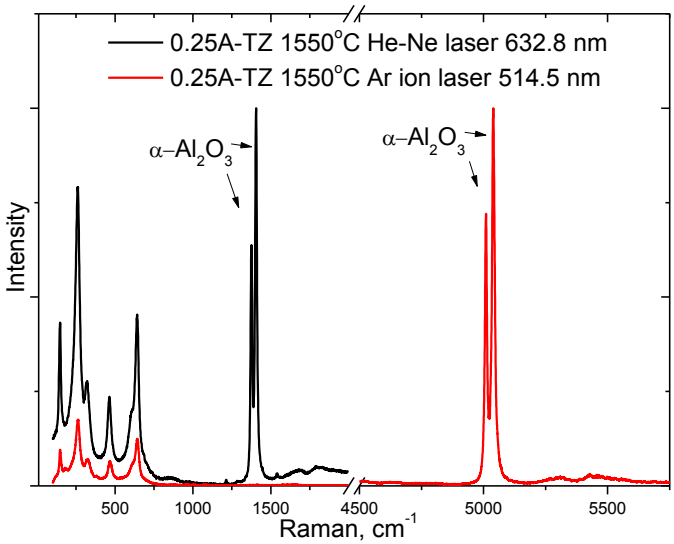


Figure 32: Comparison of Raman and luminescent spectra upon excitation with 514.5 Ar laser and 632.8 nm He-Ne laser.

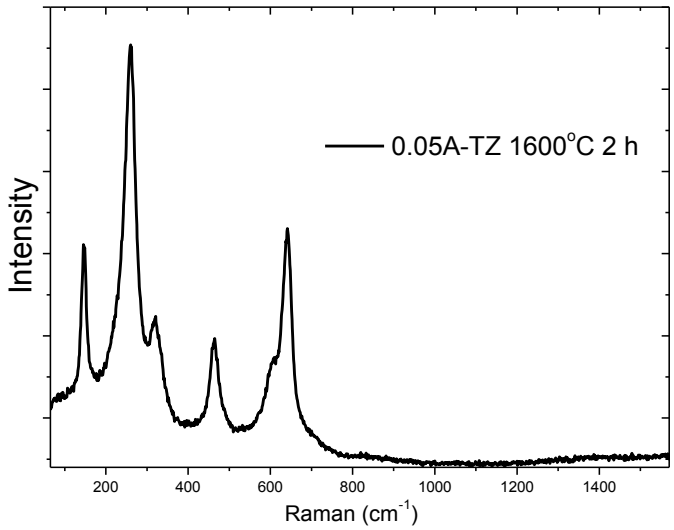


Figure 33: Raman spectra of 0.05A-TZ material sintered at 1600 °C for 2 h (632.8 nm He-Ne laser).

4.2.3 Mechanical properties

The indentation toughness, Vickers hardness and biaxial flexural strength of selected silica-free and silica-doped TZ, 0.05A-TZ and 0.25A-TZ materials are listed in Table 8, Table 9 and Table 10. No significant differences were observed between alumina- and/or silica-doped and undoped 3Y-TZP specimens, except for a slight, but systematic increase in strength with increasing alumina doping.

Table 8: Indentation toughnes of the pure and silica-doped TZ, 0.05A-TZ and 0.25A-TZ materials (mean ± SD).

Sintering temperature	TZ	0.05A-TZ	0.25A-TZ	TZ/SiO_2	0.05A-TZ/SiO_2	0.25A-TZ/SiO_2
1450	4.6 ± 0.2	4.7 ± 0.1	4.9 ± 0.1	4.7 ± 0.1	4.7 ± 0.1	4.6 ± 0.1
1500	–	–	4.8 ± 0.1	–	–	5.2 ± 0.3
1550	–	–	4.9 ± 0.1	–	4.8 ± 0.1	5.2 ± 0.2
1600	–	–	4.8 ± 0.3	4.8 ± 0.1	–	5.8 ± 0.3

Table 9: Hardness of the pure and silica-doped TZ, 0.05A-TZ and 0.25A-TZ materials (mean ± SD).

Sinter. temp.	TZ	0.05A-TZ	0.25A-TZ	TZ/SiO_2	0.05A-TZ/SiO_2	0.25A-TZ/SiO_2
1400	–	15.2 ± 0.2	–	–	14.8 ± 0.5	–
1450	14.5 ± 0.5	15.2 ± 0.5	14.3 ± 0.5	13.9 ± 0.3	14.1 ± 0.4	14.6 ± 0.3
1550	–	–	–	–	13.8 ± 0.4	–

Table 10: Flexural strength of the pure and silica-doped TZ, 0.05A-TZ and 0.25A-TZ materials (mean ± SD).

Sinter. temp.	TZ	0.05A-TZ	0.25A-TZ	TZ/SiO_2	0.05A-TZ/SiO_2	0.25A-TZ/SiO_2
1400	897± 56	916±131	1138±78	922±67	1043±118	1080 ± 42
1450	–	1041±109	–	1033±173	1135±71	–
1500	1071± 136	1156 ± 37	1236 ± 145	1096± 109	1167 ± 98	1244 ± 56
1550	1045 ± 70	1167 ± 90	1073 ± 121	1161±71	1135±29	1160± 122
1600	1202 ± 17	1206 ± 98	1186 ± 20	1073± 73	1063± 104	1204 ± 97

4.2.4 Fracture mode

After bending test the fractured surfaces of materials were examined by SEM analysis. The differences in fracture modes between pure and silica-doped TZ, 0.05A-TZ and 0.25A-TZ ceramics (exemplified by materials sintered at 1450 °C) are shown in Figure 34.

The alumina–free TZ (a) and TZ/SiO_2 (d) materials predominantly fractured intergranularly. The low-alumina containing materials 0.05-TZ (b) and 0.05A-TZ/SiO_2 (e) exhibited a mixed fracture mode with clusters of inter- and transgranular failed grains evenly distributed on the fracture surface. 0.25A-TZ (c) and 0.25A-TZ/SiO_2 (f) materials predominantly fractured transgranularly. Thus, alumina additions change the fracture mode of tetragonal zirconia from intergranular to transgranular. In contrast to alumina, silica doping had no major influence on the observed fracture mode. As illustrated in Figure 34d-f, silica-doped TZ/SiO_2, and co-doped 0.05A-TZ/SiO_2 and 0.25A-TZ/SiO_2 materials exhibited predominantly intergranular, mixed and predominantly transgranular fracture modes, respectively.

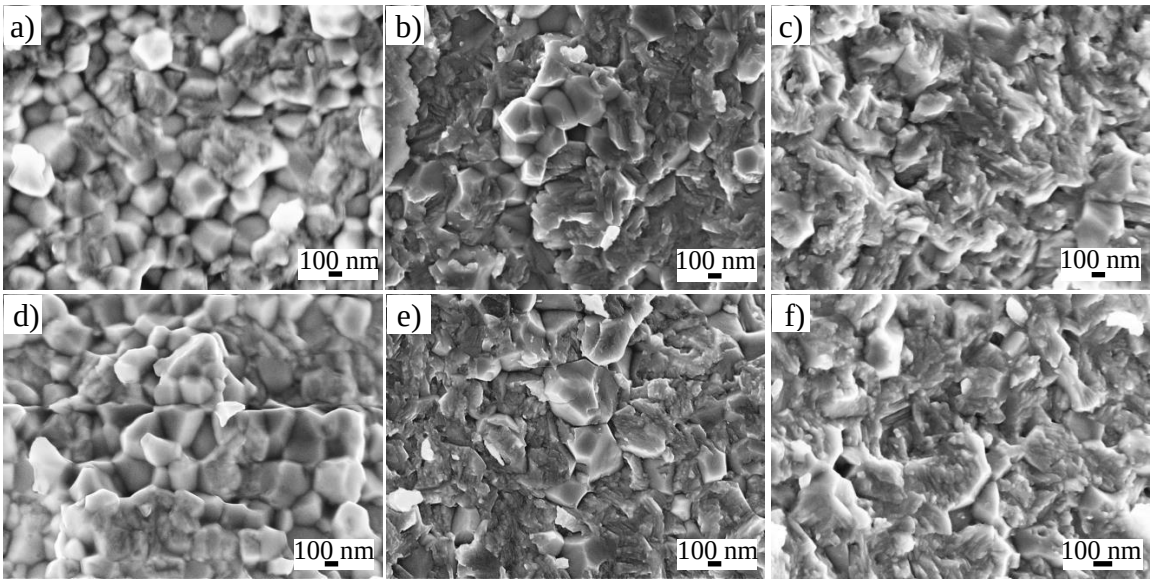


Figure 34: Fractured surfaces of as-sintered at 1450 °C (a) TZ, (b) 0.05A-TZ, (c) 0.25A-TZ and (d) TZ/SiO_2 (e) 0.05A-TZ/SiO_2 (f) 0.25A-TZ/SiO_2 materials after a bending test.

The same pure and silica-doped TZ, 0.05A-TZ and 0.25A-TZ materials sintered at 1450 °C were polished, thermally etched and indented with a series of 100 N loads. The SEM micrographs of indentation crack paths for all materials are shown in Figure 35. The results were in agreement with the studies of fracture modes of the same materials. In the case of alumina-free TZ and TZ/SiO_2 materials cracks propagate intergranularly, implying that silica does not have any effect on the crack propagation in tetragonal zirconia. In turn, the presence of 0.05 and 0.25 wt% of alumina lead to the mixed and transgranular crack propagation respectively.

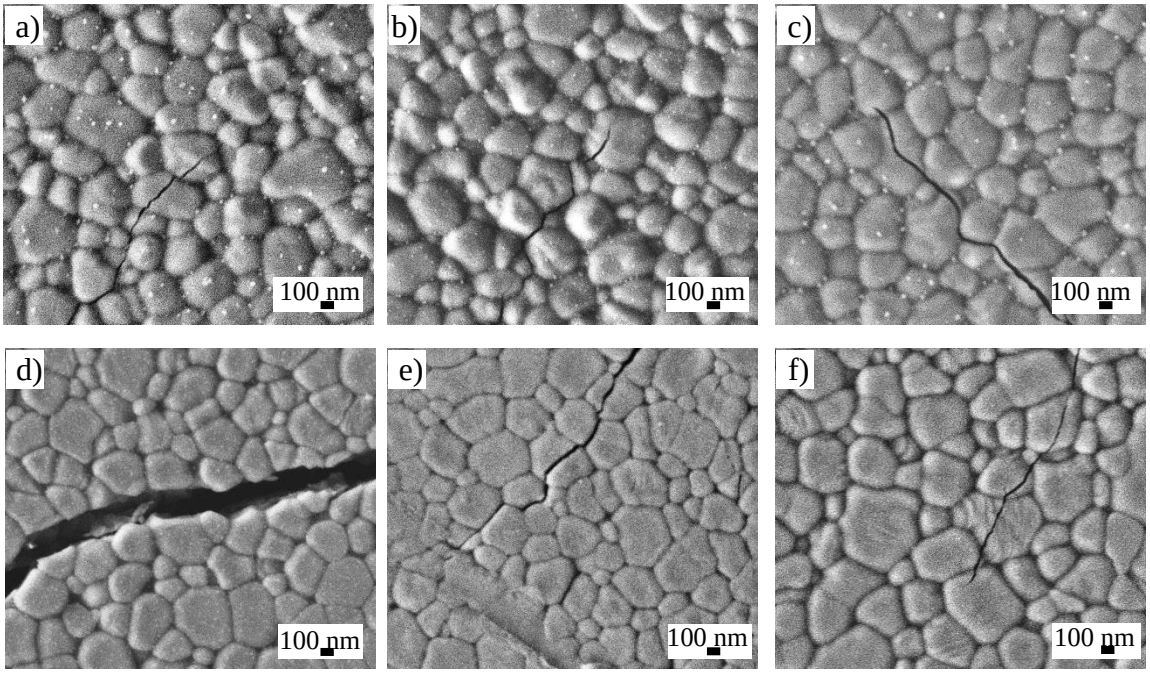


Figure 35: SEM micrographs of indentations into a sintered at 1450 °C (a) TZ (b) 0.05A-TZ (c) 0.25A-TZ (d) TZ/SiO_2 (e) 0.05A-TZ/SiO_2 and (f) 0.25A-TZ/SiO_2 materials.

In order to estimate the possible effect of sintering temperatures on the fracture modes of materials the silica-doped TZ, 0.05A-TZ and 0.25A-TZ ceramics sintered at 1400 °C and at 1600 °C for 2 h were fractured and examined by SEM. Similary to results obtained

for materials sintered at 1450 °C the alumina-free ceramics revealed essentaly intergranular fracture mode (Figure 36a,d), while 0.05% and 0.25% alumina-containing materials revealed mixed (Figure 36b,c) and transgranular fracture modes respectivly (Figure 36e,d)

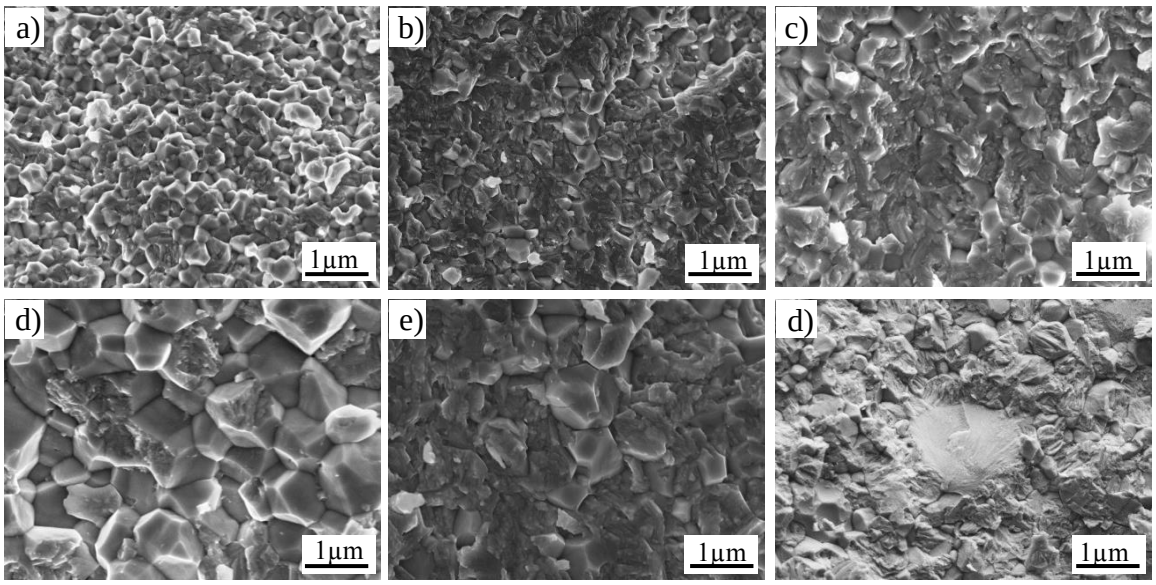


Figure 36: Fractured surfaces of as-sintered at 1400 °C for 2 h (a) TZ/SiO_2, (b) 0.05A-TZ/SiO_2, (c) 0.25A-TZ/SiO_2 and as-sintered at 1600 °C (d) TZ/SiO_2 (e) 0.05A-TZ/SiO_2 (f) 0.25A-TZ/SiO_2 materials.

4.2.5 Investigating grain boundaries in 0.25A-TZ and 0.25A-TZ/SiO_2 using impedance spectroscopy

It was reported that the activation enthalpy for LTD of 3Y-TZP (~ 83 kJ/mol) is comparable to that for the ionic conductivity, which arises from the mobility of oxygen ions, moving in the lattice via a vacancy mechanism. Since the rate of LTD and the conductivity are both goverened by the presence of oxygen vacancies, the effect of alumina-silica-co-doping on the grain boundary conductivity of 3Y-TZP was studied by impedance spectroscopy.

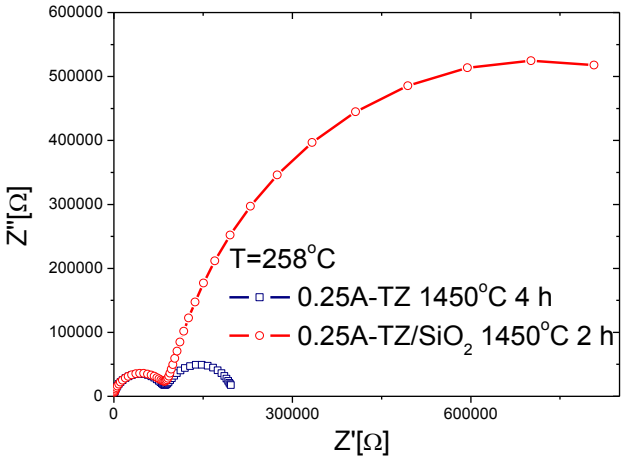


Figure 37: Impedance spectra obtained at 258 °C for 0.25A-TZ and 0.25A-TZ/SiO_2 materials.

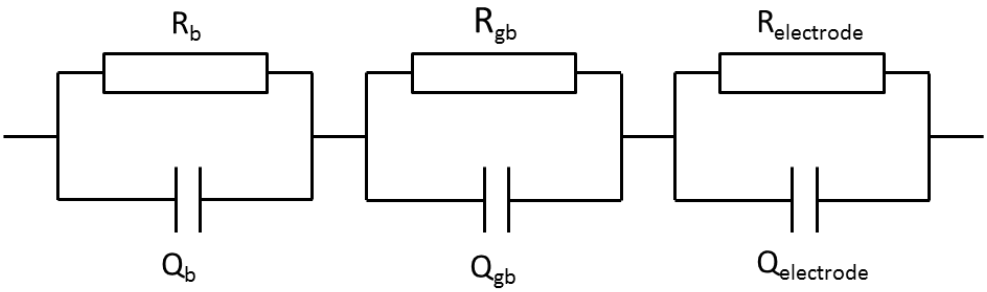


Figure 38: Equivalent circuit used for fitting of experimental data.

0.25A-TZ and 0.25A-TZ/SiO_2 sintered at 1450 °C for 4 and 2 h, having the same grain sizes, were prepared and their impedance spectra were obtained in temperature range of ~120-440 °C. Figure 37 shows typical impedance spectra of investigated 0.25A-TZ and 0.25A-TZ/SiO_2 materials, exemplified by spectra obtained at 258 °C. Two parts of semicircles may be distinguished. It is generally accepted [113] that the high-frequency part of the spectrum is related to the specific electrical conductivity of zirconia grains and the low-frequency semicircle describes electrical conductivity of grain boundaries, resulting from the blocking effect of charge carriers due to internal interfaces of the material such as grain boundaries, insulating inclusions of impurities and other microstructural defects like pores. The equivalent circuit used for the fitting of the experimental data is presented in Figure 38.

The grain boundary resistivity was thus observed to change significantly by co-doping. Figure 41 gives the Arrhenius plots of the grain boundary and the bulk resistivities, measured for 0.25A-TZ and 0.25A-TZ/SiO_2. The activation energies for the grain boundary resistivity of both samples are slightly higher than that for the bulk resistivity.

The activation energy is quite insensitive to presence of dopants: the activation energy for the grain boundary resistivity for 0.25A-TZ and co-doped 0.25A-TZ/SiO_2 samples were 1.08 eV and 1.06 eV respectively (Figure 41). Therefore, it can be assumed that the co-doping did not cause additional lattice defects (i.e. oxygen vacancies) in the ZrO_2 lattice but rather altered the grain boundary phase making it more resistant to charge transport resulting in lower conductivity.

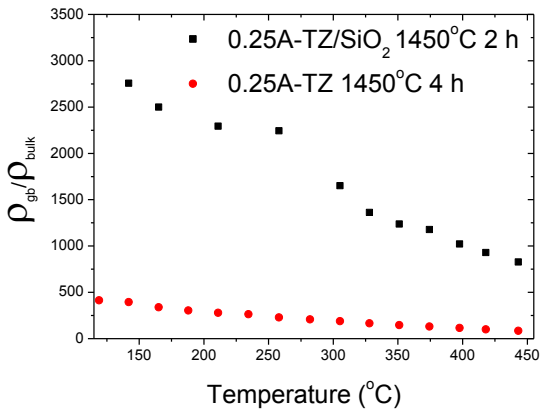


Figure 39: Ratio of grain boundary resistivity to bulk resistivity as a function of temperature.

Table 11: Bulk and grain boundary resistivity ($\Omega \cdot cm^{-1}$) obtained at 119-443 °C for 0.25A-TZ and 0.25A-TZ/SiO_2 materials sintered at 1450 °C for 4 and 2 h respectively.

Temperature (°C)	Bulk resistivity 0.25A-TZ	GB resistivity 0.25A-TZ	Bulk resistivity 0.25A-TZ/SiO_2	GB resistivity 0.25A-TZ/SiO_2
443	3706	313566	3941	3,25802E6
418	5915	593438	6559	6,10148E6
398	9798	1,12624E6	10186	1,04044E7
374	16987	2,20841E6	17483	2,0572E7
351	30614	4,49057E6	31498	3,89872E7
328	57595	9,53905E6	56291	7,664E7
305	113714	2,15013E7	112105	1,84968E8
282	244581	5,07559E7	-	-
258	566193	1,29891E8	522556	1,17226E9
235	1,36872E6	3,61703E8	-	-
211	3,57271E6	9,97822E8	3,81765E6	8,75898E9
188	1,06621E7	3,24544E9	-	-
166	3,48701E7	1,18394E10	3,6056E7	9,01268E10
142	1,32826E8	5,24202E10	1,32075E8	3,64202E11
119	5,64666E8	2,33791E11	-	-

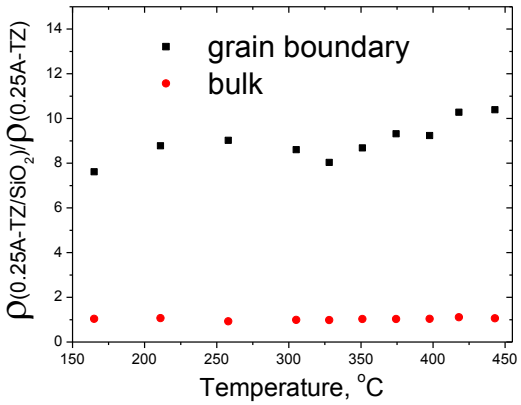


Figure 40: Temperature dependence of the resistivity ratio of 0.25A-TZ/SiO_2 to 0.25A-TZ. Silica addition to 0.25A-TZ material sintered at 1450 °C for 2 h does not influence on the bulk resistivity, while it drastically increases the grain boundary resistivity by about 10 times.

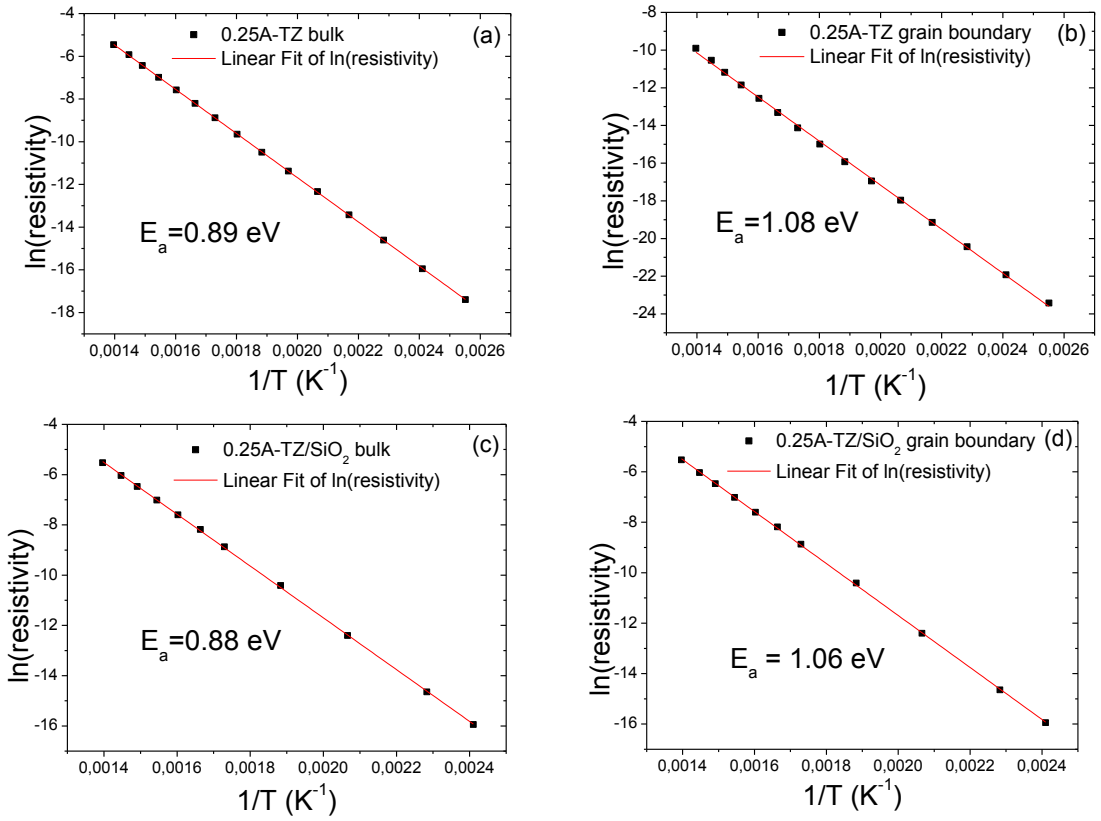


Figure 41: Arrhenius plots of grain boundary and bulk resistivity: (a) 0.25A-TZ activation energy for the bulk resistivity E_a^{bulk}= 0.89 eV, (b) 0.25A-TZ activation energy for the grain boundary resistivity $E_a^{GB} = 1.08\ eV$, (c) 0.25A-TZ/SiO_2 E_a^{bulk}= 0.88 eV, (d) 0.25A-TZ/SiO_2 $E_a^{GB} = 1.06\ eV$.

4.2.6 Optical properties

To study the effect of silica on the transmittance of 3Y-TZP materials 1.5 mm thick 0.05A-TZ and 0.05A-TZ/SiO_2 disks sintered at 1450 °C for 2 h were prepared and mirror polished from the both sides. Transmission measurements were made in the wavelength range of 300 nm to 800 nm using the Perkin-Elmer instrument (Figure 42). The results show that in case of 0.05A-TZ material the addition of silica reduces the transmittance by ~ 10%.

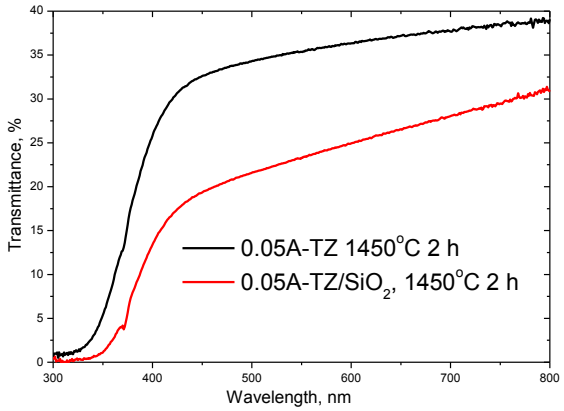


Figure 42: Transmittance of 1.5 mm thick 0.05A-TZ and 0.05A-TZ/SiO_2 materials sintered at 1450 °C for 2 h.

4.3 *In vitro* Ageing Behaviour

4.3.1 XRD of aged 3Y-TZP

Characterised in terms of microstructure, phase composition and mechanical properties the as-sintered samples were further exposed to accelerated *in vitro* ageing tests in distilled water under isothermal conditions at 134 °C.

The typical XRD profiles of aged samples (exemplified by 0.25A-TZ/SiO_2 material sintered at 1600 °C for 2 h and aged for 6-230 h) are shown in Figure 43. After 6 h of ageing, the monoclinic $(\bar{1}\ 1\ 1)_m$, $(1\ 1\ 1)_m$, and $(0\ 0\ 2)_m$ peaks positioned at 2θ of 28.15°, 31.3°, and 34°, respectively, start emerging, with a tendency for their intensity to increase with longer ageing times at the expense of reduced intensity of the tetragonal $(1\ 0\ 1)_t$, $(0\ 0\ 2)_t$ and $(1\ 1\ 0)_t$ peaks. The phase transformation progressed with time for all the examined specimens.

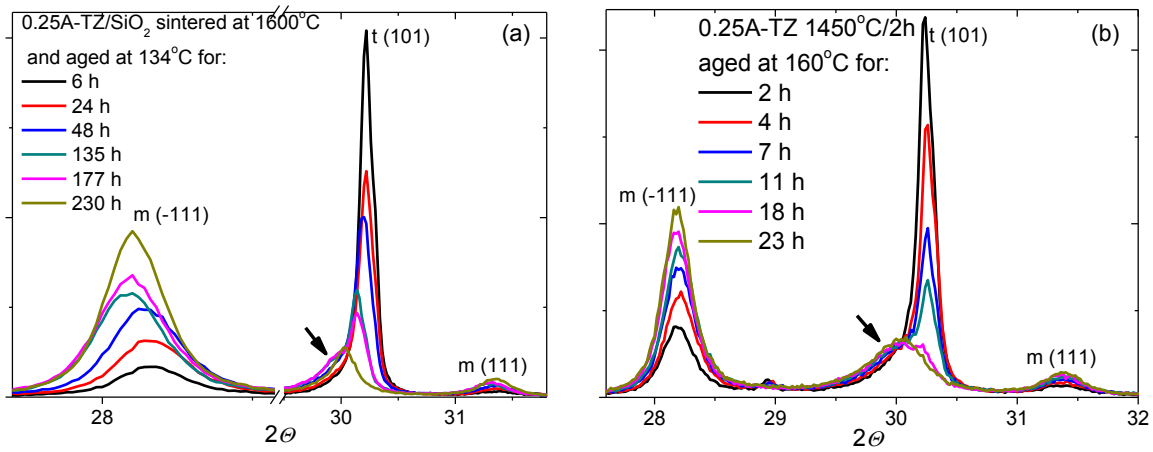


Figure 43: XRD patterns obtained from (a) 0.25A-TZ/SiO_2 ceramic surfaces, sintered for 2 h at 1600 °C and aged in water at 134 °C for 6, 24, 48, 135, 177 and 230 h; (b) 0.05A-TZ ceramic surfaces, sintered for 2 h at 1450 °C and aged in water at 160 °C for 2, 4, 7, 11, 18 and 23 h. Arrows point the broadening of $(1\ 01)_t/(1\ 1\ 1)_c$ peak.

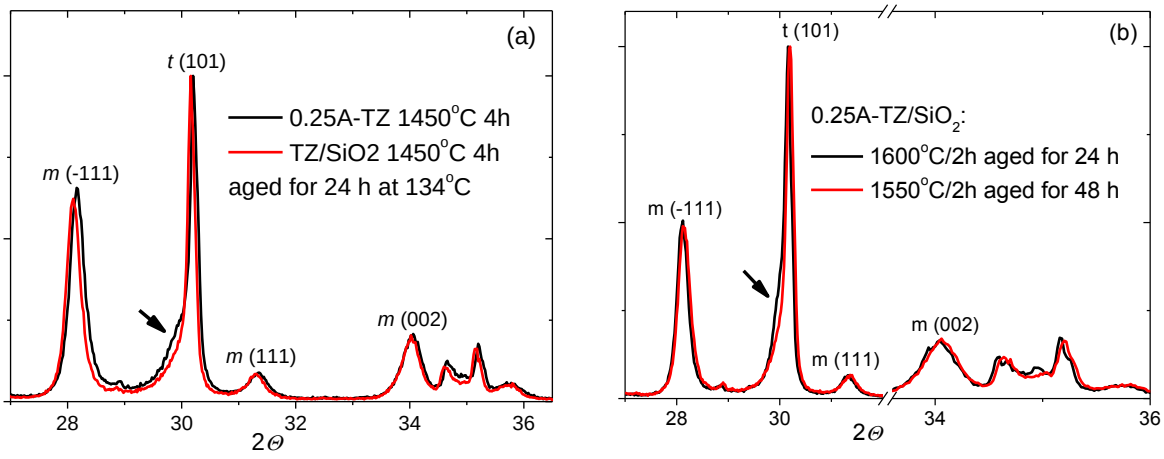


Figure 44: XRD patterns obtained from (a) 0.25A-TZ and TZ/SiO_2 ceramic surfaces, sintered for 2 h at 1450 °C and aged in water at 134 °C for 24 h; (b) 0.25A- TZ/SiO_2 ceramic surfaces, sintered for 2 h at 1600 °C and 1550 °C and aged in water at 134 °C for 24 h and 48 h respectively.

Besides, with increasing intensity of transformed monoclinic peaks (after prolonged ageing) the low-2-theta asymmetry of remaining $(1\ 01)_t/(1\ 1\ 1)_c$ peak starts to appear. This feature was systematically observed for all materials sintered and aged at different temperatures. The extent of asymmetry depends on dopant and sintering temperatures. Thus, the XRD pattern of alumina-doped material revealed higher asymmetry of $(1\ 01)_t/(1\ 1\ 1)_c$ peak compared to silica-doped material, as shown in Figure 44a for specimens with the same intensity of monoclinic peaks after 24 h ageing. The extent of broadening was also higher for 0.25A-TZ/SiO_2 material sintered at 1600 °C compared to the same material sintered at 1550 °C and having the same amount of monoclinic phase (Figure 44).

4.3.2 The effect of alumina or/and silica co-doping on the LTD of tetragonal zirconia

In order to differentiate between the distinct contributions of two dopants to the overall resistance to LTD all materials sintered at 1450 °C for 4 h and having practically similar grains sizes were exposed to hydrothermal ageing at 134 °C for 6-48 h and characterised by XRD analysis.

The time-dependent variation of the calculated fraction of the monoclinic zirconia phase for the silica-free and silica-doped TZ, 0.05A-TZ and 0.25A-TZ materials sintered at 1450 °C during *in vitro* ageing is presented in Figure 45. The rate of *t-m* transformation substantially decreases when either alumina or silica is present in the TZ. The rate of monoclinic phase nucleation and growth was further decreased, when both silica and alumina were present in the TZ.

After 24 hours of accelerated ageing, the same amount of transformed monoclinic fraction (about 50%) was measured on the surface of 0.25A-TZ and TZ/SiO_2 specimens, and only about half of this value was measured on the surface of 0.25A-TZ/SiO_2 and 0.05A-TZ/SiO_2.

Somewhat larger differences were observed after 48 hours of ageing. However, due to a noticeable difference in the asymmetry of the $(1\ 01)_t/(1\ 1\ 1)_c$ peak the accuracy of calculated monoclinic fractions in silica-free and silica-doped TZ might not be equivalent. Due to the low X-ray penetration in zirconia (typically limited to several microns in depth) the XRD analysis is unable to provide any information when the *t-m*

transformation propagates into the bulk, i.e. after 24-48 h of ageing depending on the stability of the sample. At the same time the transformed monoclinic layer on the cross-sections of the aged samples is clearly visible by optical microscope. Therefore, the cuts of sintered at 1450 °C and aged for 72-120 h pure and silica-doped TZ, 0.05A-TZ and 0.25A-TZ/SiO_2 samples were prepared, polished and the thickness transformed monoclinic layer depth was measured using an optical microscope. In optical micrographs a zone of grey colour was clearly visible, extending from the surface to some depth into the bulk material (Figure 46). With longer ageing time, this transformed zone expands deeper into the interior of the sample.

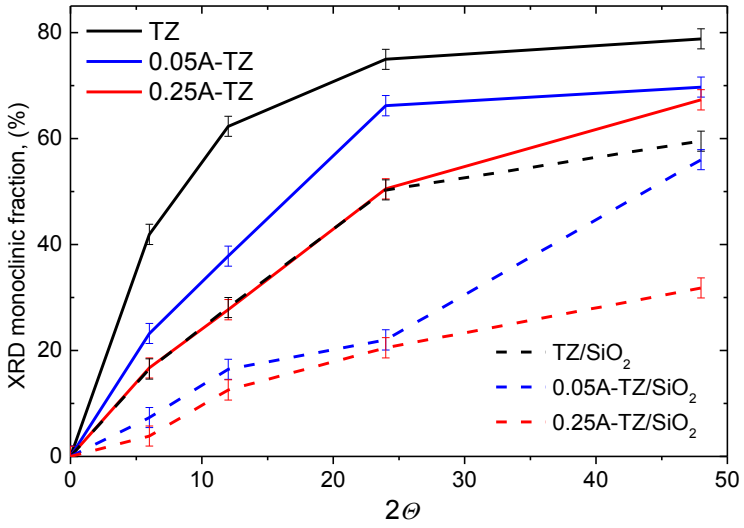


Figure 45: Calculated monoclinic fraction versus in vitro ageing time for pure and silica-doped TZ, 0.05A-TZ and 0.25A-TZ materials sintered at 1450 °C for 4 h.

The interface between unaffected and transformed material shows a distinct border, enabling the thickness of the transformed layer to be determined. The ageing curves obtained by optical observations of the transformed layer are shown in Figure 48. From these observations, one can conclude that the thickness of the transformed layer increases linearly with time. These observations hold for all investigated materials regardless whether they were co-doped or not. The cross-sections of pure and silica-doped TZ, 0.05A-TZ and 0.25A-TZ samples sintered at 1600 °C for 2 h and aged for 24-72 h were prepared as well and studied by optical microscopy (Figure 47). Similarly to the results obtained for the samples sintered at 1450 °C the transformed layer increased continuously and linearly into the bulk of the material with increasing the ageing time (Figure 48b).

Slope coefficients for obtained ageing curves are presented in Table 12.

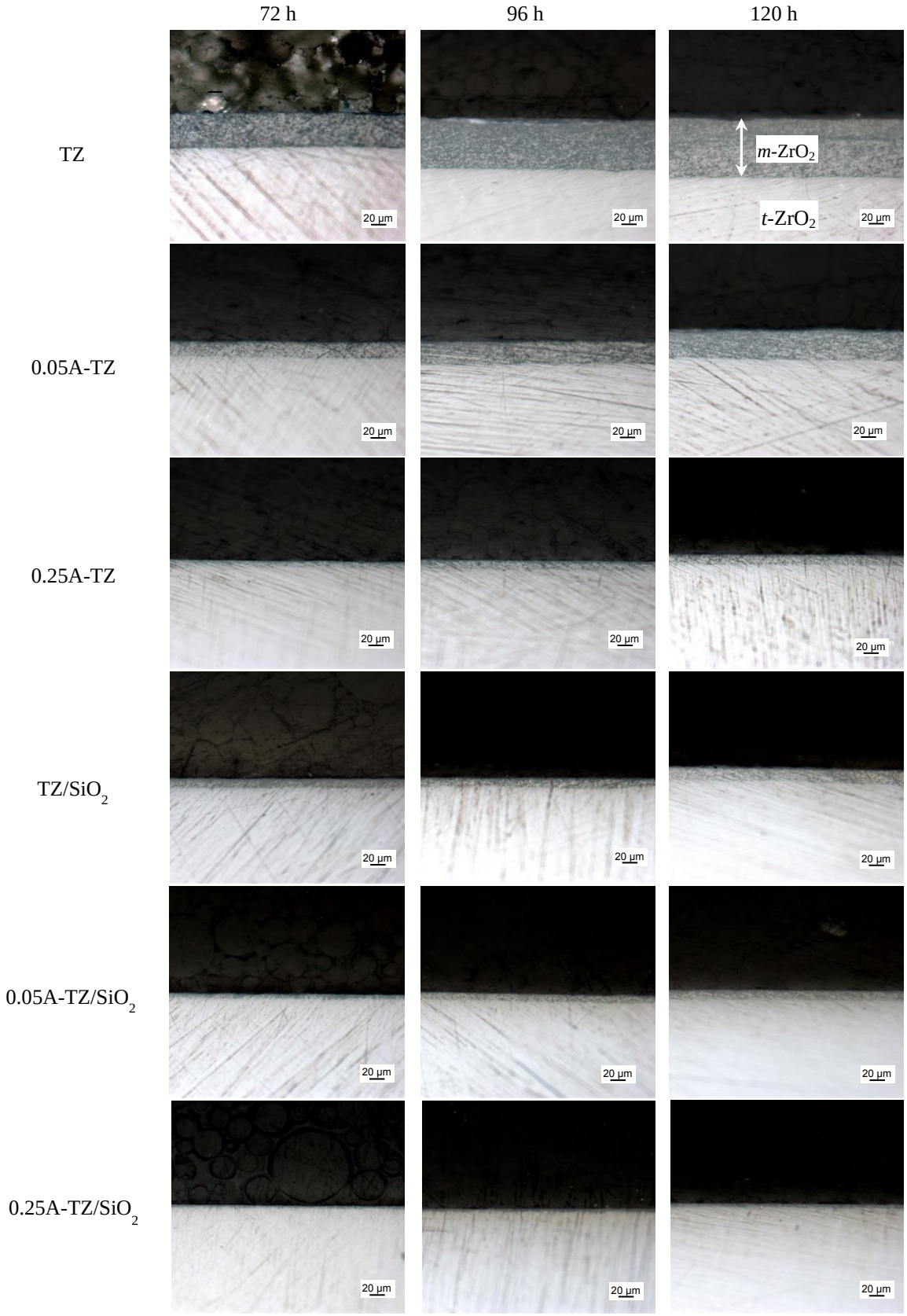


Figure 46: Optical micrographs of the cross-sections of pure and silica-doped TZ, 0.05A-TZ and 0.25A-TZ samples sintered at 1450 °C for 4 h and aged for 72-120 h. Time of ageing increases left-to-right along each material in a row.

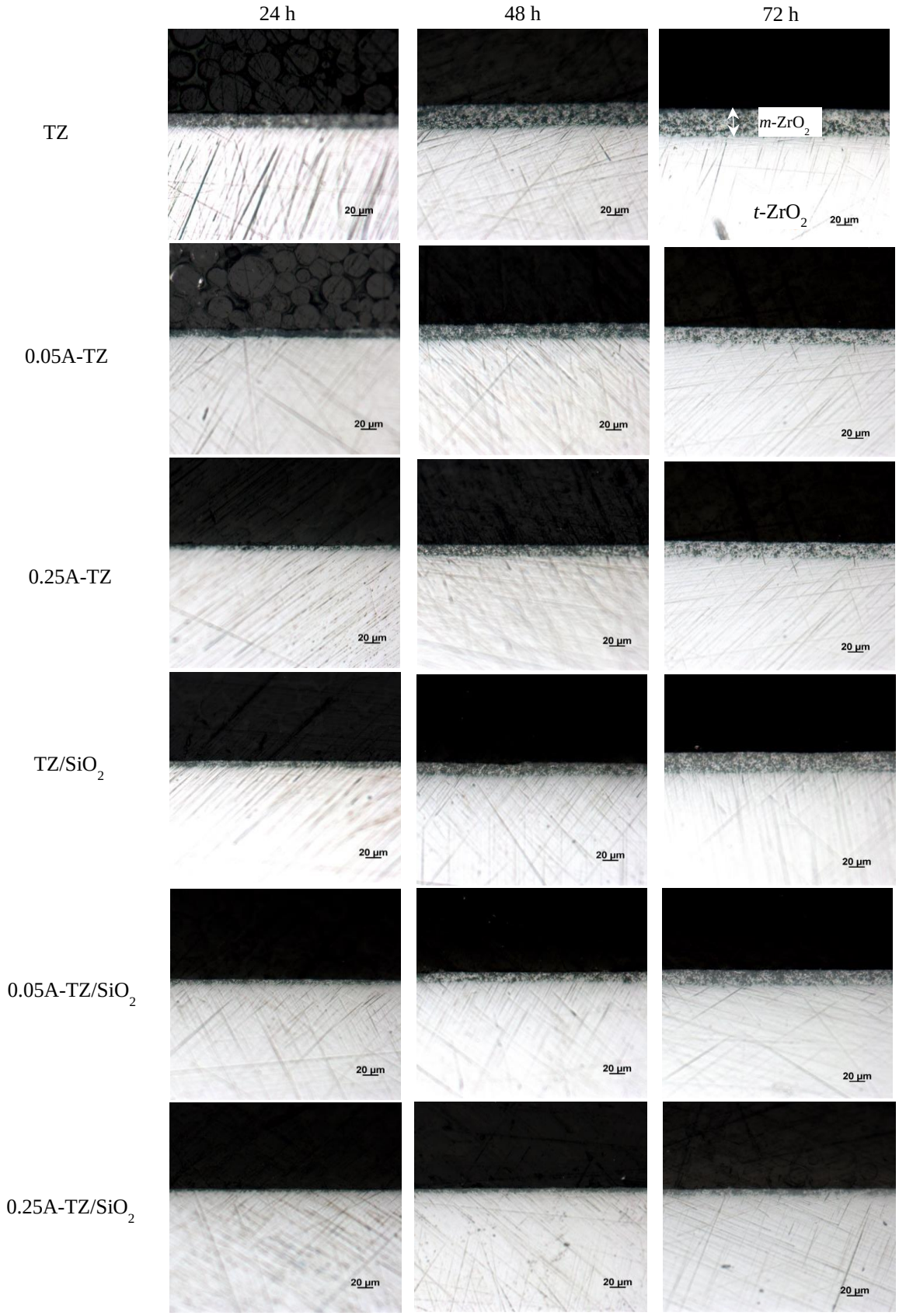


Figure 47: Optical micrographs of the cross-sections of pure and silica-doped TZ, 0.05A-TZ and 0.25A-TZ samples sintered at 1600 °C for 2 h and aged for 24-72 h. Time of ageing increases left-to-right along each material in a row.

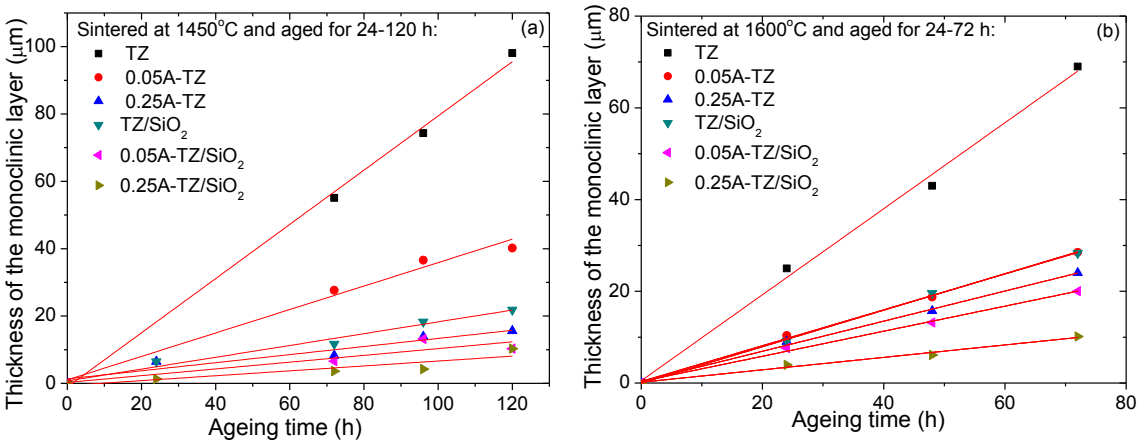


Figure 48: Thickness of the transformed layer versus *in vitro* ageing time measured from cross-sections of pure and silica-doped TZ, 0.05A-TZ and 0.25A-TZ materials sintered at: (a) 1450°C for 4 h, (b) 1600 °C for 2 h.

Table 12: Slope coefficients for ageing curves, obtained by observations of the thickness of the transformed layer on the cross-sections of aged materials using optical interferometry.

Sintering temperature	TZ	0.05A-TZ	0.25A-TZ	TZ/SiO_2	0.05A-TZ/SiO_2	0.25A-TZ/SiO_2
1450 °C	0.80	0.34	0.12	0.17	0.10	0.07
1600 °C	0.94	0.39	0.32	0.40	0.27	0.13

4.3.3 FIB-SEM analysis of transformed zone

The examination of sub-surface region of hydrothermally aged 3Y-TZP by optical microscope does not show detailed microstructures of transformed zone and interface between monoclinic layer and unaffected material. Therefore, the FIB technique was used to prepare artifact-free cuts of pure and silica-doped TZ and 0.25A-TZ materials sintered at 1450 °C for 4 h and aged for 24 h at 134 °C. The materials were subsequently investigated by SEM. The FIB-SEM study clearly revealed the formation of a zone of differing appearance (Figure 49). Within this zone, most of the grains exhibit a microstructure within the individual grain, which is interpreted to reflect the typical twinning caused by the martensitic transformation to the monoclinic structure. The interface between unaffected and transformed material shows a distinct border without any gradual decrease; therefore the thickness of the transformed layer could be determined. The largest thickness was found with the undoped TZ material (Figure 49a), extending into the bulk beyond the lower end of the cross-section, which also exhibited a significant extent of intragranular microcracking, running nearly parallel to the surface (Figure 50a). The latter are associated with the large shear and tensile strains at the grain boundaries produced by twinning during *t–m* transformation. The transformed layers in alumina- or silica-doped 3Y-TZP disks were thinner (Figure 49b,c) and showed substantially reduced amounts of grain-boundary microcracking, compared to the TZ material (Figure 50b,c) aged under the same conditions. The thickness of the transformed layer was practically the same for the 0.25A-TZ and TZ/SiO_2 (~6,5 μm). This result is in agreement with the almost overlapping ageing curves for these materials (Figure 45). SEM micrograph of the 0.25A-TZ/SiO_2 material aged for 24 h shows an almost crack-free sub-surface microstructure with the thickness of transformed layer less than 2 μm, where only few first surface layers of grains were transformed (Figure 49d and Figure

50d). In agreement with TEM observations (Figure 28), the silica-free materials have faceted grains (Figure 50a,b), while silica-doped 3Y-TZP possess rounded grains (Figure 50c-d).

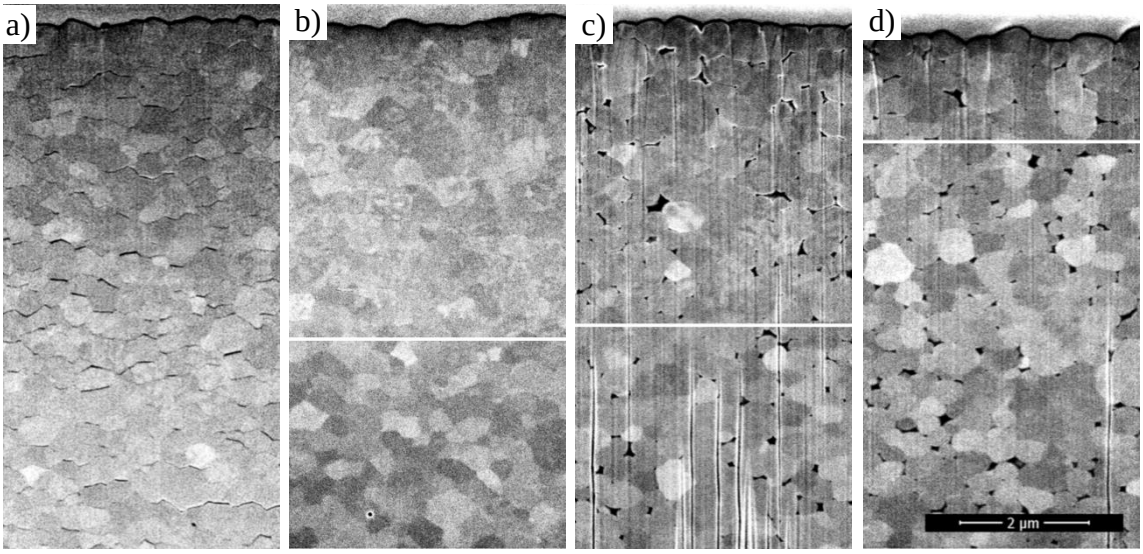


Figure 49: FIB-SEM cross-sections of the 24-hours aged (a) TZ, (b) 0.25A-TZ, (c) TZ/SiO_2 and (d) $0.25A\text{-}TZ/SiO_2$ specimens. White line indicates a rough estimate of the *t-m* transformed layer border (In Fig. 49a the layer was extending into the bulk beyond the lower end of the cross-section).

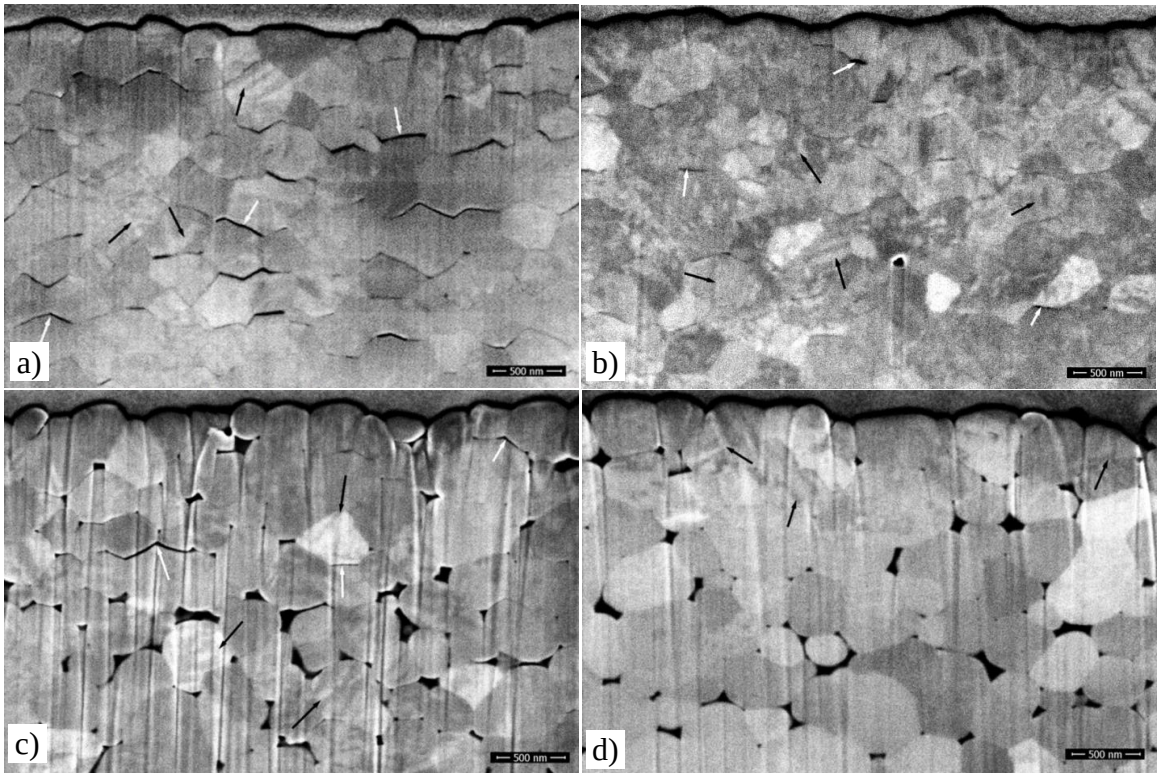


Figure 50: A higher-magnification FIB-SEM cross-sections of the 24-hours aged (a) TZ, (b) 0.25A-TZ, (c) TZ/SiO_2 and (d) $0.25A\text{-}TZ/SiO_2$ specimens. White arrows point to grain boundary microcracks, while black arrows indicate the martensitic monoclinic variants.

4.3.4 Sintering temperature-related ageing properties

In order to study the effect of sintering temperature on the ageing properties of alumina or/and silica-doped 3Y-TZP, pure and silica-doped TZ and 0.25A-TZ materials sintered at 1400-1600 °C for 2 h were exposed to *in vitro* ageing at 134 °C for 24 h (Figure 51). TZ material sintered at 1400 °C for 2 h revealed higher hydrothermal stability compared to single-doped materials, however the same material sintered at 1450-1600 °C for 2 h was already saturated with monoclinic phase after 24 h of ageing. Similarly to the results obtained for materials sintered at 1450 °C for 4 h, alumina or silica single-doped materials possess better ageing properties compared to TZ, containing the same amount of monoclinic phase. However, while alumina-doped material keeps better ageing properties even when sintered at higher temperatures, the addition of silica only slightly improves the hydrothermal stability of tetragonal zirconia sintered at temperatures ≥ 1500 °C. The co-doped 0.25A-TZ/SiO_2 material keeps the best hydrothermal stability, even when it was sintered at high temperatures.

In 3Y-TZP sintered at temperature range between 1400 °C and 1600 °C two phases, *t+c*, are present. The rate of phase partitioning depends on the type of dopant [114]. Thus, different amounts of tetragonal phase can be available for the transformation in studied materials. To verify the accuracy of the results obtained in the ageing experiment, the amount of untransformable phase was calculated from XRD patterns of overaged until the saturation pure and silica-doped TZ and 0.25A-TZ materials sintered at 1600 °C (Table 13). Pure and single-doped materials were fully or almost saturated with the monoclinic phase after ~ 24 h of ageing, while ageing at extreme conditions (200 °C, ~ 200 h) was needed to obtain the saturation with the monoclinic phase in the surface of 0.25A-TZ/SiO_2 ceramic (Figure 52). Substantial differences were observed in the shape of the untransformable zirconia peak between pure and silica-doped materials. The broad peak is characteristic for TZ and 0.25A-TZ materials, while narrow, but with higher intensity peak was observed in the case of TZ/SiO_2 and 0.25A-TZ/SiO_2 ceramics (Figure 53).

The amount of untransformable phase increased in the following order 0.25A-TZ/SiO_2 < TZ ≤ TZ/SiO_2 < 0.25A-TZ (Table 13). The values for the amounts of monoclinic phase after 24 h of ageing were normalised, taking into acount the amount of tetragonal phase, available for the *t-m* transformation (Table 11). Results revealed that in pure TZ and single-doped TZ/SiO_2 and 0.25A-TZ materials almost all tetragonal phase was transformed into the monoclinic, while in co-doped 0.25A-TZ/SiO_2 material only half of available for the transformation phase became the monoclinic.

Table 13: The values of untransformable phase, unnormalised and normalised monoclinic phase after 24 h of ageing at 134°C for pure and silica-doped TZ and 0.25A-TZ/SiO_2 materials sintered at 1600 °C for 2 h.

	Untransformable phase (%)	Monoclinic phase (24 h of ageing)	Normalised monoclinic (%)
TZ	26.3	72.9	98.9
0.25A-TZ	32.6	63.2	93.8
TZ/SiO_2	26.6	72.3	98.5
0.25A-TZ/SiO_2	21.4	39.6	50.4

Moreover, the 0.25A-TZ/SiO_2 sintered at 1500-1600 °C maintained its integrity, even after ageing under extreme conditions (~200 h at 200 °C), while the TZ, TZ/SiO_2 and 0.25A-TZ disintegrated after ageing at 134°C for 3-4 days. Thus, the co-doping of the 3Y-TZP bioceramics with alumina and silica ensures a greater resistance to ageing, as

compared to the single-doped alumina 3Y-TZP, not only when sintered at moderate temperatures, but also when higher temperatures are employed.

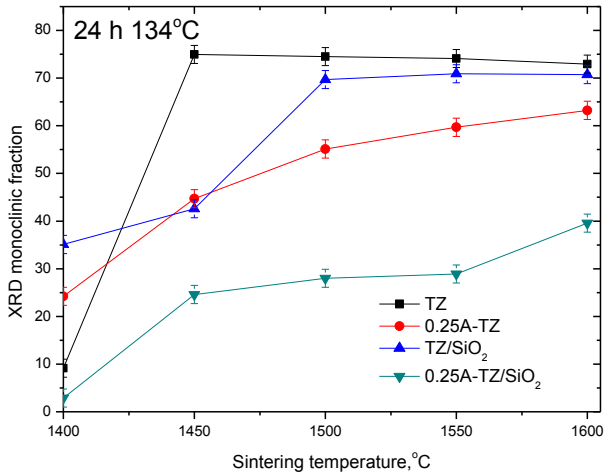


Figure 51: Calculated monoclinic fraction for pure and silica-doped TZ and 0.25A-TZ materials sintered at 1400-1600 °C for 2 h and *in vitro* aged for 24 h.

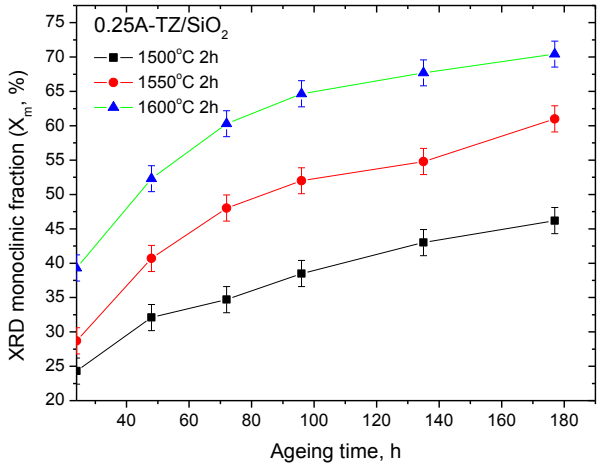


Figure 52: Calculated monoclinic fraction versus *in vitro* ageing at 134 °C for 0.25A-TZ/SiO_2 materials sintered at 1500-1600 °C for 2 h.

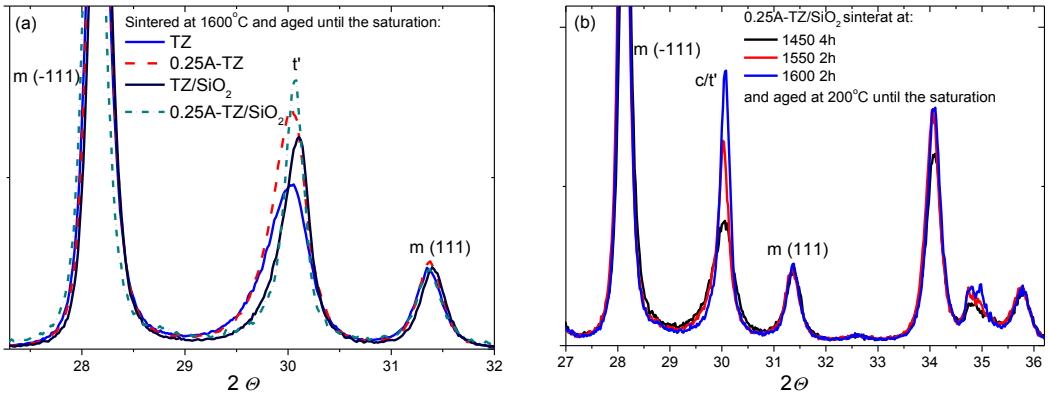


Figure 53: XRD patterns obtained from the surfaces of (a) pure and silica-doped TZ and 0.25A-TZ materials sintered at 1600 °C and aged until the saturation, (b) 0.25A-TZ/SiO_2 materials sintered at 1450-1600 °C and aged until the saturation.

4.3.5 Mechanical properties of the aged materials

The values of flexural strengths of sintered at 1450^{o}C and aged for 24 h materials, exemplified by pure and silica-doped TZ, 0.05A-TZ and 0.25A-TZ materials, are shown in Table 14. The results were nearly identical to those before ageing (i.e. those listed in Table 10), indicating that under these ageing conditions neither significant strengthening (due to transformed surface layer) nor substantial strength degradation (due to microcracking and/or lamination) has occurred. These observations hold for all investigated materials regardless whether they were co-doped or not.

Table 14**:** Flexural strength of the pure and silica-doped TZ, 0.05A-TZ and 0.25A-TZ materials (mean ± SD) after 24 h of ageing.

Sample	Flexural strength, MPa
TZ	1077 ± 100
TZ-3Y/SiO_2	1021 ± 62
0.05A-TZ	1033 ± 114
0.05A-TZ/SiO_2	1171 ± 76
0.25A-TZ	1216 ± 70
0.25A-TZ/SiO_2	1212 ± 76

In order to qualitatively estimate the effect of hydrothermal degradation on the surface mechanical properties of alumina or/and silica doped 3Y-TZP, samples sintered at 1450 °C, were polished and aged up to 48 h and indented with a load of 100 N. The optical micrographs of a Vickers indentation into as-sintered, aged for 24 and 48 h materials are shown in Figure 54 and illustrate the dramatic difference in aged doped and co-doped material's response to Vickers' indentation. Extensive microcracking appears along the impression edges in alumina (0.25%) doped 3Y-TZP after being exposed to ageing for 24 h Figure 54d, ultimately leading to chipping of a large area around the indentation after 48 h of ageing; SiO_2-doped ceramic was even more susceptible to chipping of the damaged area around an impression that occurred after 24 h of ageing (Figure 54e); superior ageing resistance of co-doped material resulted in sharp, microcrack-free impression edges even after 48 h of ageing (Figure 54i). The latter also imply superior behaviour of co-doped zirconia under wear and cyclic loading conditions in an aqueous environment.

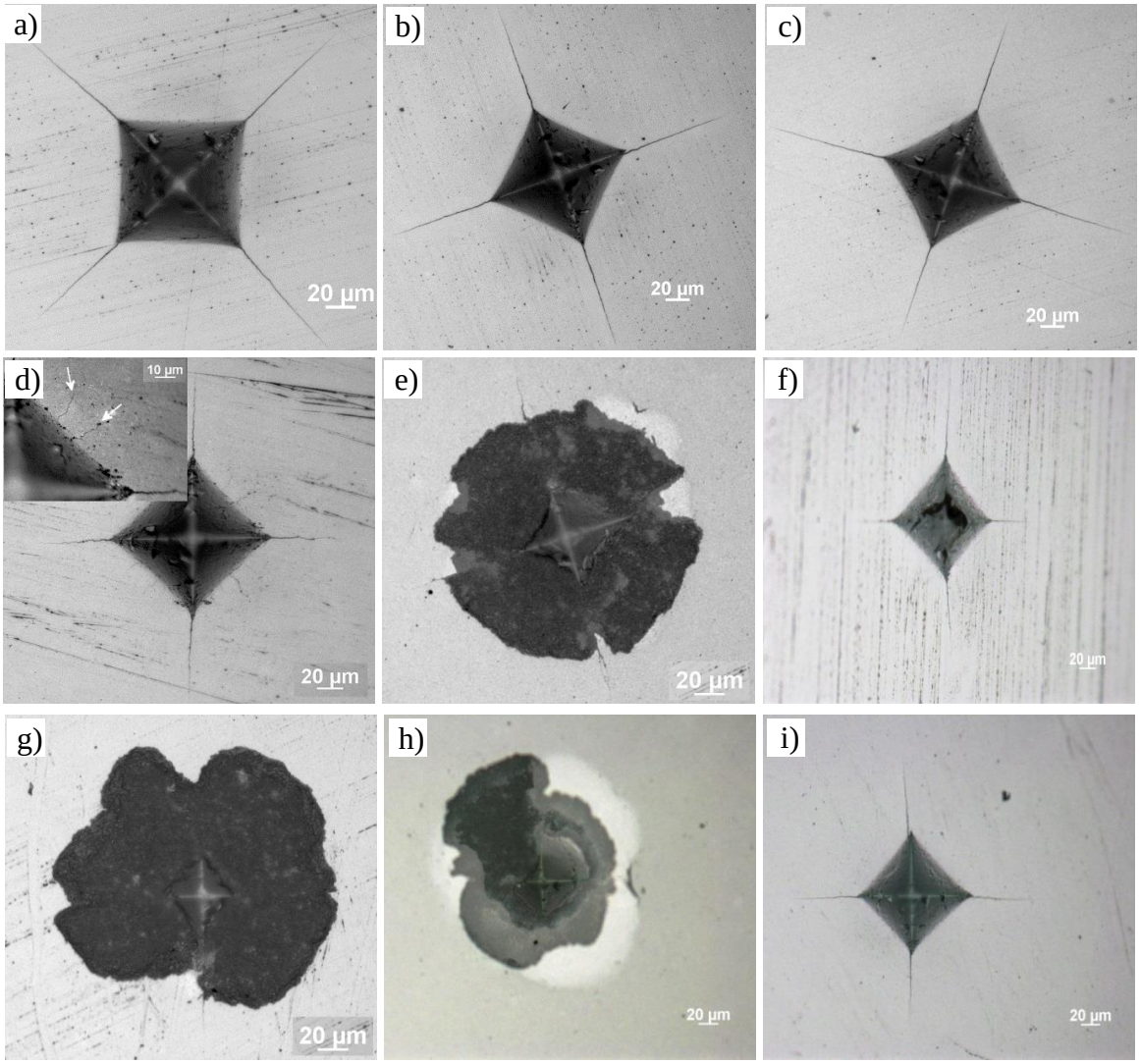


Figure 54: Optical micrographs of a Vickers indentations into a (a) 0.25A-TZ (b) TZ/SiO_2 (c) 0.25A-TZ/SiO_2 materials sintered at 1450 °C for 4 h (d) 0.25A-TZ (e) TZ/SiO_2 (f) 0.25A-TZ/SiO_2 materials sintered at 1450 °C for 4 h aged for 24 h (g) 0.25A-TZ and (h) TZ/SiO_2 (i) 0.25A-TZ/SiO_2 materials sintered at 1450 °C for 4 h aged for 48 h. White arrows point the cracks.

5 Discussion

5.1 The Infiltration Technique

In the first part of the thesis an alternative technique of adding silica into 3Y-TZP ceramics is presented. While alumina-containing 3Y-TZP powders are commertialy available, no silica-doped zirconia available in the market. Common way of preparation of silica-containing 3Y-TZP for research purposes is addition of colloidal silica to the zirconia slurry followed by drying and sintering. Since our method is based on the infiltration of pre-sintered zirconia performs with a silica sol solution, it can be easily adapted to the dry-processing of fixed dental prostheses.

Two ways of adding silica precursors were tested. The 3Y-TZP compacts were soaked either in pure dynasylan or in prehydrolyzed dynasylan solution. Pre-sintered discs were prepared from commercially available powders, which contained 0, 0.05 or 0.25 wt% of alumina. After soaking in prehydrolyzed dynasylan solution for 30 min, dried and finally sintered silica-doped and alumina/silica co-doped 3Y-TZP pellets contained from 0.15 to 0.25 wt% of amorphous silica phase, depending on the amount of porosity in pre-sintered discs. These additions to a large extent do not change the densities and mechanical properties of 3Y-TZP, but significantly decelerate the ageing. The soaking in pure dynasylan or in prehydrolyzed dynasylan solution for a longer period of time (~ 1 h) resulted in a higher content of silica, which is present in a form of zirconium silicate or cristobalite and substantially reduces the flexural strength of *t*-zirconia. Therefore, the soaking for 30 min in prehydrolyzed dynasylan solution is an optimized condition for preparing the silica-containing 3Y-TZP.

It should be noticed, however, that even small additions of silica reduce the translucency of 3Y-TZP ceramics. Thus, the translucency of 0.05A-TZ/SiO_2 material sintered at 1450 °C for 2 h was ~10% lower compared to this for 0.05A-TZ ceramic sintered at the same temperature. Therefore the silica-doped 3Y-TZP will work well for crowns and abutments mounted into metallic parts and implants, respectively.

5.2 Characterization of Sintered Ceramics

5.2.1 Microstructure and phase composition

Our results show that the presence of alumina does not introduce any noticeable change in the grain shape of 3Y-TZP (Figure 26), but it does slightly increase the grain size (Table 7). This could be attributed to the enhanced surface diffusion also responsible for the reported increase of sintering rate by alumina addition [115]. Since the solubility of alumina in Y-TZP is very limited, it tends to segregate along the grain boundaries. Our results of impedance measurements, i.e. substantially higher grain boundary resistivity in 0.25A-TZ and 0.25A-TZ/SiO_2 materials compared to the bulk resistivity of the same materials (Figure 39) support this. However, the excess of alumina, which could not be accommodated at the grain boundaries, tends to form individual alumina grains (α-Al_2O_3) in *t*-zirconia matrix. As it was mentioned in Chapter 1, due to a lower CTE the latter are known to have a negative role on the hydrothermal stability of *t*-zirconia [48]. Thus,

depending on the sintering temperature, influencing the grain size of 3Y-TZP, alumina can be either dissolved in *t*-zirconia or it will precipitate in the form of discrete α-Al_2O_3 grains. However, since the content of alumina in 0.05A-TZ and 0.25A-TZ materials is very low, the presence of α-Al_2O_3 phase is difficult to confirm. In fact, no individual alumina grains were observed in the SEM micrographs of 0.25A-TZ material, sintered at temperatures < 1500°C (Figure 26). The presence of such small amount of α-Al_2O_3 in this material could not be detected by XRD analysis, but this phase was detected as a fluorescence background on the Raman spectrum (Figure 31). To find out the temperature of the formation of α-Al_2O_3 phase the additional 0.25A-TZ specimens sintered at 1200-1350 °C were prepared and excited with a He-Ne laser together with samples sintered at higher temperatures. The obtained spectra are presented in Figure 55. Raman signals in the range of 100 and 750 cm^{-1} corresponding to the tetragonal zirconia were observed for all materials. Notice, that spectra for samples sintered at temperatures ≥ 1300 °C also contain fluorescence doublets in the 1370-1410 cm^{-1} range, corresponding to α-Al_2O_3.

These results suggest that in the case of 0.25A-TZ material the first α-Al_2O_3 precipitates appeared already at 1300 °C. It is known, that when heated to temperatures above 1200 °C, *θ*-Al_2O_3 undergoes a transformation, where the oxygen atoms rearrange into a hexagonal close packed structure to form thermodynamically stable α-Al_2O_3 [116]. On the other side, the appearance of α-Al_2O_3 peak at 1300°C can suggest that the amount of alumina in the region near the grain boundaries in 0.25A-TZ materials sintered above this temperature, i.e. at 1400-1600 °C, was already higher than the solubility limit.

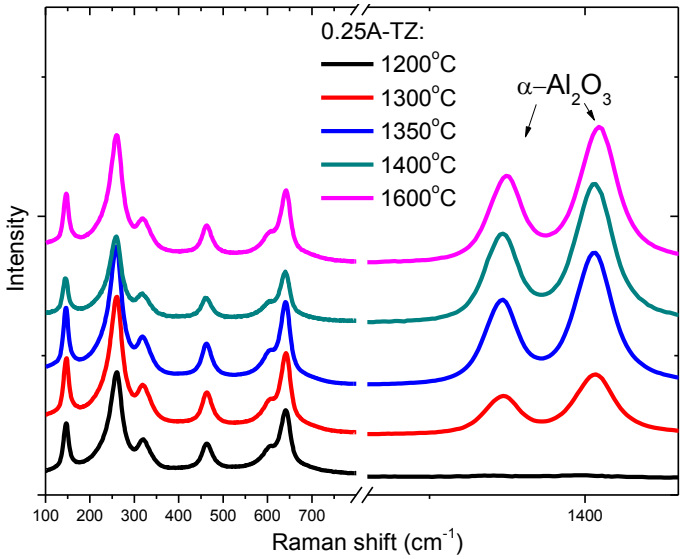


Figure 55: Raman spectra of 0.25A-TZ material sintered at 1200-1600°C for 2 h.

Considering the mean zirconia grain size for 0.25A-TZ material sintered at 1300 °C, which was measured to be a 0.2 μm – a very rough estimate of the limiting amount of alumina accommodated per unit area of zirconia grains can be made yielding a value 2×10^{-9} g/m^2. Anticipating this estimate, and assuming the homogeneous dopant distribution, the concentration of alumina per unit area of zirconia grains in 0.05A-TZ material was far below the saturation value; (for this the grains should have grown to 4 μm). In fact, no alumina fluorescence doublet characteristic for α-Al_2O_3 phase was observed for 0.05A-TZ even when the material was sintered at 1600 °C (Figure 33). Since the alumina fluorescence signals are usually too intensive, the absence of these signals suggests that in 0.05A-TZ material sintered at temperatures ≤ 1600 °C for 2 h the area of zirconia grains is large enough to accommodate the 0.05 wt% of alumina. Thus the increasing of sintering temperature (decreasing in the surface area of zirconia grains) will

result in a higher concentration of Al^{3+} at grain boundaries of 0.05A-TZ, but precipitation of alumina grains is highly unlikely.

In contrast to alumina, silica was preferentially located as an amorphous phase at the multiple grain junctions as evidenced by TEM micrographs in Figure 29. This amorphous phase contained some yttria and zirconia, but the exact composition, melting point and properties, e.g., temperature of glass transition T_g and CTE, have not been determined. Also demonstrated in Figure 29b-d is another important change in the microstructure with the silica addition, i.e., rounded zirconia grains also exhibiting largely reduced residual strains. This was demonstrated by Gremillard et al. [106], who thoroughly evaluated the lattice distortion in undoped and 0.5 wt.% silica containing 3Y-TZP. Two factors would appear to be contributing to this effect, i) the rounded grains as the radius of sharp edge determines the magnitude of the stresses associated with thermal expansion anisotropy on the tetragonal grains, and ii) even though this was not explicitly mentioned in their work, the strain developed at multiple grain junctions should be further reduced thanks to the presence of glassy phase with $T_g << T_{sintering}$. However, the stress absorbing effect of the glassy phase can neither be discerned from the overall reduction of internal strain, as determined from XRD peak broadening, nor can it be estimated, since the CTE and T_g values of this material are not known.

The co-doped ceramics sintered at temperatures < 1500^{o}C combined rounded grains with a glassy phase at multiple grain junctions characteristic for the silica-doped material, and higher concentration of alumina at grain boundaries compared to alumina single-doped 0.25A-TZ ceramic.

The microstructure of 0.25A-TZ/SiO_2 material substantially changes with the increase of sintering temperature.

In 0.25A-TZ/SiO_2 material sintered at 1550-1600 °C the amorphous phase was found not only at triple grain junctions, but also along the grain boundaries. The temperature-related (≥1550 °C) penetration of the silica phase from the grain junctions into the grain boundaries was accompanied by the emergence of a fraction of larger grains. The bimodal microstructures in the 3Y-TZP have already been observed [69], [73], [117], [118]. High sintering temperatures (>1550 °C) and longer dwell times (5-8 hours) were usually needed for them to evolve, but there was no indication of the possible role of the powder purity and/or the dopant level during the formation of the large grains. Here we demonstrate that in 3Y-TZP ceramics the bi-modal microstructure is likely to be formed, provided that small amounts of alumina and silica are simultaneously present and the material is sintered at temperatures ≥1550 °C. Since 3Y-TZP ceramics are sintered in a bi-phasic, *t*+*c* region, the larger grains are usually thought to be un-transformable (yttria-rich) *c*-ZrO_2 co-existing in equilibrium with the yttria-lean *t*-ZrO_2. Our additional EDS analyses performed on the 0.25A-TZ/SiO_2 material sintered at 1600 °C revealed that the larger grains indeed contained a higher yttria content (5–6 mol.%), while a considerably lower yttria content (2.2–2.7 mol.%) was found in the smaller grains.

Interestingly, instead of the representative *c*(400) reflection, positioned at around 35° 2θ, two additional discrete peaks were observed in the XRD pattern obtained from the surfaces of all materials sintered at 1550-1600 °C (Figure 29), which was further confirmed after inspecting the 72.5–75° 2θ region (plotted in Figure 30b). The observed two peaks are characteristic of the high-temperature, yttria-rich, tetragonal phase, known as *t'*-ZrO_2, which is not transformable to the monoclinic structure. It is formed upon cooling via a diffusionless transition from the cubic phase, which in turn is formed by partitioning during the sintering at high temperatures [25]. Compared to the transformable *t*-ZrO_2 in the 3Y-TZP, the untransformable *t'*-ZrO_2 possesses a much smaller degree of tetragonality and a much higher yttria content [119].

Thus, in 0.25A-TZ/SiO_2 ceramics exhibiting a bi-modal grain size distribution, the large grains containing a larger amount of yttria are composed of *t'*-ZrO_2 rather than of *c*-ZrO_2, as it is usually described in the literature.

It is important to note, that the relative intensities of the reflections characteristic of the *t'*-ZrO_2 phase in the pattern of the 0.25A-TZ/SiO_2 were noticeably lower compared to other materials sintered at the same temperature, suggesting that in this material the phase-partitioning process was more retarded than in other materials. This was quantitatively confirmed by a determination of the remaining untransformed *t'*-ZrO_2 after ageing until the saturation with the monoclinic phase, yielding values of 26.3, 26.6, 32.6 and 21.4 wt. % for the TZ, TZ/SiO_2, 0.25A-TZ and 0.25A-TZ/SiO_2 material, respectively.

Another interesting observation related to the microstructure of the as-sintered co-doped 0.25A-TZ/SiO_2 ceramics warranted attention, namely, no α-alumina grains were found in this material neither by SEM analysis (Figure 26) nor by Raman studies (Figure 31), even when it was sintered at 1600 °C. Alumina could form mullite with silica upon heating at high temperatures. Besides, no signals corresponding to mullite were observed in Raman spectrum of 0.25A-TZ/SiO_2 (Figure 31). According to the Al_2O_3-Y_2O_3-ZrO_2 phase diagram [120] the solubility of alumina in zirconia increases with the decreasing yttria content and increasing sintering temperature. In fact, in 0.25A-TZ/SiO_2 ceramics sintered at 1600 °C the phase partitioning is already pronounced, but, with the reference to Table 13, the amount of untransformable phase was relatively low, preserving high yttria content in the tetragonal zirconia grains. Therefore, solid solubility of alumina in tetragonal zirconia grains can be increased by the presence of silicate phase.

The impedance studies revealed that the specific grain boundary resistivity of 0.25A-TZ/SiO_2 material is ~10 orders of magnitude higher than that of 0.25A-TZ. It was reported that the resistivity of Y-TZP ceramics varies significantly with the grain size [121]. However, both pure and silica-doped 0.25A-TZ materials had similar grain sizes and, thus, other factors should be considered to explain the difference in grain boundary resistivity. As already mentioned, in 0.25A-TZ/SiO_2 material sintered at 1450 °C no silica grain boundary segregation was observed, and the amorphous silica phase was only located at the triple grain junctions. It was shown that adding of small amounts of silica (less than 5 wt. %) does not affect the grain boundary conductivity of Y-TZP [122]. The blocking effect contributed from the siliceous phase is therefore negligible. The addition of alumina is known to increase the resistivity of 3Y-TZP. However, both 0.25A-TZ and 0.25A-TZ/SiO_2 materials contain the same amount of alumina. Taking into account the results of Raman studies, showing that in 0.25A-TZ/SiO_2 material alumina was dissloved in zirconia, and knowing that both materials revealed the same bulk resistivity, it is reasonable to suggest that in the co-doped material a higher amount of alumina was segregated at the grain boundaries.

In the space charge model a grain boundary consists of a grain boundary core (crystallographic mismatch zone) and two adjacent space charge layers. The commonly observed cation, e.g. yttrium segregation at the grain boundaries is a good indicator of the negative space charges, owing to its negative effective charge in the zirconium lattice (Y'_{Zr}). The positively charged oxygen vacancies are therefore depleted in the space charge layer. The oxygen vacancy depletion in the space charge layer was proposed as the cause of the ‘‘intrinsic’’ grain boundary blocking effect [113]. Implying this model to the obtained results, one can conclude that the higher concentration of alumina at the grain boundaries of 0.25A-TZ/SiO_2 material decreases the oxygen vacancy concentration in the space charge layer.

5.2.2 Mechanical properties

Our results (Table 10) show that alumina slightly increases the flexural strength of 3Y-TZP. This may reflect the change in the fracture mode when small amounts of alumina are present. Silica, in turn, does not have any effect on flexural strength and consequently on the fracture mode of 3Y-TZP. Similar to alumina-doped 3Y-TZP the alumina and silica co-doped material had a sligthly higher flexural strength compared to un-doped material. Neither single-doping nor co-doping practically does not have effect on the fracture toughness of 3Y-TZP

5.3 LTD

The obtained results indicate that in the investigated systems the grain size was not the prevailing factor influencing the transformability of the 3Y-TZP under hydrothermal conditions. The minor alumina and/or silica additions followed by sintering at temperatures ≤1500 °C to a large extent do not change the densities, grain sizes or mechanical properties of 3Y-TZP, but they do significantly reduce the LTD. The alumina- or alumina/silica co-doping followed by sintering at higher temperatures even increases the grain growth of 3Y-TZP, but again, significantly decelerates the ageing. Other microstructural features (grains shape, the presence and location of second phases) as well as phase relations in ZrO_2-Y_2O_3 and Y_2O_3-SiO_2-Al_2O_3 systems should be taken into account in order to explain the effect of alumina- or/and silica- doping and co-doping on the LTD of tetragonal zirconia.

5.3.1 Effect of alumina

In spite of the low solubility, the presence of alumina noticeably decreases the rate of the moisture-induced *t*-*m* transformation, as evidenced by the ageing curves (Figure 45) and additionally supported by optical micrographs of cross-sections of aged samples (Figure 46 and Figure 47) and by FIB-SEM analysis (Figure 50b). Even a relatively low amount of alumina (0.05 wt.%) in 0.05A-TZ already showed a lower ageing rate (Figure 46) and a mixed fracture mode (Figure 35). It should be noted that 0.05A-TZ material contains a slightly higher amount of yttria compared to TZ. The effect of small changes in the content of yttria on LTD was not studied in the present work, but it may also contribute to higher overall ageing resistance of 0.05A-TZ. As shown in subsection 5.2.1 the amount of alumina in 0.05A-TZ materials sintered at 1400-1600 °C for 2 h lies within its solubility limit in *t*-zirconia. Therefore with increasing of sintering temperature the amount of alumina at the grain boundaries of 0.05A-TZ increases. Due to the counteracting effect exerted by reduced surface energy term opposing the transformation and increased alumina concentration per unit grain area, a less pronounced grain size dependence of LTD in 0.05A-TZ material could be expected. For example, the 0.05A-TZ material sintered at 1550 °C for 2 h (with grain size of 0.44 μm) should have higher concentration of alumina at grain boundaries, compared to the same material sintered at 1450 °C for 4 h and having the grain size of 0.31 μm. To confirm the above assumption, both materials were aged for 6-48 h at 134 °C. As shown in Figure 56 materials exhibited very similar ageing properties, confirming that the effect of larger grains in material sintered at 1550 °C for 2 h is indeed compensated by the higher amount of Al^{3+} segregated at the grain boundaries. After ageing for 24-48 h the surface of 0.05A-TZ material sintered at 1550 °C contains an even lesser amount of monoclinic phase. However, the careful study of XRD (Figure 57) profiles showed that in both materials the saturation in monoclinic phase is almost reached such that the above result could reflect a higher amount of

untransformable phase in the higher-temperature sintered 0.05A-TZ.

Anyway, regardless of this uncertainty, the above result shows that with increasing of concentration of Al^{3+} at the grain boundaries the hydrothermal stability of tetragonal zirconia increases.

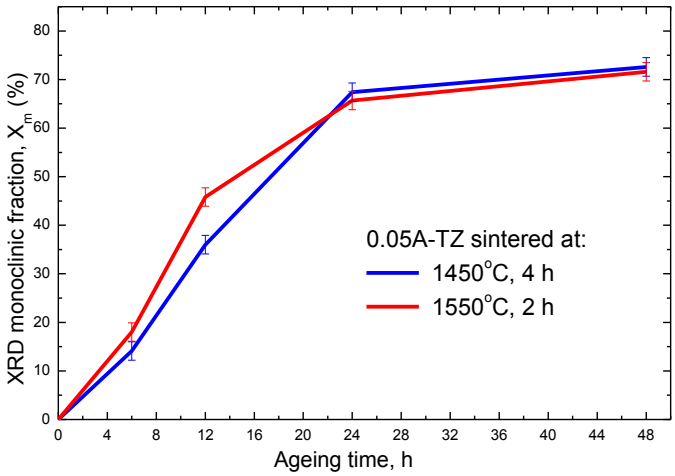


Figure 56: Calculated monoclinic fraction versus in vitro ageing time for pure and silica-doped, 0.05A-TZ materials sintered at 1450 °C for 4 h and 1550 °C for 2 h.

Given that high alumina-doped (0.25 wt.%) materials preferentially fractured in a transgranular mode (Figure 34) and also showed a low density of microcracks in the transformed surface layer upon ageing (Figure 50b), the presence of alumina is likely to reduce the local strain at the grain boundaries. Namely, segregation of impurities commonly influences the grain boundary cohesion and its strength when under stress.

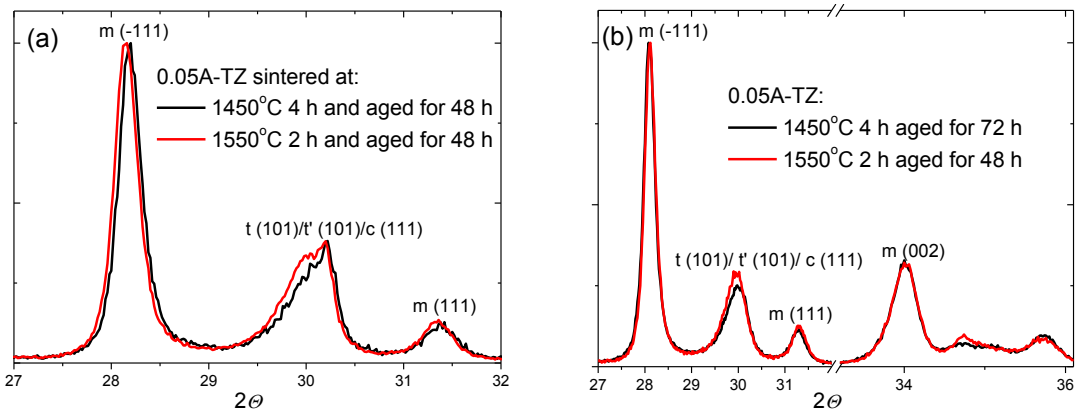


Figure 57: XRD patterns obtained from the surfaces of 0.05A-TZ materials sintered at 1450 °C for 4 h and 1550 °C for 2 h and aged for (a) 48 h and (b) 72 h.

The higher proportion of transgranular fracture for the alumina-doped 3Y-TZP ceramics (Figure 34) thus suggests much stronger cohesion between the grains which in turn may also exert a constraining effect hindering the formation of the monoclinic phase upon ageing, as well as microcracking. According to Chevalier et al. [76] (Figure 13) the latter initiates at the surface and propagates along (randomly oriented) grain boundaries into the bulk thereby facilitating water penetration and hence accelerating LTD by a stress corrosion type mechanism. However, as demonstrated by several other groups, microcracks originating from LTD run preferentially in a direction parallel to the surface [123], [124] and in accordance with recent work of Jimenez-Pique et al. [125] they are also not connected to the surface. Based on these (new) findings, Chevalier's proposed scheme for LTD propagation has been questioned and another mechanism for the

propagation of the monoclinic phase into the bulk (i.e. autocatalytic propagation) was proposed by Munoz-Tabarez [124]. Our FIB-SEM studies (e.g. those presented in Figure 49 and Figure 50) strongly support preferential microcrack alignment, on the other hand we do see a relationship between the microcrack density and the thickness of the transformed layer. The SEM micrograph of the top region of 0.25A-TZ material sintered at 1600 °C and aged for 72 h (Figure 58) clearly shows the presence of microcraks and they preferentially propagate intergranularly. Therefore, before the Munoz-Tabarez's et al. alternative mechanism is adopted, the (un)accessibility of water into the preferentially aligned microcrack network should be unambiguously clarified.

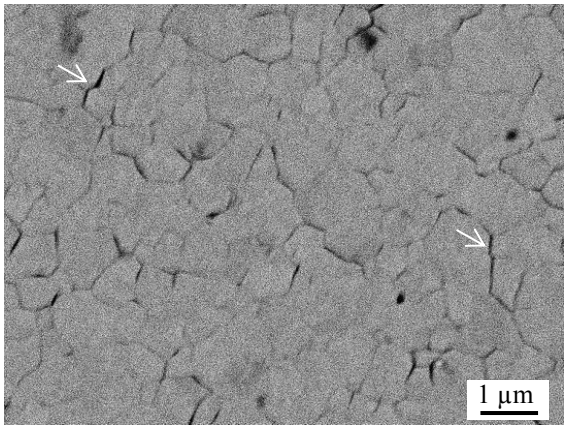


Figure 58: SEM micrograph of 0.25A-TZ material (top region) sintered at 1600 °C and aged for 72 h. White arrows point to grain boundary microcracks.

The higher cohesion between the grains in the alumina-doped 3Y-TZP observed in the present work was anticipated by Tsubakino et al. [99] in 1991, but without providing any direct evidence. Moreover, these authors suggested that the strong cohesion between grains in 3Y-TZP could be related not only to the alumina segregation, but also to the formation of the silica phase at the grain boundaries. However, in the present study no substantial changes in the fracture mode between the silica-free and silica-doped materials were observed (Figure 34-Figure 36). Therefore, the cohesion between the grain boundaries is strongly related to the alumina segregation in 3Y-TZP regardless of whether silica is also present or not. Recently, another study showed that when 3Y-TZP was co-doped with alumina and lanthana, both dopants segregated to the grain boundaries causing a dramatic reduction in the extent of microcracking [105].

In addition to its role in hindering the propagation of the transformation, the presence of alumina should also influence the nucleation of ageing before any microcracks are formed. Segregated alumina could prevent the reaction between hydroxyl groups (OH^-) and Y_2O_3/ZrO_2 [126] by forming either mononuclear aluminum soluble species, or hydrated alumina particles, depending on the pH, temperature, and the presence of other ionic species, or solid phases. A similar role in decreasing the tendency to age for the 3Y-TZP doped with small amounts of MnO_2 was proposed by Ramesh et al. [127], who suggested that the formation manganese-rich compounds could have prevented hydroxyl reaction with zirconia or yttria. Besides, taking into account the literature data reporting on increased grain boundary resistivity in alumina-doped Y-TZP [128], due to the formation of complex defect associates, which binds some oxygen vacancies to immobile ions, it can be assumed that alumina segregation at the grain boundaries has a potential of decreasing the concentration of free oxygen vacancies which, in turn should increase the stability of the tetragonal zirconia. This effect will depend on the enhanced diffusivity of yttrium cations toward alumina-rich grain boundaries, a phenomenon first reported by Murase et al. [72], as well as on the amount of alumina accommodated at the grain boundaries.

5.3.2 Effect of silica

According to results presented in Figure 51, the effect of silica on the LTD of TZ depends on the sintering temperature of doped material. The addition of small amounts of amorphous silica into TZ followed by sintering at temperatures < 1500 °C for 2 h resulted in substantial deceleration of the LTD, while the addition of silica into TZ followed by sintering at temperatures ≥1500 °C led to the material with ageing properties similar to silica-free TZ, i.e. it practically does not reduces the LTD.

In the former case the role of silica is clear in that it mainly reduces the strain within the grains, especially at the triple points [107], which is important for both the nucleation and propagation of LTD. Anticipating that LTD in silica-free ceramics starts at grain corners, where internal stresses are highly localized [74], the tentative explanation by Gremillard et al. [107] can be adopted for the reduced sensitivity to moisture-induced transformation of silica-doped materials, which builds on hindered nucleation of the transformation due to reduced local stress at multiple grain junctions. Besides, with reference to FIB-SEM micrograph in Figure 50c, reduced strain due to rounded grains and/or amorphous glassy phase at the grain junctions evidently hinders the formation of microcracks in the transformed surface layer. Being so, silica doping not only hinders the nucleation, but also reduces the propagation of the transformation into the bulk via water penetration along the cracks.

The Y_2O_3-SiO_2 phase diagram (Figure 59) can help to explain the sintering temperature related change in the ageing behavior of TZ/SiO_2 material. Namely, the diagram predicts the formation of yttrium silicate at temperatures ≥ 1500 °C [129]. This could be a driven force for a diffusion of yttria from the tetragonal grains into amorphous silica phase, leading to a reduction of yttria content in *t*-grains, which will increase the susceptibility of 3Y-TZP to hydrothermal degradation.

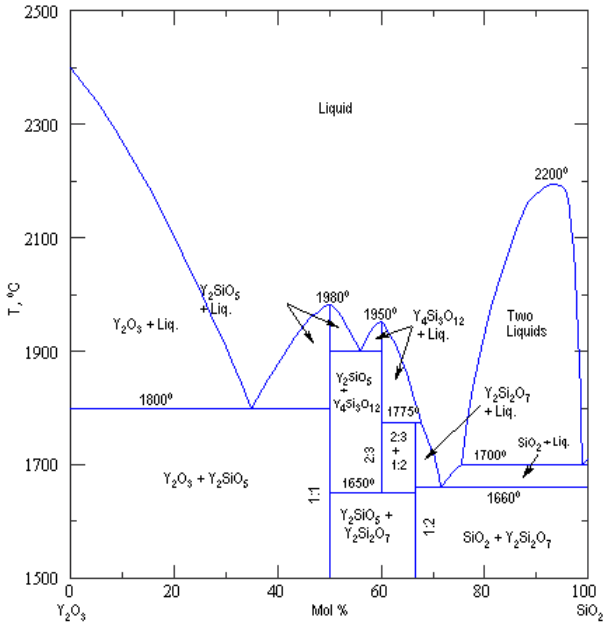


Figure 59: Y_2O_3-SiO_2 phase diagram. (Source: Toropov et al. [129]).

In fact, as will be shown in the next chapter, the formation of new yttria-reach phase within the glassy phase was observed in coupled-diffusion experiment in TZ/SiO_2 system. Therefore, according to the results of present work, the silica single-doping is an effective method to decelerate the LTD of TZ only when it sintered at temperatures below 1500 °C.

5.3.3 Effect of co-doping

In contrast to silica-doped TZ/SiO_2 material the co-doped 0.05A-TZ and 0.25A-TZ/SiO_2 materials revealed improved ageing properties even when they were sintered at temperatures ≥ 1500 °C, indicating that alumina has an impact on the reactivity in Y_2O_3-ZrO_2-SiO_2 system.

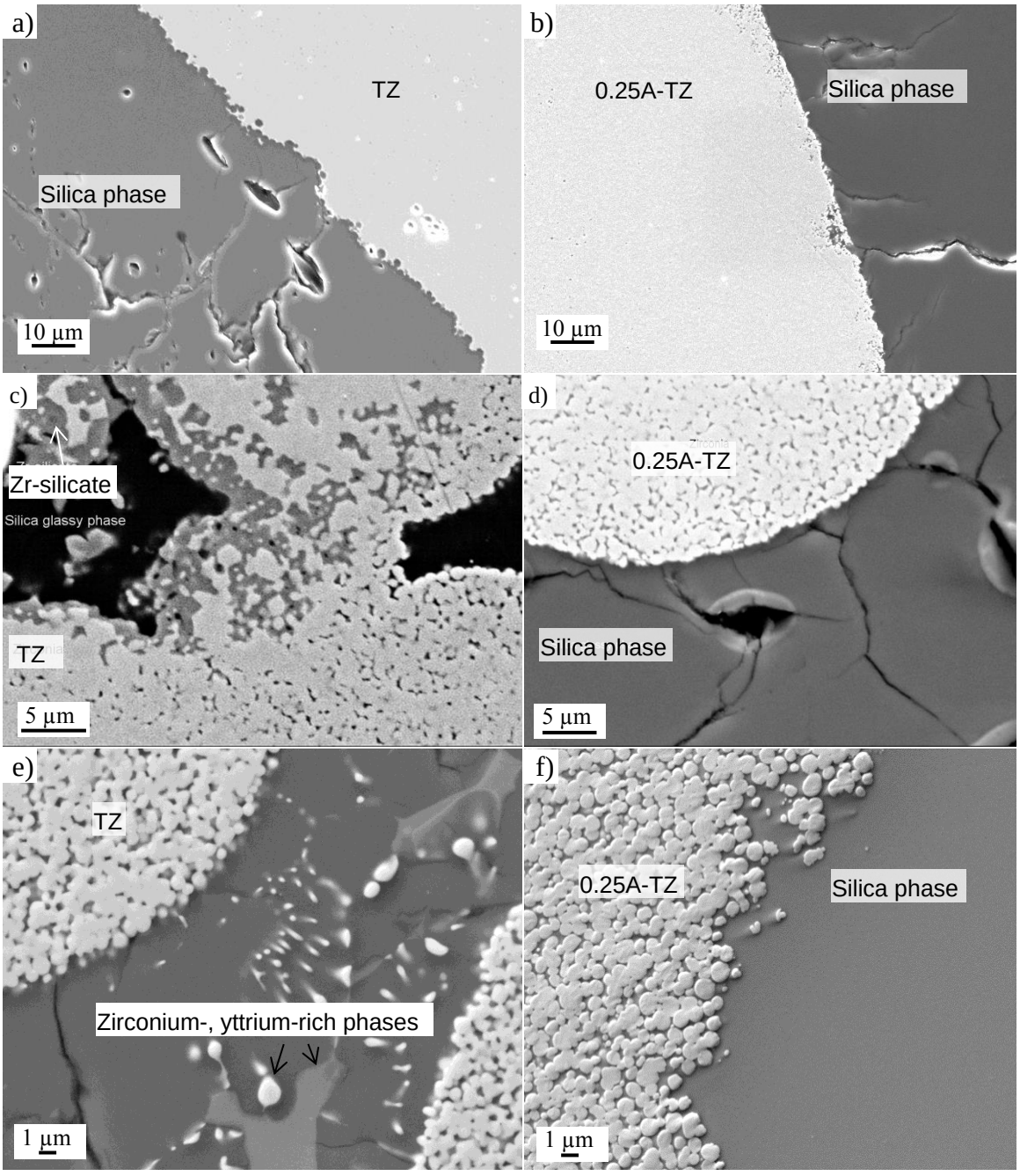


Figure 60: SEM micrographs of polished specimens after the diffusion coupled experiment performed at different annealing/sintering conditions. (a) TZ/SiO_2 and (b) 0.25A-TZ/SiO_2 annealed/sintered at 1450 °C for 4 hours (c) TZ/SiO_2 and (d) 0.25A-TZ/SiO_2 annealed/sintered at 1450 °C for 50 hours; (e) TZ/SiO_2 and (f) 0.25A-TZ/SiO_2 annealed/sintered at 1500 °C for 8 hours.

In order to get a better insight into the possible effects of silica-doping and co-doping, a few diffusion-coupled experiments in the TZ/SiO_2 and 0.25A-TZ/SiO_2 systems were conducted (Figure 60). TZ and 0.25A-TZ powders were mixed with a larger amount of

highly reactive silica synthesized using the sol-gel method (the same as used for the infiltration), pressed into pellets and sintered under different conditions, i.e. at 1450 °C for 4 and 50 hours, and the other at 1500 °C for 8 hours. The polished cross-sections of the diffusion couples were analyzed using XRD, SEM and EDS with emphasis on the phase relations and the composition of the glassy phase. These were thought to be indicative for the diffusivity of yttrium and aluminum cations relevant for both the zirconia phase partitioning and LTD. No signs of reactions between silica and TZ or 0.25A-TZ were observed after annealing at 1450 °C for 4 h (Figure 60). However, after annealing for a longer time or at higher temperature much higher reactivity was observed in TZ/SiO_2 system. The XRD pattern of obtained samples did not show any new peaks indicating that the new compounds (if any) were present in the samples at concentrations below the detection limit of XRD. EDS analysis revealed the formation of yttria-reach silica phase in the glassy phase of the specimen annealed at 1500 °C for 8 h in agreement with Y_2O_3-SiO_2 phase diagram, showing the formation of yttrium silicate at 1500 °C. This explains the previously mentioned temperature-related change in the ageing properties of TZ/SiO_2 material, which showed higher stability compared to TZ, when sintered at temperatures $\leq$1450^{o}C, but only slightly improved ageing properties when sintered at higher temperatures. Notwithstanding that there are many factors influencing the phase equilibria in a given system, (e.g. temperature, time, size, shape of reactants, etc.) the above results clearly show a much higher reactivity of the "pure" TZ/SiO_2 system compared to the 0.25A-TZ/SiO_2 system confirming that alumina substantially influences the composition and properties of the glassy phase between rounded zirconia grains.

Since the yttria-rich silica phase in TZ/SiO_2 system appears at temperatures $\geq$ 1500 °C, the presence of small amounts of alumina has a critical role in the hydrothermal stability of TZ/SiO_2 system sintered at the same temperatures.

At higher sintering temperatures, i.e. 1550-1600 °C, the amorphous phase was found not only at triple grain junctions, but also along the grain boundaries in 0.25A-TZ/SiO_2. This should further reduce the internal stresses and stresses, appearing during the propagation of LTD. On the other side, the temperature-related ($\geq$1550 °C) penetration of the silica phase from the grain junctions into the grain boundaries was accompanied by the emergence of a fraction of yttria-reach larger *t`* grains. These larger grains are usually thought to be co-existing in equilibrium with the more readily transformable (yttria-lean) *t*-ZrO_2, which in turn were shown to act as the sites for the nucleation of LTD. However, as shown in Table 13, 0.25A-TZ/SiO_2 material the phase-partitioning process was more retarded than in the other materials. This observation corroborates with the observations from a coupled diffusion experiment, where it was shown that alumina hindered the diffusion of the Y^{3+} and Zr^{4+} into the silica phase, reducing the reactivity of that specific system. Thus, the much smaller amount of *t'*-ZrO_2 phase in the 0.25A-TZ/SiO_2 resulted in a less-depleted *t*-ZrO_2 grains, increasing the overall resistance to ageing. Moreover, the 0.25A-TZ/SiO_2 maintained its integrity, even after ageing under extreme conditions (e.g. 240 h at 200 °C), while upon ageing under the same conditions the 0.25A-TZ material disintegrated. Thus, the co-doping of the 3Y-TZP bioceramics with alumina and silica ensures a greater resistance to ageing, as compared to the single-doped alumina 3Y-TZP, not only when sintered at moderate temperatures, but also when higher sintering temperatures are employed.

In summary of this chapter it can be concluded, that the addition of either alumina or silica has the potential to influence both the nucleation and the propagation of moisture-induced transformation, but in a different manner and to a different extent. These two additives evidently have different mechanisms for the deceleration of LTD of 3Y-TZP. When they are combined the resistance to ageing futher increases (Figure 45) and, importantly, without reducing the fracture toughness and flexural strength of the material

(Table 8 and Table 10).

It should be pointed out here that this statement not only holds for materials before ageing, but also for materials after ageing. Optical micrographs of aged ceramics illustrated the dramatic difference in doped and co-doped material's response to Vickers' indentation (Figure 54). Superior ageing resistance of co-doped material resulted in sharp, microcrack-free impression edges even after 48 h of ageing. The latter also implies superior behaviour of co-doped zirconia under wear and cyclic loading conditions in an aqueous environment. The flexural strength of co-doped material aged for 24 h (Table 14) was nearly identical to that before ageing (Table 10), indicating that under these ageing conditions neither significant strengthening (due to transformed surface layer) nor substantial strength degradation (due to microcracking and/or lamination) has occurred.

5.4 Influence of the Yttria Distribution (Heterogeneities/Segregation) in 3Y-TZP Grains on the LTD

It was reported that not only the overall yttria content, but also the yttria distribution in sintered 3Y-TZP ceramics should be considered as one of the crucial factors controlling the LTD behaviour of Y-TZP ceramics. As it was already noticed [72], the yttria-rich non-transferable, presumably, cubic phase, as stated previously, has a critical role on the nucleation of hydrothermal ageing, because the remaining yttria-lean t grains will act as the nucleation sites for the LTD.

Large yttria-rich *t'* grains are clearly discernible from small t grains in the SEM micrographs of co-doped 0.25A-TZ/SiO_2 materials sintered at 1550-1600 °C (Figure 27). However, due to very uniform microstructures of TZ and single-doped ceramics sintered at the same temperatures (Figure 26-27), it was difficult to distinguish the *t* and *t'* phases in these materials.

The location of yttria-rich *t'* phase can be estimated by SEM analysis of the aged until the saturation surfaces of 3Y-TZP ceramics. The *t'* phase is expected to be visible as untransformed grains or part of the grains within the martensitically transformed monoclinic grains.

In a fact, as illustrated in Figure 61 in sintered at 1600 °C and aged until the saturation TZ and single-doped (TZ/SiO_2 and 0.25A-TZ) materials three types of grains were observed: 1) the fully transformed tetragonal grains, having visible martensitic relief, induced by the t-m transformation, 2) fully untransformed grains, having in most cases a small size < 0.3 μm and 3) relatively large grains (≥ 1 μm), having one part untransformed (white arrows) and one part transformed to the monoclinic phase.

It should be noticed that the imperfections (which are hardly distinguished from martensitic relief) were also observed on the surfaces of as-sintered materials. Therefore to study the origin of all microstructural imperfections in aged materials a more careful study (by AFM) should be done, but this was not the goal of the present experiment.

Regardless of the uncertainties in the origin of microstructural relief, the location of untransformable phase can be estimated. The microstructures of aged until the saturation TZ, TZ/SiO_2 and 0.25A-TZ ceramics are very similar, i.e. in all materials there are grains, in which one part consists of nontransformable *t'* phase (Figure 61a-c, white arrows). The formation of *t'* phase in these materials is most probably a diffusion-controlled process. In fact, the phase partitioning in zirconia depends on the dopant (yttria, alumina, etc.) segregation to the grain boundaries. Matsui et al. [104] reported that alumina accelerates the phase partitioning in 3Y-TZP. Our results confirm this assumption (Table 13).

In contrast, the microstructure of co-doped 0.25A-TZ/SiO_2 material consisted of the smaller tetragonal grains, which were fully transformed, having visible surface changes

induced by the emergence of the monoclinic martensitic variants, and large *t'* grains, which tend to remain untransformed. The large grains contain the inner heterogeneities, i.e. small tetragonal grains (dashed box in Figure 61d), which were fully transformed.

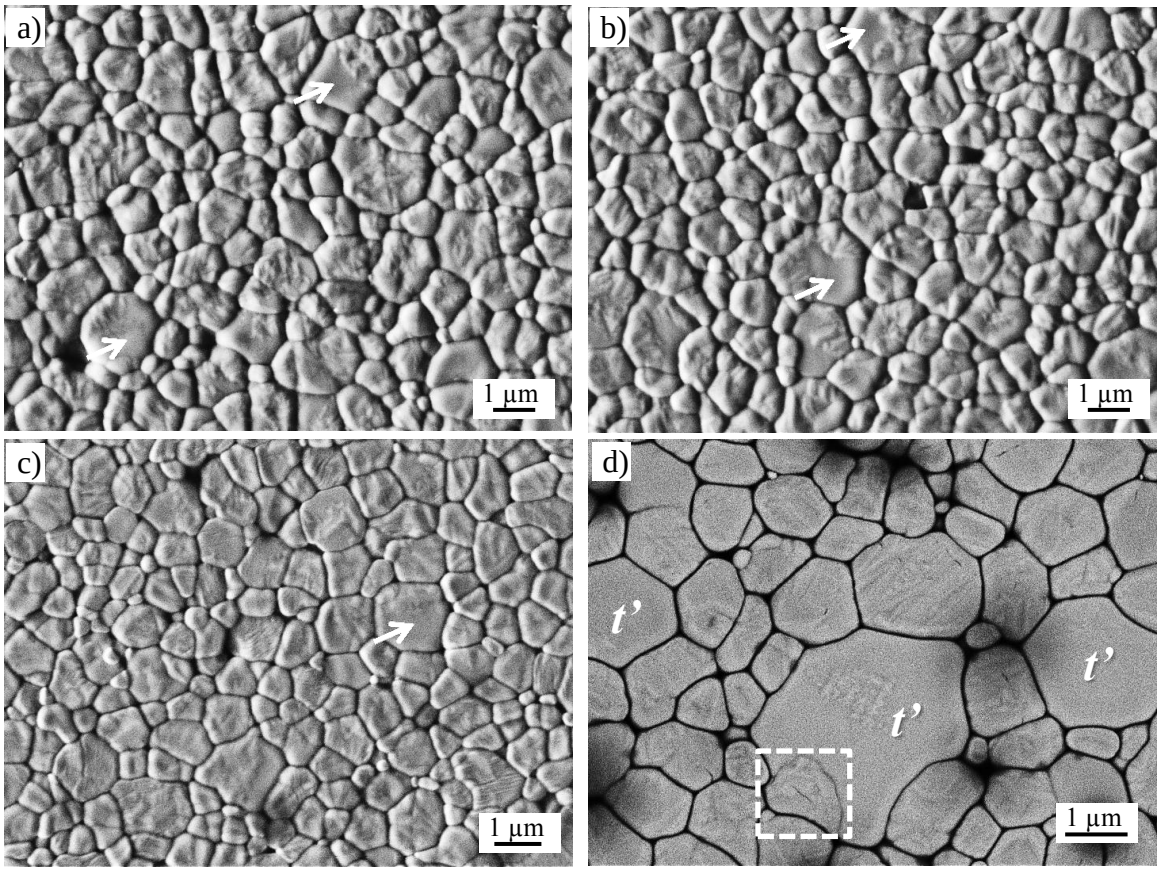


Figure 61: SEM micrographs of sintered at 1600 °C for 2 h and aged until the saturation (a) TZ, (b) 0.25A-TZ, (c) TZ/SiO_2 and (c) 0.25A-TZ/SiO_2 materials. White arrows point to untransformed parts of the grains.

The appearance of inner heterogeneities in large *t'* grains in the yttria-diffusion-limited conditions (paragraph 5.3.3 implies that in 0.25A-TZ/SiO_2 an alternative mechanism of grain growth might be operating next to the classic, diffusion-controlled process. Recently, a novel grain growth mechanism resulting from multiple ordered coalescence was suggested for a couple of ceramic materials and confirmed based on TEM studies [130]–[132]. We supposed that the inner yttria-lean heterogeneities (Figure 61d, dashed box) can be coalesced grains.

In order check this assumption a large grain surrounded by smaller *t*-ZrO_2 grains in 0.25A-TZ/SiO_2 material sintered at 1600 °C, where a possible initiation of the ordered grain coalescence section was identified and analysed using the TEM (Figure 62). The smaller grain (labelled *t*) had a family of (110) plains oriented in the same direction as the large grain as had several other neighbouring smaller grains. In the selected-area electron diffraction (SAED) region 1 (Figure 62 a), where the smaller, individual, tetragonal grains (t) start to merge into the large one, the diffraction pattern indicates an almost perfect crystallographic match between the orientations of both grains (Figure 62b). This suggests that, prior to the coalescence, grain-rotation within the amorphous phase may occur, thereby reducing the angle of misorientation. Just under the merging region 1, there is a clearly visible, larger pocket of an amorphous silica layer within the grain boundary (red arrow - region 2; EDXS - red spectra). It is believed that the silica was squeezed out from the merging region into the pocket beneath, due to its insolubility in

zirconia at room temperature. The SAED acquired from the same region (Figure 62c) shows the pattern of both crystals, i.e., unchanged peaks corresponding to the (110) planes of the large grain and slightly tilted peaks corresponding to the same planes of a smaller grain. In region 3 (Figure 62d), going further into the smaller grain, the diffraction corresponding to the (110) planes revealed that, with respect to the larger hosting grain, this region was even more tilted than region 2 (Figure 62c).

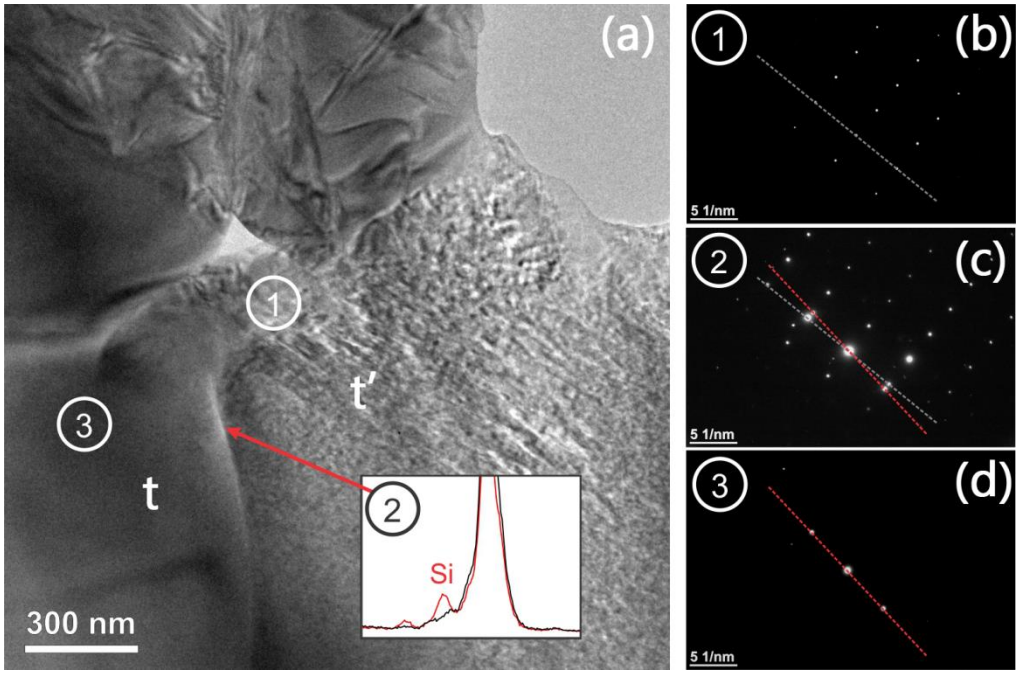


Figure 62: TEM micrograph of the 0.25A-TZ/SiO_2 sintered at 1600 °C for 2 h. (a) The micrograph reveals the initiation of grain coalescence, i.e., the region where smaller *t*-ZrO_2 grain merged with a larger *t'*-ZrO_2 grain. The numbered circles represent the location where the SAED were performed and are shown in Figure b–d. (b) the merged region, (c) the silica-containing grain boundary located beneath the merged region, (d) the smaller *t*-ZrO_2 grain.

Heterogeneities, i.e. *t* grains, in the as-formed large grains, coalesced from the smaller neighbouring grains, in terms of un-even yttria distributions are highly likely. This is because each newly coalesced grain has a different net amount of yttria, leaving behind "quasi-interfaces" and substructures [131]. Several other indications of such features are presented in Figure 63. Figure 63a shows two large, heterogeneous grains: (i) in the dashed box is a smaller grain coalesced into a larger one, with a still visible inner grain boundary; (ii) in the dotted box is an inner region having some sort of substructures, exhibiting a distinct surface roughness. In Figure 63b is an FIB-SEM sub-surface microstructure of a larger grain with light-grey contrast. On its right-hand side, in a white box, a smaller domain of faintly darker contrast (possibly indicating a slightly tilted orientation, as observed with TEM in Figure 62b) can be seen along with an inner "quasi-interface".

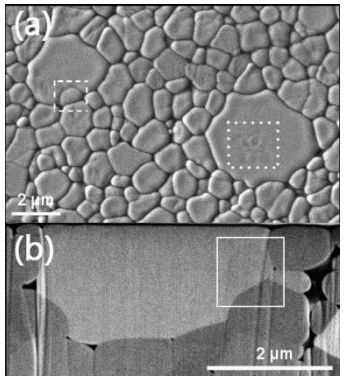


Figure 63: (a) SEM micrograph and (b) FIB-SEM sub-surface microstructure of 0.25A-TZ/SiO_2 sintered at 1600°C for 2 h.

The grain growth of *t'* by ordered coalescence suggests that in 0.25A-TZ/SiO_2 material the distribution of yttria should be more homogeneous. If it is so, in this material the large *t'* grains will not have a critical role on the ageing resistance. To confirm the idea, 0.25A-TZ/SiO_2 material sintered at 1600 °C and aged for 3 h was studied by SEM analysis (Figure 64). After 3 h of ageing the martensitic relief induced by *t-m* transformation is clearly visible (white arrows). As it was expected, tetragonal grains, which are the nearest neighbours to a larger grain, remained untransformed. However, SEM analysis is not sufficient to confirm the above assumption, further AFM studies are needed.

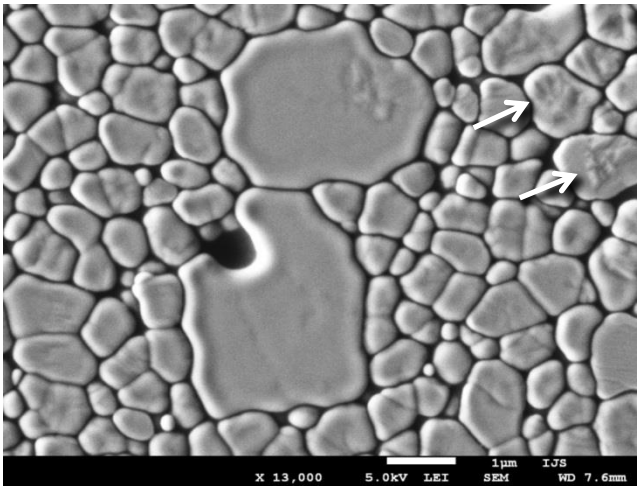


Figure 64: 0.25A-TZ/SiO_2 material sintered at 1600 °C and aged for 3 h. White arrows point to martensitic relief.

It should be noticed, that in 3Y-TZP ceramics the difference in dopant concentration can be observed not only between grains, but also within the one grain. In present work the yttria/alumina distribution within the transformable *t* parts of the grains in 3Y-TZP materials was not studied by direct measurements. However, our impedance measurements and studies of fracture modes support the observations made by Matsui, that dopants tend to segregate to the grain boundaries.

At the same time the LTD is known to nucleate at the triple points and grain boundaries, where the higher internal stresses are localized [74], [75].

Thus, the higher concentration of dopants at the grain boundaries and the nucleation of LTD at the triple points or/and grain boundaries contradict the fact that the increasing of yttria or/and alumina content improves the hydrothermal stability of Y-TZP. It looks like the segregation of yttria to the grain boundaries has a negative effect on the LTD stability of *t*-zirconia grains. Knowing that Y^{3+} is larger than Zr^{4+}, it is surmised that upon segregation to the grain boundaries, the large Y^{3+} weakens the interatomic bonding by

pushing apart the Zr^{4+} at the interface. This, in turn, can explain the weak grain boundaries in pure 3Y-TZP, which were observed by studying the fracture mode (Figure 34). In the case of alumina-doped 3Y-TZP the yttrium segregation is subdued by the preferential segregation of aluminium cation (Al^{3+}) [133]. Since Al^{3+} is smaller compared to Zr^{4+}, it will not create additional stresses. However, other evidences are needed to prove these assumptions.

5.5 Origin of the Low-Theta Broadening of $(1\ 01)_t/(1\ 1\ 1)_c$ Peak on the XRD of Aged 3Y-TZP

The XRD pattern of aged 3Y-TZP materials revealed the low-theta broadening of the most intense $(1\ 01)_t/(1\ 1\ 1)_c$ peak (Figure 43-Figure 44). Similar asymmetry of that peak was often observed for fully, partially stabilized and tetragonal zirconia after ageing, grinding, sandblasting or fracture [134]–[136]. Several interpretations of the origin of this asymmetry were suggested. Some studies reported the existence of the extraordinary phase such as the rhombohedral phase in the ZrO_2–Y_2O_3 system based on the results of XRD [134], [135], [137], [138]. It has been suggested by several authors that the stresses which appear after *t-m* transformation under the hydrothermal conditions could cause the appearance of rhombohedral phase. Kondoh [136] studied the origin of the hump in XRD of fully and partially stabilised zirconia annealed at different temperatures and for different times. Based on the XRD results and the results of EXAFS this author concluded that a hump is caused by lattice distortion and is not derived from the rhombohedral phase.

For clarification of the origin of $(1\ 01)_t/(1\ 1\ 1)_c$ peak asymmetry, which appears in tetragonal zirconia after the LTD the TZ material sintered at 1450 °C for 50 h was chosen and studied by XRD analysis before and after ageing for 24 h.

In the XRD pattern of this material the cubic peak positioned at 35 °2Θ is clearly visible (Figure 65). After the hydrothermal ageing no tetragonal peaks were observed, implying that this material was fully transformed. Instead of $(1\ 01)_t/(1\ 1\ 1)_c$ peak the signal corresponding to the untransformable phase was observed. This peak was shifted to the left side compared to the initial t/c peak. At the same time the cubic peak positioned at 35 °2*Θ* was shifted to the left side as well, confirming that the asymmetry of the $(1\ 01)_t/(1\ 1\ 1)_c$ peak is not likely to be derived from the rhombohedral phase. The shift of XRD peaks with ageing therefore implies the existence of lattice distortion in as-sintered 3Y-TZP and subsequent relaxation due to ageing. The relaxation of the cubic lattice could create additional stresses on the neighbouring tetragonal zirconia grains and thereby accelerating the ageing. Thus the presence of the cubic phase not only decreases the overall amount of yttria in the neighbouring tetragonal grains but also produces additional stresses during the ageing. These stresses have been substantially reduced in 0.25A-TZ/SiO_2 material by the amorphous silica phase presented at the grain junctions and the grain boundaries.

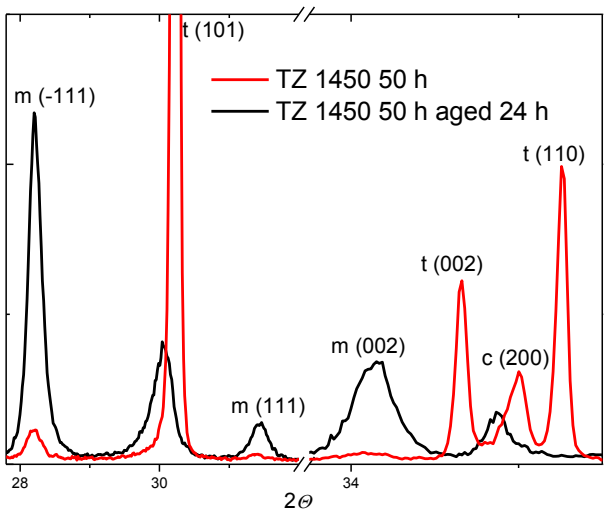


Figure 65: XRD patterns obtained from the surfaces of as-sintered at 1450 °C and aged for 24 h TZ materials.

6 Conclusions

From the present work, which was designed to study the effect of silica or/and alumina-(co)-doping on the microstructural evolution, mechanical and ageing behaviour of 3Y-TZP biomedical ceramics sintered at temperatures ranging from 1400 °C to 1600 °C the following conclusions can be drawn:

1. The infiltration technique proved to be a successful strategy in the preparation of silica- and alumina-silica-co-doped 3Y-TZP materials. The soaking of pre-sintered discs in silica sol and subsequent sintering produced SiO_2-doped and SiO_2-Al_2O_3-co-doped 3Y-TZP pellets containing 0.15 to 0.25 wt% of amorphous silica, depending on the amount of porosity in biscuit-sintered preforms. These additions to a large extent do not change the final densities and mechanical properties of as-prepaed 3Y-TZP ceramics.

2. In investigated systems the grain size turned out not to be the prevailing factor influencing the LTD resistance of 3Y-TZP ceramics as is generally believed. Irrespective of the difference in the chemical composition, the ceramic microstructures after sintering at 1400-1500 °C for 2 h were practically identical, being unimodal and exhibiting similar grain sizes. However, the ageing resistance was substantially improved by alumina or silica single-doping and was still higher when co-doping was employed.

3. The presence of alumina in 3Y-TZP increases the grain boundary cohesion reflected in increased fraction of transgranular fracture and reduced microcracking upon t-m transformation. In 3Y-TZP sintered below 1550 °C silica is concentrated at multiple grain junctions, where it causes rounding of zirconia grains without affecting the fracture mode and the material does not readily crack upon hydrothermal *t-m* transformation.

4. Increasing the sintering temperatures to 1550-1600 °C resulted in a substantial differences in the microstructures and ageing behaviour of doped and co-doped materials. The addition of 0.25 wt% of alumina increases the grain size of 3Y-TZP, but still significantly decelerates the LTD. In contrast, the addition of silica followed by sintering at higher temperatures does not change the grain size of 3Y-TZP, but silica-containing 3Y-TZP aged much faster compared to alumina-doped material. This behaviour coincides with the formation of yttrium silicate phase in Y_2O_3-SiO_2 system at temperatures $\geq$ 1500 °C, which is the driving force for the diffusion of yttria into silica phase, thereby decreasing the yttria content in tetragonal grains. In the presence of alumina the diffusion of yttria into the silica phase is hindered at sintering temperatures $\geq$ 1500 °C.

5. In alumina-silica co-doped 3Y-TZP the temperature-related ($\geq$1550 °C) penetration of the silica phase from the grain junctions into the grain boundaries was accompanied by the emergence of a fraction of larger, heterogeneous grains. The overall partitioning process was slowest in the co-doped material, leaving the higher amount of yttria in tetragonal grains and thereby decelerating the LTD.

6. Upon the cooling the partitioned yttria-rich phase was found to be untransformable (thermodynamically stable at room temperature) tetragonal (*t'*-ZrO_2). The slow partitioning process in co-doped 3Y-TZP corroborates with observations from a coupled diffusion experiment, where it was shown that alumina hinders the diffusion of the Y^{3+} and Zr^{4+} into the silica phase.

7. The alumina grains could be found in co-doped materials neither by SEM nor by

Raman studies indicating that a larger amount of alumina can be dissolved in zirconia grains, i.e. the presence of silica increases the solubility of alumina in 3Y-TZP. This founding was further supported by impedance measurements revealing that alumina-silica-co-doping substantially increases the grain boundary resistivity of 3Y-TZP, also indicating that dissolved alumina is segregated to the grain boundaries.

In summary, there are several reasons for the superior resistance towards LTD of the alumina-silica-co-doped 3Y-TZP ceramics. Namely, compared to pure or/and single-doped materials it contains less amount of yttria-rich *t`*-ZrO_2 phase, i.e. higher amount of yttria in tetragonal grains, and higher amount of alumina at the grain boundaries, while silica reduces the internal stresses and stresses arising during the *t-m* transformation. These factors substantially decelerate the LTD of 3Y-TZP and, importantly, without affecting the fracture toughness.

7 Acknowledgements

This work would not have been possible without the support of many peoples.

I am grateful to my supervisor, Prof. Dr. Tomaž Kosmač, for giving me the opportunity to join his group. He encouraged me not only to grow as an experimentalist, but also as an independent thinker. Thank you for your patience and guidance in developing and improving the dissertation.

I would also like to thank my co-supervisor, Dr. Andraž Kocjan, for his support and enthusiasm for my research. Our conversations helped me to refine my thinking on many of the topics covered in this work.

I would like to acknowledge Dr. Srečo Škapin, who performed the XRD analysis of more than one hundred samples, and Damjan Vengust, who spent evenings in front of the TEM microscope. My great thanks to Dr. Andreja Gajovic from Ruđer Bošković Institute in Zagreb for performing the Raman analysis and Dr. Jože Moškon from the National Institute of Chemistry for the opportunity to carry out the Impedance measurements.

My special thanks to all current and former co-workers at the Jožef Stefan Institute, especially Dr. Aleš Dakskobler for valuable advices and support with the porosimetry measurements, Darko Eterovič and Tomislav Pustotnik for their help with various experimental set-ups, our youngest associate Ana Lazar for keeping me company and Dr. Irena Pribošič for teaching me to operate with SEM.

I wish to acknowledge the Slovenian Research Agency for financial support.

My warmest thanks to my parents, Irina and Yuriy, for their continuous support over the years and encouraging me with their best wishes. Спасибо вам.

8 References

[1] E. H. Kisi and C. J. Howard, “Crystal Structures of Zirconia Phases and their Inter-Relation,” *Key Eng. Mater.*, vol. 153–154, pp. 1–36, 1998.

[2] R. H. J. Hannink, P. M. Kelly, and B. C. Muddle, “Transformation Toughening in Zirconia-Containing Ceramics,” *J. Am. Ceram. Soc.*, vol. 83, no. 3, pp. 461–487, 2000.

[3] M. Rühle and A. G. Evans, “High toughness ceramics and ceramic composites.,” *Prog. Mater. Sci*, vol. 33, pp. 85–167, 1989.

[4] O. Ruff, F. Ebert, and E. Stephen, “No Title,” *Z Anorg Allg Chem*, vol. 180, no. 1, pp. 215–224, 1929.

[5] T. Proffen, R. B. Neder, F. Frey, and W. Assmus, “Defect structure and diffuse scattering of zirconia single crystals doped with 7 mol% CaO,” *Acta Crystallogr. Sect. B Struct. Sci.*, vol. 49, no. 4, pp. 599–604, 1993.

[6] R. C. Garvie and P. S. Nicholson, “Phase Analysis in Zirconia Systems,” *J. Am. Ceram. Soc.*, vol. 55, no. 6, pp. 303–305, Jun. 1972.

[7] R. H. J. Hannink, K. A. Johnston, R. T. Pascoe, and R. C. Garvie, “Microstructural changes during isothermal aging of a calcia partially stabilized zirconia alloy,” in *Science and technology of zirconia*, A. . Heuer and L. w. Hobbs, Eds. Columbus, OH: The American Ceramic Society, 1981, pp. 116–136.

[8] R. C. Garvie, R. H. Hannink, and R. T. Pascoe, “Ceramic steel?,” *Nature*, vol. 258, no. 5537, pp. 703–704, 1975.

[9] P. Rieth, J. Reed, and A. Naumann, “Fabrication and flexural strength of ultra-fine grained Yttria stabilized zirconia,” *Bull Am Ceram Soc*, vol. 55, p. 717, 1976.

[10] T. Gupta, J. Bechtold, R. Kuznickie, L. Cadoff, and B. Rossing, “Effect of stress-induced phase transformation on the properties of polycrystalline zirconia containing metastable tetragonal phase,” *J Mater Sci*, vol. 13, p. 1464, 1978.

[11] K. Kobayashi, H. Kuwajima, and T. Masaki, “Phase change and mechanical properties of ZrO2-Y2O3 solid electrolyte after ageing,” *Solid State Ionics*, vol. 3–4, pp. 489–493, 1981.

[12] P. Christel, A. Meunier, M. Heller, J. P. Torre, and C. N. Peille, “Mechanical properties and short-termin vivo evaluation of yttrium-oxide-partially-stabilized zirconia,” *J. Biomed. Mater. Res.*, vol. 23, no. 1, pp. 45–61, Jan. 1989.

[13] P. Duwez, F. H. Brown, and F. Odell, “The Zirconia-Yttria System,” *J. Electrochem. Soc.*, vol. 98, no. 9, p. 356, 1951.

[14] H. G. Scott, “Phase relationships in the zirconia-yttria system,” *J. Mater. Sci.*, vol. 10, no. 9, pp. 1527–1535, 1975.

[15] O. Fabrichnaya and F. Aldinger, “Assessment of the Thermodynamic Parameters in the System ZrO2–Y2O3–Al2O3,” *Zeit. Met.*, vol. 95, no. 1, pp. 27–39, 2004.

[16] S. Lakiza, O. Fabrichnaya, M. Zinkevich, and F. Aldinger, “On The Phase Relations in the ZrO2–YO1.5–AlO1.5 System,” *J. Alloy. Comp*, vol. 420, pp. 237–45, 2006.

[17] M. Kilo, M. A. Taylor, C. Argirusis, G. Borchardt, B. Lesage, S. Weber, S. Scherrer, H. Scherrer, M. Schroeder, and M. Martin, “Cation Self-Diffusion of 44Ca, 88Y and 96Zr in Single Crystalline Calcia- and Yttria-Doped Zirconia,” *J. Appl. Phys.*, vol. 94, no. 12, pp. 7547–52, 2003.

[18] R. A. Miller, J. L. Sinialek, and R. G. Garlick, “Phase Stability in Plasma-Sprayed Partially Stabilized Zircunia-Yttria,” in *Science and Technology of Zirconia, vol. 3*, A. Heuer and L. W. Hobbs, Eds. Columbus, OH, USA: American Ceramic Society, 1981, pp. 241–253.

[19] A. H. Heuer and M. Riihle, “Phase Transformations in ZrO2-Containing Ceramics: I,The Instability of c-ZrO, and the Resulting Diffusion- Controlled Reactions,” in *Science and Technology of Zirconia II*, N. Claussen, M. Ruhle, and A. H. Heuer, Eds. Columbus, OH, USA, 1984, pp. 1–13.

[20] V. Lanteri, A. H. Heuer, and T. E. Mitchell, “Tetragonal Phase in the System ZrO2-Y2O3,” in *Science and Technology of Zirconia II, vol.12*, N. Claussen, M. Riihle, and A. H. Heuer, Eds. Columbus, OH, USA: American Ceramic Society, 1984, pp. 118–130.

[21] R. Chaim, M. Ruhle, and A. H. Heuer, “Microstructural Evolution in a ZrO2 Wt% Y2O3 Ceramic,” *J. Am. Ceram. Soc.*, vol. 68, no. 8, pp. 427–431, Aug. 1985.

[22] R. Chaim, A. H. Heuer, and D. G. Brandon, “Phase Equilibration in ZrO2-Y2O3 Alloys by Liquid-Film Migration,” *J. Am. Ceram. Soc.*, vol. 69, no. 3, pp. 243–248, Mar. 1986.

[23] C. A. Andersson, J. Greggi Jr, and T. . K. Gupta, “Diffusionless Transformations in Zirconia Alloys,” in *Science and Technology of Zirconia II*, N. Claussen, M. Riihle, and A. H. Heuer, Eds. Columbus, OH, USA: American Ceramic Society, 1984, pp. 78–85.

[24] D. Michel, L. Mazerolles, and M. Perez Y Jorba, “Fracture of metastable tetragonal zirconia crystals,” *J. Mater. Sci.*, vol. 18, no. 9, pp. 2618–2628, Sep. 1983.

[25] V. Lanteri, R. Chaim, and A. H. Heuer, “On the Microstructures Resulting from the Diffusionless CubicTetragonal Transformation in ZrO2-Y2O3 Alloys,” *J. Am. Ceram. Soc.*, vol. 69, no. 10, pp. 258–261, Oct. 1986.

[26] V. Lanteri and a H. Heuer, “On the Microstructures Resulting from the Diffusionless Cubic-Tetragonal Transformation in ZrO 2-Y20 Alloys,” *October*, vol. 261, no. October, pp. 258–261, 1986.

[27] M. Yashima, S. Sasaki, M. Kakihana, Y. Yamaguchi, H. Arashi, and M. Yoshimura, “Oxygen-induced structural change of the tetragonal phase around the tetragonal–cubic phase boundary in ZrO2 –YO1.5 solid solutions,” *Acta Crystallogr. Sect. B Struct. Sci.*, vol. 50, no. 6, pp. 663–672, Dec. 1994.

[28] J. Chevalier and L. Gremillard, “The Tetragonal-Monoclinic Transformation in Zirconia: Lessons Learned and Future Trends,” *J. Am. Ceram. Soc.*, vol. 92, no. 9, pp. 1901–1920, 2009.

[29] M. Yashima, M. Kakihana, and M. Yoshimura, “Metastable-stable phase diagrams in the zirconia-containing systems utilized in solid-oxide fuel cell application,” *Solid State Ionics*, vol. 86–88, no. PART 2, pp. 1131–1149, 1996.

[30] M. Yashima, K. Ohtake, H. Arashi, M. Kakihana, and M. Yoshimura, “Determination of cubic-tetragonal phase boundary in Zr1−XYXO2−X/2 solid solutions by Raman spectroscopy,” *J. Appl. Phys.*, vol. 74, no. 12, p. 7603, 1993.

[31] M. Yashima, N. Ishizawa, and M. Yoshimura, “High-Temperature X-ray Study of the Cubic-Tetragonal Diffusionless Phase Transition in the ZrO2ErO1.5 System: I, Phase Change between Two Forms of a Tetragonal Phase, t’-ZrO2 and t"-ZrO2, in the Compositionally Homogeneous 14 mol% ErO1.5-ZrO2,” *J. Am. Ceram. Soc.*, vol. 76, no. 3, pp. 641–648, Mar. 1993.

[32] J. D. Helmer and T. D. Driskell, “Research on Bioceramics,” in *Proceedings of the Symposium on Use of Ceramics as Surgical Implants.*, 1969.

[33] C. Piconi, S. G. Condo, and T. Kosmač, “Alumina- and Zirconia-based Ceramics for Load-bearing Applications,” in *Advanced Ceramics for Dentistry*, J. Shen and T. Kosmač, Eds. Butterworth-Heinemann: Elsevier/BH, 2014, pp. 219–253.

[34] “Steam re-sterilization causes deterioration of zirconia ceramic heads of total hip prostheses,” *US Food and Drug Administration*, 1997. .

[35] J. Chevalier, L. Gremillard, A. V. Virkar, and D. R. Clarke, “The Tetragonal-Monoclinic Transformation in Zirconia: Lessons Learned and Future Trends,” *J. Am. Ceram. Soc.*, vol. 92, no. 9, pp. 1901–1920, Sep. 2009.

[36] C. Piconi, G. Maccauro, and F. Muratori, “Alumina Matrix Composites in Arthroplasty,” *Key Eng. Mater.*, vol. 284–286, pp. 979–982, 2005.

[37] C. Piconi and G. Maccauro, “Zirconia as a ceramic biomaterial,” *Biomaterials*, vol. 20, no. 1, pp. 1–25, Jan. 1999.

[38] I. Denry and J. A. Holloway, “Ceramics for Dental Applications: A Review,” *Materials (Basel).*, vol. 3, no. 1, pp. 351–368, Jan. 2010.

[39] J. Kelly and I. Denry, “Stabilized zirconia as a structural ceramic: An overview,” *Dent. Mater.*, vol. 24, no. 3, pp. 289–298, Mar. 2008.

[40] M. C. Cehreli, A. M. Kökat, and K. Akça, “CAD/CAM Zirconia vs. slip-cast glass-infiltrated Alumina/Zirconia all-ceramic crowns: 2-year results of a randomized controlled clinical trial.,” *J. Appl. Oral Sci.*, vol. 17, no. 1, pp. 49–55.

[41] A. Örtorp, M. L. Kihl, and G. E. Carlsson, “A 3-year retrospective and clinical follow-up study of zirconia single crowns performed in a private practice,” *J. Dent.*, vol. 37, no. 9, pp. 731–736, 2009.

[42] F. Beuer, M. Stimmelmayr, J. F. Gueth, D. Edelhoff, and M. Naumann, “In vitro performance of full-contour zirconia single crowns,” *Dent. Mater.*, vol. 28, no. 4, pp. 449–456, 2012.

[43] R. Christensen, “Focus on: Monolithic crowns.,” *Dent. Today*, vol. 32, no. 3, p. 22, 2013.

[44] J. D. Griffin, “Tooth in a bag: Same-day monolithic zirconia crown,” *Dent. Today*, vol. 32, no. 1, p. 14, 2013.

[45] R. C. Garvie, “The Occurrence of Metastable Tetragonal Zirconia as a Crystallite Size Effect,” *J. Phys. Chem.*, vol. 69, no. 4, pp. 1238–1243, Apr. 1965.

[46] A. Suresh, M. J. Mayo, W. D. Porter, and C. J. Rawn, “Crystallite and Grain-Size-Dependent Phase Transformations in Yttria-Doped Zirconia,” *J. Am. Ceram. Soc.*, vol. 86, no. 2, pp. 360–362, Feb. 2003.

[47] F. F. Lange, “Transformation toughening,” *J. Mater. Sci.*, vol. 17, no. 1, pp. 225–234, Jan. 1982.

[48] F. Zhang, K. Vanmeensel, M. Inokoshi, M. Batuk, B. Hadermann, B. Van Meerbeek, I. Naert, and J. Vleugels, “Critical influence of alumina content on the low temperature degradation of 2–3 mol% yttria-stabilized TZP for dental restorations,” *J. Eur. Ceram. Soc.*, vol. 35, no. 2, pp. 741–750, 2014.

[49] a. Eichler, “Tetragonal Y-doped zirconia: Structure and ion conductivity,” *Phys. Rev. B*, vol. 64, no. 17, pp. 1–8, 2001.

[50] J. Livage, K. Doi, and C. Mazieres, “Nature and Thermal Evolution of Amorphous Hydrated Zirconium Oxide,” *J. Am. Ceram. Soc.*, vol. 51, no. 6, pp. 349–353, Jun. 1968.

[51] E. C. Subbarao, “Zirconia - an overview,” in *Advances in Ceramics*, vol. 3, A. H. Heuer and L. Hobbs, Eds. Columbus, OH, USA: The American Ceramic Society, 1981, pp. 1–24.

[52] M. I. Osendi, J. S. Moya, C. J. Serna, and J. Soria, “Metastability of Tetragonal Zirconia Powders,” *J. Am. Ceram. Soc.*, vol. 68, no. 3, pp. 135–139, Mar. 1985.

[53] N. Narita, I. Leng, and S. Inada, “Environmental Effect on Phase Stability in Y-TZP Ceramics,” in *Sintering 87: Proceedings of the Fourth International Symposium on Science and Technology of Sintering*, S. Somiya, M. Shimada, M. Yoshimura, and R. Watanabe, Eds. Tokyo, Japan: Elsevier, London, 1988, pp. 1130– 1135.

[54] S. P. S. Badwal and N. Nardella, “Formation of monoclinic zirconia at the anodic face of tetragonal zirconia polycrystalline solid electrolytes,” *Appl. Phys. A Solids Surfaces*, vol. 49, no. 1, pp. 13–24, Jul. 1989.

[55] M. Hillert, “Thermodynamic Model of the Cubic - Tetragonal Transition in Nonstoichiometric Zirconia,” *J. Am. Ceram. Soc.*, vol. 74, no. 8, pp. 2005–06, 1991.

[56] J. Katamura and T. Sakuma, “Thermodynamic Analysis of the Cubic-Tetragonal Phase Equilibria in the System ZrO2-YO1.5,” *J. Am. Ceram. Soc.*, vol. 80, no. 10, pp. 2685–2688, Jan. 2005.

[57] P. Kontouros and G. Petzow, “Defect Chemistry, Phase Stability and Properties of zirconia Polycrystals,” in *Science and Technology of Zirconia V*, S. P. S. Badwall, B. M. J, and R. H. J. Hannink, Eds. Technomic Publishing Co. Inc., 1992, pp. 30–48.

[58] S. Ostanin, E. Salamatov, A. J. Craven, D. W. McComb, and D. Vlachos, “Theory of the phases and atomistic structure of yttria-doped zirconia,” *Phys. Rev. B*, vol. 66, no. 13, p. 132105, Oct. 2002.

[59] P. Li, I.-W. Chen, and J. E. Penner-hahn, “Effect of Dopants on Zirconia Stabilization-An X-ray Absorption Study: III, Charge-Compensating Dopants,” *J. Am. Ceram. Soc.*, vol. 77, no. 194, pp. 1289–95, 1994.

[60] P. Li and I. W. Chen, “Effect of dopants on zirconia stabilization - an X-ray-absorption study .2. Tetravalent dopants,” *Journal of the American Ceramic Society*, vol. 77, no. 5. pp. 1281–1288, 1994.

[61] J. Chevalier, B. Cales, and J. M. Drouin, “Low-Temperature Aging of Y-TZP Ceramics,” *J. Am. Ceram. Soc.*, vol. 82, no. 8, pp. 2150–2154, Dec. 1999.

[62] V. Lughi and D. R. Clarke, “High temperature aging of YSZ coatings and subsequent transformation at low temperature,” *Surf. Coatings Technol.*, vol. 200, no. 5–6, pp. 1287–1291, Nov. 2005.

[63] J. Chevalier, L. Gremillard, and S. Deville, “Low-Temperature Degradation of Zirconia and Implications for Biomedical Implants,” *Annu. Rev. Mater. Res.*, vol. 37, no. 1, pp. 1–32, Aug. 2007.

[64] M. Keuper, K. Eder, C. Berthold, and K. G. Nickel, “Direct evidence for continuous linear kinetics in the low-temperature degradation of Y-TZP,” *Acta Biomater.*, vol. 9, no. 1, pp. 4826–4835, Jan. 2013.

[65] K. Tsukama and M. Shimada, “Thermal stability of Y2O3 -partially stabilized zirconia (Y-PSZ) and Y-PSZ/ Al2O3 composites,” *J. Mater. Sci. Lett.*, vol. 4, pp. 857–861, 1985.

[66] F. F. Lange, “Transformation-toughened ZrO2 - correlations between grain-size control and composition in the system ZrO2-Y2O3,” *J. Am. Ceram. Soc.*, vol. 69, no. 3, pp. 240–242, 1986.

[67] T. Sato, S. Ohtaki, and M. Shimada, “Transformation of yttria partially stabilized zirconia by low temperature annealing in air,” *J. Mater. Sci.*, vol. 20, no. 4, pp. 1466–1470, Apr. 1985.

[68] T. Sato and M. Shimada, “Transformation of Yttria-Doped Tetragonal ZrO2 Poly crystals by Annealing in Water,” *J. Am. Ceram. Soc.*, vol. 68, no. 6, pp. 356–359, Dec. 1985.

[69] L. Ruiz and M. J. Readey, “Effect of Heat Treatment on Grain Size, Phase Assemblage, and Mechanical Properties of 3 mol% Y-TZP,” *J. Am. Ceram. Soc.*, vol. 79, no. 9, pp. 2331–2340, Sep. 1996.

[70] T. Kosmač and A. Kocjan, “Ageing of dental zirconia ceramics,” *J. Eur. Ceram. Soc.*, vol. 32, no. 11, pp. 2613–2622, 2012.

[71] K. Matsui, H. Horikoshi, N. Ohmichi, M. Ohgai, H. Yoshida, and Y. Ikuhara, “Cubic-Formation and Grain-Growth Mechanisms in Tetragonal Zirconia Polycrystal,” *J. Am. Ceram. Soc.*, vol. 86, no. 8, pp. 1401–1408, Aug. 2003.

[72] K. Matsui, N. Ohmichi, M. Ohgai, H. Yoshida, and Y. Ikuhara, “Effect of alumina-doping on grain boundary segregation-induced phase transformation in yttria-stabilized tetragonal zirconia polycrystal,” *J. Mater. Res.*, vol. 21, no. 09, pp. 2278–2289, Sep. 2006.

[73] J. Chevalier, “Critical effect of cubic phase on aging in 3mol% yttria-stabilized zirconia ceramics for hip replacement prosthesis,” *Biomaterials*, vol. 25, no. 24, pp. 5539–5545, Nov. 2004.

[74] S. Schmauder and H. Schubert, “Significance of Internal Stresses for the Martensitic Transformation in Yttria-Stabilized Tetragonal Zirconia Polycrystals During Degradation,” *J. Am. Ceram. Soc.*, vol. 69, no. 7, pp. 534–540, Jul. 1986.

[75] S. Deville and J. Chevalier, “Martensitic Relief Observation by Atomic Force Microscopy in Yttria-Stabilized Zirconia,” *J. Am. Ceram. Soc.*, vol. 86, no. 12, pp. 2225–27, 2003.

[76] J. Chevalier, “What future for zirconia as a biomaterial?,” *Biomaterials*, vol. 27, no. 4, pp. 535–543, Feb. 2006.

[77] T. Sato and M. Shimada, “Transformation of Yttria-Doped Tetragonal ZrO2 Polycrystals by Annealing in Water,” *J. Am. Ceram. Soc.*, vol. 68, no. 6, pp. 356–356, Jun. 1985.

[78] T. Kosmač, Č. Oblak, P. Jevnikar, N. Funduk, and L. Marion, “Strength and reliability of surface treated Y-TZP dental ceramics,” *J. Biomed. Mater. Res.*, vol. 53, no. 4, pp. 304–313, 2000.

[79] F. F. Lange, G. L. Dunlop, and B. I. Davis, “Degradation During Aging of Transformation-Toughened ZrO2-Y2O3 Materials at 250oC,” *J. Am. Ceram. Soc.*, vol. 69, no. 3, pp. 237–240, Mar. 1986.

[80] D. Kim, “Phase transformations of Y2O3 and Nb2O5 doped tetragonal zirconia during low temperature aging in air,” *Solid State Ionics*, vol. 80, no. 1–2, pp. 67–73, Aug. 1995.

[81] T. Sato and M. Shimada, “Transformation of ceria-doped tetragonal zirconia polycrystals by annealing in water.,” *Am Ceram Soc Bull*, vol. 64, pp. 1382–1384, 1985.

[82] M. Yoshimura, T. Noma, K. Kawabata, and S. Sōmiya, “Role of H2O on the degradation process of Y-TZP,” *J. Mater. Sci. Lett.*, vol. 6, no. 4, pp. 465–467, Apr. 1987.

[83] H. Schubert and F. Frey, “Stability of Y-TZP during hydrothermal treatment: neutron experiments and stability considerations,” *J. Eur. Ceram. Soc.*, vol. 25, no. 9, pp. 1597–1602, Jun. 2005.

[84] X. Guo and T. Schober, “Water Incorporation in Tetragonal Zirconia,” *J. Am. Ceram. Soc.*, vol. 87, no. 4, pp. 746–748, Apr. 2004.

[85] M. Weller and H. Schubert, “Internal friction, dielectric loss, and ionic conductivity of tetragonal ZrO2–3% Y2O3 (Y-TZP),” *J. Am. Ceram. Soc.*, vol. 69, pp. 573–577, 1986.

[86] S. P. S. Badwal, “Ceramic superionic conductors,” in *Structure and Properties of Ceramics , vol.11*, M. Swain, Ed. VCH, Weinheim, 1994, pp. 567–633.

[87] M. Kilo, C. Argirusis, G. Borchardt, and R. A. Jackson, “Oxygen diffusion in yttria stabilised zirconia-experimental results and molecular dynamics calculations,” *Phys. Chem. Chem. Phys.*, vol. 5, no. 11, p. 2219, 2003.

[88] A. E. Hughes, F. T. Ciacchi, and S. P. S. Badwal, “Role of O2-, OH- and anion vacancies in the degradation of Y-TZP in moist environments,” *J. Mater. Chem.*, vol. 4, no. 2, p. 257, 1994.

[89] K.-D. Kreuer, “Proton Conductivity: Materials and Applications,” *Chem. Mater.*, vol. 8, no. 3, pp. 610–641, Jan. 1996.

[90] S. Fabris, “A stabilization mechanism of zirconia based on oxygen vacancies only,” *Acta Mater.*, vol. 50, no. 20, pp. 5171–5178, Dec. 2002.

[91] X. Guo, “On the degradation of zirconia ceramics during low-temperature annealing in water or water vapor,” *J. Phys. Chem. Solids*, vol. 60, no. 4, pp. 539–546, Apr. 1999.

[92] X. Guo, “In Situ Monitoring of the Low Temperature Degradation of Tetragonal Zirconia with Impedance Spectroscopy,” *Adv. Eng. Mater.*, vol. 2, no. 9, pp. 604–607, Sep. 2000.

[93] X. Guo, “Title: Hydrothermal degradation mechanism of tetragonal Zirconia,” *J. Mater. Sci.*, vol. 36, no. 15, pp. 3737–3744, 2001.

[94] H. K. Schmid, “Diffusion-Induced Grain-Boundary Migration in Ceria-Stabilized Tetragonal Zirconia Polycrystals,” *J. Am. Ceram. Soc.*, vol. 74, no. 2, pp. 387–394, Feb. 1991.

[95] J.-K. Lee, Y. J. Kim, and H. Kim, “Formation of irregular grain shapes by ceria doping in 3 mol% yttria-stabilized zirconia ceramics,” *Mater. Lett.*, vol. 33, no. 5–6, pp. 279–282, Jan. 1998.

[96] M. M. R. Boutz, A. J. A. Winnubst, B. Van Langerak, R. J. M. Olde Scholtenhuis, K. Kreuwel, and A. J. Burggraaf, “The effect of ceria co-doping on chemical stability and fracture toughness of Y-TZP,” *J. Mater. Sci.*, vol. 30, no. 7, pp. 1854–1862, Jan. 1995.

[97] J. G. Duh and M. Y. Lee, “Fabrication and sinterability in Y2O3-CeO2-ZrO2,” *J. Mater. Sci.*, vol. 24, no. 12, pp. 4467–4474, Dec. 1989.

[98] E. Camposilvan, F. G. Marro, A. Mestra, and M. Anglada, “Enhanced reliability of yttria-stabilized zirconia for dental applications,” *Acta Biomater.*, vol. 17, pp. 36–46, Apr. 2015.

[99] H. Tsubakino, R. Nozato, and M. Hamamoto, “Effect of Alumina Addition on the Tetragonal-to-Monoclinic Phase Transformation in Zirconia-3 mol% Yttria,” *J. Am. Ceram. Soc.*, vol. 74, no. 2, pp. 440–443, Feb. 1991.

[100] I. M. Ross, W. M. Rainforth, D. W. McComb, A. J. Scott, and R. Brydson, “The role of trace additions of alumina to yttria-tetragonal zirconia polycrystals (Y-TZP),” *Scr. Mater.*, vol. 45, no. 6, pp. 653–660, 2001.

[101] Z. Wu, N. Li, C. Jian, W. Zhao, and J. Yan, “Low temperature degradation of Al2O3-doped 3Y-TZP sintered at various temperatures,” *Ceram. Int.*, vol. 39, no. 6, pp. 7199–7204, Aug. 2013.

[102] P. Vomacka, R. Ramesh, and S. Hampshire, “Influence of Zirconia Addition on the Crystallization Kinetics of a Y-Si-Al-O-N Glass,” *J. Eur. Ceram. Soc.*, vol. 16, no. 11, pp. 1253–1262, 1996.

[103] D. Tang, K.-J. Lee, J. Xu, H.-B. Lim, K. Park, and W.-S. Cho, “Effect of the Al2O3 content on the mechanical properties and microstructure of 3Y-TZP ceramics for dental applications,” *Met. Mater. Int.*, vol. 18, no. 3, pp. 545–551, Jun. 2012.

[104] S. M. Lakiza and L. M. Lopato, “Stable and Metastable Phase Relations in the System Alumina-Zirconia-Yttria,” *J. Am. Ceram. Soc.*, vol. 80, no. 4, pp. 893–902, Jan. 2005.

[105] A. A. Nogiwa-Valdez, W. M. Rainforth, P. Zeng, and I. M. Ross, “Deceleration of hydrothermal degradation of 3Y-TZP by alumina and lanthana co-doping,” *Acta Biomater.*, vol. 9, no. 4, pp. 6226–6235, Apr. 2013.

[106] L. Gremillard, J. Chevalier, T. Epicier, and G. Fantozzi, “Improving the Durability of a Biomedical-Grade Zirconia Ceramic by the Addition of Silica,” *J. Am. Ceram. Soc.*, vol. 85, no. 2, pp. 401–7, 2002.

[107] L. Gremillard, T. Epicier, J. Chevalier, and G. Fantozzi, “Microstructural study of silica-doped zirconia ceramics,” *Acta Mater.*, vol. 48, no. 18–19, pp. 4647–4652, 2000.

[108] F. Filser, P. Kocher, F. Weibel, H. Lüthy, P. Schärer, and L. J. Gauckler, “Reliability and strength of all-ceramic dental restorations fabricated by direct ceramic machining (DCM).,” *Int. J. Comput. Dent.*, vol. 4, no. 2, pp. 89–106, 2001.

[109] D. K. Shetty, A. R. Rosenfield, M. P., B. K. Bansal, and W. H. Duckworth, “Biaxial Flexure Tests for Ceramics,” *Ceram. Bull.*, vol. 59, no. 12, pp. 1193–1197, 1980.

[110] K. Niihara, R. Morena, and D. Hasselman, “Evaluation of KIc of brittle solids by the indentation method with low crack-to-indent ratios,” *J Mater Sci Lett*, vol. 1, pp. 13–16, 1982.

[111] R. S. Krishnan, “Raman spectrum of alumina and the luminescence of ruby,” *Proc. Indian Acad. Sci. - Sect. A*, vol. 26, no. 6, pp. 450–459, 1947.

[112] A. Aminzadeh, “Excitation Frequency Dependence and Fluorescence in the Raman Spectra of Al2O3,” *Appl. Spectrosc.*, vol. 51, no. 6, pp. 817–819, Jun. 1997.

[113] X. Guo and J. Maier, “Grain Boundary Blocking Effect in Zirconia: A Schottky Barrier Analysis,” *J. Electrochem. Soc.*, vol. 148, no. 3, p. E121, 2001.

[114] T. Stoto, M. Nauer, and C. Carry, “Influence of Residual Impurities on Phase Partitiioning and Grain Growth Processes of Y-TZP Materials,” *J. Am. Ceram. Soc.*, vol. 74, no. 10, pp. 2615–2621, Oct. 1991.

[115] C.-C. Chen, H. I. Hsiang, and C. M. Zhou, “Effects of the addition of minute amounts of alumina on the microstructure and sintering behavior of yttria stabilized tetragonal zirconia polycrystals ceramic via a co-precipitation process,” *J. Ceram. Process. Res.*, vol. 9, no. 3, pp. 1–6, 2008.

[116] G. A. Rankin and H. E. Merwin, “The Ternary System CaO-Al2O3 -MgO.,” *J. Am. Chem. Soc.*, vol. 38, no. 3, pp. 568–588, Mar. 1916.

[117] M. Ruhle, N. Claussen, and A. Heuer, “No Title,” in *Science and Technology of Zirconia II*, Advances i., M. Ruhle, N. Claussen, and A. Heuer, Eds. Columbus, 1984, pp. 352–370.

[118] D. Casellas, A. Feder, L. Llanes, and M. Anglada, “Fracture toughness and mechanical strength of Y-TZP/PSZ ceramics,” *Scr. Mater.*, vol. 45, no. 2, pp. 213–220, Jul. 2001.

[119] M. Yashima, M. Kakihana, and M. Yoshimura, “Metastable-stable phase diagrams in the zirconia-containing systems utilized in solid-oxide fuel cell application,” *Solid State Ionics*, vol. 86–88, pp. 1131–1149, Jul. 1996.

[120] O. Fabrichnaya and F. Aldinger, “Assessment of thermodynamic parameters in the system ZrO2 –Y2O3 –Al2O3,” *Zeitschrift für Met.*, vol. 95, no. 1, pp. 27–39, Jan. 2004.

[121] X. Guo and Z. Zhang, “Grain size dependent grain boundary defect structure: case of doped zirconia,” *Acta Mater.*, vol. 51, no. 9, pp. 2539–2547, May 2003.

[122] M. Martin, “Grain boundary ionic conductivity of yttrium stabilized zirconia as a function of silica content and grain size,” *Solid State Ionics*, vol. 161, no. 1–2, pp. 67–79, Jul. 2003.

[123] F. G. Marro, R. Chintapalli, P. Hvizdos, F. Soldera, F. Mücklich, and M. Anglada, “Study of near surface changes in yttria-doped tetragonal zirconia after low temperature degradation,” *Int. J. Mater. Res.*, vol. 100, no. 1, pp. 92–96, Jan. 2009.

[124] J. a. Muñoz-Tabares, E. Jiménez-Piqué, and M. Anglada, “Subsurface evaluation of hydrothermal degradation of zirconia,” *Acta Mater.*, vol. 59, no. 2, pp. 473–484, 2011.

[125] E. Jiménez-Piqué, A. Ramos, J. A. Muñoz-Tabares, A. Hatton, F. Soldera, F. Mücklich, and M. Anglada, “Focused ion beam tomography of zirconia degraded under hydrothermal conditions,” *J. Eur. Ceram. Soc.*, vol. 32, no. 10, pp. 2129–2136, Aug. 2012.

[126] G. V. Franks and Y. Gan, “Charging Behavior at the Alumina–Water Interface and Implications for Ceramic Processing,” *J. Am. Ceram. Soc.*, vol. 90, no. 11, pp. 3373–3388, Nov. 2007.

[127] S. Ramesh, S. Meenaloshini, C. Y. Tan, W. J. K. Chew, and W. D. Teng, “Effect of manganese oxide on the sintered properties and low temperature degradation of Y-TZP ceramics,” *Ceram. Int.*, vol. 34, no. 7, pp. 1603–1608, Sep. 2008.

[128] X. Guo, “Roles of Alumina in Zirconia for Functional Applications,” *J. Am. Ceram. Soc.*, vol. 86, no. 11, pp. 1867–1873, Nov. 2003.

[129] N. A. Toropov and I. A. Bondar, “Silicates of the rare earth elements,” *Bull. Acad. Sci. USSR Div. Chem. Sci.*, vol. 10, no. 4, pp. 502–508, Apr. 1961.

[130] Z. Shen, Y. Xiong, T. Höche, D. Salamon, Z. Fu, and L. Belova, “Ordered coalescence of nanocrystals: a path to strong macroporous nanoceramics,” *Nanotechnology*, vol. 21, no. 20, p. 205602, May 2010.

[131] D. Salamon, K. Maca, and Z. Shen, “Rapid sintering of crack-free zirconia ceramics by pressure-less spark plasma sintering,” *Scr. Mater.*, vol. 66, no. 11, pp. 899–902, Jun. 2012.

[132] J. Hu and Z. Shen, “Ordered coalescence of nanocrystallites contributing to the rapid anisotropic grain growth in silicon nitride ceramics,” *Scr. Mater.*, vol. 69, no. 3, pp. 270–273, Aug. 2013.

[133] X. Guo, “Space-charge conduction in yttria and alumina codoped-zirconia,” *Solid State Ionics*, vol. 96, no. 3–4, pp. 247–254, Apr. 1997.

[134] N. Mitra, K. Vijayan, B. N. P. Bai, and S. K. Biswas, “Phase Transformation Introduced by Mechanical and Chemical Surface Preparations of Tetragonal Zirconia Polycrystals,” *J. Am. Ceram. Soc.*, vol. 76, no. 2, pp. 533–535, Feb. 1993.

[135] I. L. Denry and J. A. Holloway, “Microstructural and crystallographic surface changes after grinding zirconia-based dental ceramics.,” *J. Biomed. Mater. Res. B. Appl. Biomater.*, vol. 76, no. 2, pp. 440–8, 2006.

[136] J. Kondoh, “Origin of the hump on the left shoulder of the X-ray diffraction peaks observed in Y2O3-fully and partially stabilized ZrO 2,” *J. Alloys Compd.*, vol. 375, no. 1–2, pp. 270–282, 2004.

[137] D. P. Burke and W. M. Rainforth, “Intermediate rhombohedral (r-ZrO2) phase formation at the surface of sintered Y-TZP’s,” *J. Mater. Sci. Lett.*, vol. 16, no. 11, pp. 883–885, 1997.

[138] T. Sakuma, Y.-I. Yoshizawa, and H. Suto, “The rhombohedral phase produced in partially-stabilized zirconia,” *J. Mater. Sci. Lett.*, vol. 4, no. 1, pp. 29–30, Jan. 1985.

9 Index of Figures

Figure 1: Schematic representation of the three polymorphs of ZrO_2 and the corresponding space groups: (a) cubic (*Fm*3*m*), (b) tetragonal ($P4_2/nmc$), and (c) monoclinic ($P2_1/c$). (Source: H. J. Hannink et al. [7]). 2

Figure 2: Evolution of the zirconia–yttria phase diagram: (a) original diagram by Duwez [13] in 1951; (b) diagram presented by Scott in 1975 [14]; (c) and (d) the most recent diagrams [15]; (d) is the metastable phase diagram (Source: Chevalier et al. [28]). Unsigned regions in Duwez's phase diagram were assumed to be two-phase without actual experimental proof. The hatched region in Scott's phase diagram shows the uncertainty of characteristic features of the martensitic transformation, such as the initial and final temperatures. 4

Figure 3: Estimated time of diffusion needed to homogenize the Y content of 0.5- and 3-μm-diameter grains at different temperatures in 3Y-TZP. TZP – tetragonal zirconia polycrystals; Y – yttria. 5

Figure 4: Shemathic representation of the crystal structures of monoclinic, *t'*, *t''* and cubic phases (Source: Yashima et al. [29]). 5

Figure 5: SEM micrograph of 3Y-TZP (TZ-PX-242A, Tosoh, Japan) sintered at 1550 °C for 2 h. 6

Figure 6: Monoclinic content measured by XRD versus time for 3Y-TZP sintered at 1500 °C for 2 h, polished and aged at temperatures ranging from 70 to 130 °C (Source: Chevalier et al. [61]). 10

Figure 7: Nucleation-and-growth process observed by optical interferometry (the circled area indicates a monoclinic spot). (Source: Chevalier et al. [63]). 11

Figure 8: Transformed layer thickness determined in FIB cuts of 3Y-TZP versus ageing time at 134°C. (Source: Keuper et al. [64]). 11

Figure 9: Sintering-temperature-dependent average grain sizes of TZ-3YB-E and TZ-3YSB-E ceramics evaluated by using the linear interception method (Source: Kosmač et al. [70]). 12

Figure 10: Calculated fraction of monoclinic zirconia (Xm) versus accelerated in vitro ageing time for the TZ-3YSB-E and TZ-3YB-E ceramic surfaces, sintered for 2 h in the temperature range 1400–1550 °C (Source: Kosmač et al. [70]). 12

Figure 11: SEM micrographs of sintered at 1550 °C for 2 h 3Y-TZP powders produced by (a) Zirconia Sales of America, Atlanta (source: Ruiz et al. [69]) and (b) Tosoh, Japan. (Source: Chevalier et al. [73]) 13

Figure 12: Progressive transformation of a grain in 3Y-TZP. The first variants (arrow) appeared at a grain boundary triple junction (Source: Deville et al. [75]). 13

Figure 13: Scheme of the ageing process occurring in a cross section, showing the transformation neighbor to neighbor. (a) Nucleation on a particular grain at the surface, leading to microcracking and stresses to the neighbors. (b) Growth of the transformed zone, leading to extensive microcracking and surface roughening. Transformed grains are gray. Red path represents the penetration of water due to microcracking around the transformed grains. (Source: Chevalier et al. [76])....14

Figure 14: Proposed degradation process of Y-TZP by H_2O: 1) the adsorption of water to form Zr-OH 2) reaction of water with Zr-0-Zr bonds to form two Zr-OH groups 3) the migration of OH^- species in the lattice 4) the accumulation of stresses and as a result the nucleation of LTD. (Source: Yoshimura et al. [82]) 15

Figure 15: SEM micrograph of 3Y-TZP containing 0.25 wt% alumina (Source: Wu et al. [101])....17

Figure 16: TEM micrographs of (a) silica-free and (b) silica-containing 3Y-TZP material, showing faceted grains for pure material and round grains with smal amorphous pockets (see arrows) for 3Y-TZP/SiO_2 material (Source: Gremillard et al. [106]). 18

Figure 17: Williamson–Hall plot of (Z-S0) pure and (Z-S05) silica-doped 3Y-TZP, showing that Z-S0 material exhibits more internal stresses than Z-S05 material (Source: Gremillard et al. [106]). 19

Figure 18: Piston-on-3-ball experimental configuration. 25

Figure 19: Pore size distribution measured by mercury intrusion porosimetry for TZ and 0.05A-TZ materials pre-sintered at 900 °C and 0.25A-TZ material pre-sintered at 1000 °C....29

Figure 20: TGA/DTA analysis of soaked in dynasylan and dried 0.25A-TZ sample.....30

Figure 21: Sintering program used for silica-doped TZ, 0.05A-TZ and 0.25A-TZ materials. 30

Figure 22: XRD patterns collected from the 0.25A-TZ/SiO_2 samples, obtained by the soaking of pre-sintered TZ in pure dynasylan for 5 min; prehydrolysed dynasylan for 30 min and prehydrolysed dynasylan for 60 min followed by final sintering at 1450 °C for 4 h. 31

Figure 23: Raman spectra of 0.25A-TZ/SiO_2 samples, obtained by the soaking of pre-sintered 0.25A-TZ in (a) pure dynasylan for 5 min (b) prehydrolysed dynasylan for 30 min and finally sintered at 1450 °C for 4 h....31

Figure 24: Scanning electron micrographs of 0.25A-TZ specimens infiltrated using (a) pure and (b) prehydrolyzed dynasylan and sintered at 1450 °C for 4 h. 32

Figure 25: FIB-SEM cross-section of the 24-hours aged 0.25A-TZ/SiO_2 specimen. 32

Figure 26: SEM micrographs of polished and thermally etched surfaces of pure TZ, 0.05A-TZ and 0.25A-TZ discs sintered at 1400-1600 °C for 2 h. Dashed circles show alumina grains. 34

Figure 27: SEM micrographs of polished and thermally etched surfaces of silica-doped TZ, 0.05A-TZ and 0.25A-TZ discs sintered at 1400-1600 °C for 2 h. 35

Figure 28: TEM micrographs of (a) 0.05A-TZ and (b-d) 0.05A-TZ/SiO_2 specimens, sintered at 1450 °C....36

Figure 29: XRD patterns obtained from the 0.25A-TZ/SiO_2 ceramic surfaces, sintered at 1400-1600 °C for 2 h....37

Figure 30: Detailed XRD patterns in (a) 34-35° 2Θ regions and (b) 72-75° 2Θ regions obtained from the pure and silica-doped TZ, 0.05A-TZ and 0.25A-TZ ceramic surfaces, sintered at 1600°C for 2 h. 38
Figure 31: Raman spectra of TZ, 0.25A-TZ and 0.25A-TZ/SiO_2 materials sintered at 1600 °C for 2 h (632.8 nm He-Ne laser). 38
Figure 32: Comparison of Raman and luminescent spectra upon excitation with 514.5 Ar laser and 632.8 nm He-Ne laser. 39
Figure 33: Raman spectra of 0.05A-TZ material sintered at 1600 °C for 2 h (632.8 nm He-Ne laser). 39
Figure 34: Fractured surfaces of as-sintered at 1450 °C (a) TZ, (b) 0.05A-TZ, (c) 0.25A-TZ and (d) TZ/SiO_2 (e) 0.05A-TZ/SiO_2 (f) 0.25A-TZ/SiO_2 materials after a bending test. 41
Figure 35: SEM micrographs of indentations into a sintered at 1450 °C (a) TZ (b) 0.05A-TZ (c) 0.25A-TZ (d) TZ/SiO_2 (e) 0.05A-TZ/SiO_2 and (f) 0.25A-TZ/SiO_2 materials. 41
Figure 36: Fractured surfaces of as-sintered at 1400 °C for 2 h (a) TZ/SiO_2, (b) 0.05A-TZ/SiO_2, (c) 0.25A-TZ/SiO_2 and as-sintered at 1600 °C (d) TZ/SiO_2 (e) 0.05A-TZ/SiO_2 (f) 0.25A-TZ/SiO_2 materials. 42
Figure 37: Impedance spectra obtained at 258 °C for 0.25A-TZ and 0.25A-TZ/SiO_2 materials. 42
Figure 38: Equivalent circuit used for fitting of experimental data. 43
Figure 39: Ratio of grain boundary resistivity to bulk resistivity as a function of temperature. 43
Figure 40: Temperature dependence of the resistivity ratio of 0.25A-TZ/SiO_2 to 0.25A-TZ. Silica addition to 0.25A-TZ material sintered at 1450 °C for 2 h does not influence on the bulk resistivity, while it drastically increases the grain boundary resistivity by about 10 times. 44
Figure 41: Arrhenius plots of grain boundary and bulk resistivity: (a) 0.25A-TZ activation energy for the bulk resistivity $Eabulk$= 0.89 eV, (b) 0.25A-TZ activation energy for the grain boundary resistivity $EaGB = 1.08\ eV$, (c) 0.25A-TZ/SiO_2 $Eabulk$= 0.88 eV, (d) 0.25A-TZ/SiO_2 $EaGB = 1.06\ eV$ 45
Figure 42: Transmittance of 1.5 mm thick 0.05A-TZ and 0.05A-TZ/SiO_2 materials sintered at 1450 °C for 2 h. 46
Figure 43: XRD patterns obtained from (a) 0.25A-TZ/SiO_2 ceramic surfaces, sintered for 2 h at 1600 °C and aged in water at 134 °C for 6, 24, 48, 135, 177 and 230 h; (b) 0.05A-TZ ceramic surfaces, sintered for 2 h at 1450 °C and aged in water at 160 °C for 2, 4, 7, 11, 18 and 23 h. Arrows point the broadening of $(1\ 01)_t/(1\ 1\ 1)_c$ peak. 46
Figure 44: XRD patterns obtained from (a) 0.25A-TZ and TZ/SiO_2 ceramic surfaces, sintered for 2 h at 1450 °C and aged in water at 134 °C for 24 h; (b) 0.25A- TZ/SiO_2 ceramic surfaces, sintered for 2 h at 1600 °C and 1550 °C and aged in water at 134 °C for 24 h and 48 h respectively. 47
Figure 45: Calculated monoclinic fraction versus in vitro ageing time for pure and silica-doped TZ, 0.05A-TZ and 0.25A-TZ materials sintered at 1450 °C for 4 h. 48
Figure 46: Optical micrographs of the cross-sections of pure and silica-doped TZ, 0.05A-TZ and 0.25A-TZ samples sintered at 1450 °C for 4 h and aged for 72-120 h. Time of ageing increases left-to-right along each material in a row. 49

Figure 47: Optical micrographs of the cross-sections of pure and silica-doped TZ, 0.05A-TZ and 0.25A-TZ samples sintered at 1600 °C for 2 h and aged for 24-72 h. Time of ageing increases left-to-right along each material in a row. 50

Figure 48: Thickness of the transformed layer versus *in vitro* ageing time measured from cross-sections of pure and silica-doped TZ, 0.05A-TZ and 0.25A-TZ materials sintered at: (a) 1450°C for 4 h, (b) 1600 °C for 2 h. 51

Figure 49: FIB-SEM cross-sections of the 24-hours aged (a) TZ, (b) 0.25A-TZ, (c) TZ/SiO_2 and (d) 0.25A-TZ/SiO_2 specimens. White line indicates a rough estimate of the *t-m* transformed layer border (In Fig. 49a the layer was extending into the bulk beyond the lower end of the cross-section). 52

Figure 50: A higher-magnification FIB-SEM cross-sections of the 24-hours aged (a) TZ, (b) 0.25A-TZ, (c) TZ/SiO_2 and (d) 0.25A-TZ/SiO_2 specimens. White arrows point to grain boundary microcracks, while black arrows indicate the martensitic monoclinic variants. 52

Figure 51: Calculated monoclinic fraction for pure and silica-doped TZ and 0.25A-TZ materials sintered at 1400-1600 °C for 2 h and *in vitro* aged for 24 h. 54

Figure 52: Calculated monoclinic fraction versus *in vitro* ageing at 134 °C for 0.25A-TZ/SiO_2 materials sintered at 1500-1600 °C for 2 h. 54

Figure 53: XRD patterns obtained from the surfaces of (a) pure and silica-doped TZ and 0.25A-TZ materials sintered at 1600 °C and aged until the saturation, (b) 0.25A-TZ/SiO_2 materials sintered at 1450-1600 °C and aged until the saturation. 54

Figure 54: Optical micrographs of a Vickers indentations into a (a) 0.25A-TZ (b) TZ/SiO_2 (c) 0.25A-TZ/SiO_2 materials sintered at 1450 °C for 4 h (d) 0.25A-TZ (e) TZ/SiO_2 (f) 0.25A-TZ/SiO_2 materials sintered at 1450 °C for 4 h aged for 24 h (g) 0.25A-TZ and (h) TZ/SiO_2 (i) 0.25A-TZ/SiO_2 materials sintered at 1450 °C for 4 h aged for 48 h. White arrows point the cracks. 56

Figure 55: Raman spectra of 0.25A-TZ material sintered at 1200-1600°C for 2 h. 58

Figure 56: Calculated monoclinic fraction versus in vitro ageing time for pure and silica-doped, 0.05A-TZ materials sintered at 1450 °C for 4 h and 1550 °C for 2 h. 62

Figure 57: XRD patterns obtained from the surfaces of 0.05A-TZ materials sintered at 1450 °C for 4 h and 1550 °C for 2 h and aged for (a) 48 h and (b) 72 h. 62

Figure 58: SEM micrograph of 0.25A-TZ material (top region) sintered at 1600 °C and aged for 72 h. White arrows point to grain boundary microcracks. 63

Figure 59: Y_2O_3-SiO_2 phase diagram. (Source: Toropov et al. [129]). 64

Figure 60: SEM micrographs of polished specimens after the diffusion coupled experiment performed at different annealing/sintering conditions. (a) TZ/SiO_2 and (b) 0.25A-TZ/SiO_2 annealed/sintered at 1450 °C for 4 hours (c) TZ/SiO_2 and (d) 0.25A-TZ/SiO_2 annealed/sintered at 1450 °C for 50 hours; (e) TZ/SiO_2 and (f) 0.25A-TZ/SiO_2 annealed/sintered at 1500 °C for 8 hours. 65

Figure 61: SEM micrographs of sintered at 1600 °C for 2 h and aged until the saturation (a) TZ, (b) 0.25A-TZ, (c) TZ/SiO_2 and (c) 0.25A-TZ/SiO_2 materials. White arrows point to untransformed parts of the grains. 68

Figure 62: TEM micrograph of the 0.25A-TZ/SiO_2 sintered at 1600 °C for 2 h. (a) The micrograph reveals the initiation of grain coalescence, i.e., the region where smaller *t*-ZrO_2 grain merged with a larger *t'*-ZrO_2 grain. The numbered circles represent the location where the SAED were performed and are shown in Figure b–d. (b) the merged region, (c) the silica-containing grain boundary located beneath the merged region, (d) the smaller *t*-ZrO_2 grain. 69

Figure 63: (a) SEM micrograph and (b) FIB-SEM sub-surface microstructure of 0.25A-TZ/SiO_2 sintered at 1600^{o}C for 2 h. 70

Figure 64: 0.25A-TZ/SiO_2 material sintered at 1600 °C and aged for 3 h. White arrows point to martensitic relief. 70

Figure 65: XRD patterns obtained from the surfaces of as-sintered at 1450 °C and aged for 24 h TZ materials. 72

10 Index of Tables

Table 1: Potential effect of the different process stages on the microstructure of zirconia ceramics. (Source: Chevalier et al. [76]) 16

Table 2: Chemical composition of the 3Y-TZP powders as obtained from the commercial suppliers, expressed as wt. %, specific surface area (m^2/g). 22

Table 3: The temperature of shrinkage onset for TZ, 0.05A-TZ and 0.25A-TZ powders evaluated from the dilatometric curves. 23

Table 4: Results of a mercury porosimetry measurements. 29

Table 5: Flexural strength of 0.25A-TZ material infiltrated with pure dynasylan, hydrolised dynasylan for 30 and 60 min and finally sintered at 1450 °C for 4 h. 31

Table 6: Relative densities in percentages of sintered at 1400-1600 °C for 2 h pure and silica-doped TZ, 0.05A-TZ and 0.25A-TZ discs (mean ± SD). 33

Table 7: Average grain sizes in microns of pure and silica-doped TZ, 0.05A-TZ and 0.25A-TZ materials sintered at 1400-1600 °C for 2 h (mean ± SD). 36

Table 8: Indentation toughnes of the pure and silica-doped TZ, 0.05A-TZ and 0.25A-TZ materials (mean ± SD). 40

Table 9: Hardness of the pure and silica-doped TZ, 0.05A-TZ and 0.25A-TZ materials (mean ± SD). 40

Table 10: Flexural strength of the pure and silica-doped TZ, 0.05A-TZ and 0.25A-TZ materials (mean ± SD). 40

Table 11: Bulk and grain boundary resistivity ($\Omega \cdot cm^{-1}$) obtained at 119-443 °C for 0.25A-TZ and 0.25A-TZ/SiO_2 materials sintered at 1450 °C for 4 and 2 h respectively. 44

Table 12: Slope coefficients for ageing curves, obtained by observations of the thickness of the transformed layer on the cross-sections of aged materials using optical interferometry. 51

Table 13: The values of untransformable phase, unnormalised and normalised monoclinic phase after 24 h of ageing at 134°C for pure and silica-doped TZ and 0.25A-TZ/SiO_2 materials sintered at 1600 °C for 2 h. 53

Table 14**:** Flexural strength of the pure and silica-doped TZ, 0.05A-TZ and 0.25A-TZ materials (mean ± SD) after 24 h of ageing. 55

11 Appendix

11.1 Personal Bibliography

1. A. Samodurova, A. Kocjan, M.V. Swain, T. Kosmač. The combined effect of alumina and silica co-doping on the ageing resistance of 3Y-TZP bioceramics. *Acta Biomater.* 11:477-87 (2015).

2. A. Samodurova, D. Vengust, A. Kocjan, T. Kosmač. The sintering-temperature-related microstructure and phase assemblage of alumina-doped and alumina–silica-co-doped 3-mol%-yttria-stabilized tetragonal zirconia. *Scripta Materialia* 105: 50-53 (2015).

3. A. Samodurova, A. Kocjan, T. Kosmač. The effect of silica infiltration on the low temperature degradation and mechanical properties of 3Y-TPZ ceramics. 5. IPSSC, 2013, Ljubljana, Slovenija. Prispevek na konferenci str. 366. COBISS.SI-ID:27436327.